UNIVERSITY OF CALIFORNIA,
IRVINE

Retinal Organoids On-a-Chip: Study of Stem Cell Derived Retinal Organoids Long-term Development and Maintenance

DISSERTATION

submitted in partial satisfaction of the requirements
for the degree of

DOCTOR OF PHILOSOPHY

in Biomedical Engineering

by

Yuntian Xue

Dissertation Committee:
Professor William C. Tang, Chair
Assistant Professor Andrew W. Browne
Associate Professor Magdalene J. Seiler

2022

DEDICATION

To

My family and friends

in recognition of their worth

TABLE OF CONTENTS

LIST OF FIGURES

Page

LIST OF TABLES

Page

ACKNOWLEDGEMENTS

Words cannot express my gratitude to my professor and chair of my committee – Dr. William C. Tang, for his patience and continuous support during my Ph.D. study. I also could not have undertaken this journey without my co-advisors and defense committee members – Dr. Andrew W. Browne and Dr. Magdalene J. Seiler, who generously provided knowledge, expertise and collaborative opportunities, their enthusiasm to research has inspired me all the time. My committee members are not only the best mentors, who taught me how to think and solve a problem, but also the best friends in my life, who shared their life experience and their advice. Special thanks to Dr. Michelle Digman and Dr. Lisa Flanagan, for being my qualifying exam committee members and providing me valuable suggestions.

I am also grateful to all lab members, for their feedback, technical help, and moral support. Many thanks to my undergraduate mentees, for their hard work and contributions to my projects. Thanks should also go to the research assistants, librarians, and technicians from the university, who impacted me and provided professional trainings.

I would be remiss in not mentioning my parents Mr. Wenming Xue and Mrs. Xiaobo Wu, and my boyfriend Mr. Qianwei Xiong. Their belief in me has kept my spirits and motivation high during this process. Their remote company always warmed my heart. Their love and support helped me overcome difficult times. Many thanks to my friends at Irvine, five years of spending time together made us like brothers and sisters.

The text of Chapter Three dissertation is a reprint of the material as it appears in *Lab on a Chip*. The text of Chapter Four dissertation is a reprint of the material as it appears in *Frontiers in Cellular Neuroscience*. The co-authors William C. Tang, Andrew W. Browne and Magdalene J. Seiler listed in these two publications directed and supervised research which forms the basis for the dissertation. Financial support was provided by CIRM (#TRAN1-10995), RPB unrestricted grant to UCI Department of Ophthalmology, ICTS KL2 (#KL2 TR001416), Koehler Foundation and NIH (#R01 EY031834).

VITA

Yuntian Xue

2013-17	B.S. in Materials Science and Engineering,
	Southern University of Science and Technology, Shenzhen, China
2022	Teaching Assistant, Biomedical Engineering,
	University of California, Irvine
2017-22	Ph.D. in Biomedical Engineering,
	University of California, Irvine

FIELD OF STUDY

Stem Cell Technology

Retinal Organoids Developmental Biology

3D printed Microfluidic Device

Two-Photon Functional Imaging

PUBLICATIONS

Xue, Y., Lin, B., Chen, J.T., Tang, W.C., Browne, A.W., Seiler, M.J., 2022 (accepted, in press). The Prospects for Retinal Organoids in Treatment of Retinal Diseases. *Asia-Pacific Journal of Ophthalmology*.

Xue, Y., Seiler, M.J., Tang, W.C., Wang, J.Y., Delgado, J., McLelland, B.T., Nistor, G., Keirstead, H.S. and Browne, A.W., 2021. Retinal Organoids On-a-chip: a Micro-millifluidic Bioreactor for Long-term Organoid Maintenance. *Lab on a Chip*, 21(17), pp.3361-3377.

Xue, Y., Browne, A.W., Tang, W.C., Delgado, J., McLelland, B.T., Nistor, G., Chen, J.T., Chew, K., Lee, N., Keirstead, H.S. and Seiler, M.J., 2021. Retinal Organoids Long-term Functional Characterization Using Two-Photon Fluorescence Lifetime and Hyperspectral Microscopy. *Frontiers in Cellular Neuroscience*, 518.

McAleer, S., Fast, A., Xue, Y., Seiler, M.J., Tang, W.C., Balu, M., Baldi, P. and Browne, A.W., 2021. Deep Learning–Assisted Multiphoton Microscopy to Reduce Light Exposure and Expedite Imaging in Tissues with High and Low Light Sensitivity. *Translational vision science & technology*, 10(12), pp.30-30.

ABSTRACT OF THE DISSERTATION

Retinal Organoids On-a-Chip: Study of Stem Cell Derived Retinal Organoids Long-term Development and Maintenance

by

Yuntian Xue

Doctor of Philosophy in Biomedical Engineering

University of California, Irvine, 2022

Professor William C. Tang, Chair

Retinal degeneration (RD) is a leading cause of vision impairment and blindness worldwide and treatment for advanced RD does not exist. Stem cell-derived retinal organoids (RtOgs) became an emerging tool for tissue replacement therapy. However, existing RtOg production methods are highly heterogeneous. Besides, subjective tissue selection reduces the repeatability of organoid-based scientific experiments and clinical studies. Controlled and predictable methodology and tools are needed to standardize RtOg production, characterization and long-term maintenance.

To optimize and standardize RtOg long-term maintenance, we designed a shear stress-free micro-millifluidic bioreactor platform for nearly labor-free retinal organoid maintenance. We compared different 3D printers for fabricating the mold from which Polydimethylsiloxane (PDMS) was cast to create the bioreactor. We optimized the bioreactor design using *in silico* simulations and *in vitro* evaluation to optimize mass transfer efficiency and concentration uniformity. Once assembled, we successfully cultured RtOgs using different designs of the bioreactors for up to 4 months. We used different quantitative and qualitative techniques to characterize the RtOgs produced with our

bioreactors and compared with those produced with conventional culture to demonstrate the superiority of our approach.

At the same time, to improve the quality control of organoids, we introduced a live imaging technique based on two-photon microscopy (2PM) to non-invasively monitor RtOgs' long-term development. Fluorescence Lifetime Imaging Microscopy (FLIM) was used to monitor the metabolic trajectory, and hyperspectral imaging (HSpec) was applied to characterize structural and molecular changes. These live imaging experimental results were confirmed with endpoint biological tests, including quantitative polymerase chain reaction (qPCR), single-cell RNA sequencing, and immunohistochemistry.

In addition, we applied an advanced electrophysiology testing system to further verify the functionality of matured RtOgs cultured in the bioreactor platform. Spontaneous and light-stimulated spiking activities were observed.

In summary, we designed and optimized a bioreactor for long term RtOg culture in a low shear stress environment that was also compatible with multimodal imaging. We have demonstrated a 2PM-based non-invasive imaging technique to monitor RtOg metabolic and structural changes at the cellular level throughout the entire differentiation and development process. The health of mature RtOgs were further verified with electrophysiological measurements. The methodology and the findings of this study are of great value in live RtOgs long-term maintenance, characterization and monitoring, offering potentially powerful tools in screening and quality control for RtOg production.

Chapter 1 : Introduction

1.1 Outline of the dissertation

The overarching goal of the present research is to standardize retinal organoids (RtOgs) production, characterization and long-term maintenance with the ultimate objective of enhancing the ability for transplantation therapy for retinal degenerative (RD) diseases. The organization of this thesis is outlined below.

Chapter 2 provides a comprehensive review on current status and future prospects of the transplantation therapies with tissues derived from RtOgs for RD disease. In particular, rodent RD disease models, RtOgs culture protocols, analytical tools to evaluate RtOg quality and function, and transplantation approaches and results were reviewed. Methods to form RtOgs from pluripotent stem cells differentiation have been significantly improved and become more efficient in recent years. Transplantation with RtOg-derived tissues has resulted in visual function improvements in several RD models, showing promises for eventual clinical translations. In addition, more novel technologies have been reported to characterize and validate RtOg quality. However, opportunity remains in optimizing tissue differentiation protocols and in achieving better RtOg reproducibility. This review provides the context and background for the research work discussed in subsequent chapters.

Chapter 3 focuses on the engineering approaches to standardize RtOgs long-term maintenance. We designed, fabricated and tested a shear stress-free micro-millifluidic bioreactor platform that aimed at minimizing human labor in maintaining RtOgs for up to 6

months. We first optimized the bioreactor design with *in silico* simulations and *in vitro* evaluation to improve mass transfer efficiency from the infusion channels into the culture chambers and concentration uniformity within the chambers while maintaining near-zero net flow. We successfully cultured RtOgs using different designs of the bioreactors for up to 4 months. Different quantitative and qualitative techniques were used to characterize and compare the RtOgs produced with our bioreactors with those from conventional culture to demonstrate the superiority of our approach.

Chapter 4 describes the optimized RtOgs' long-term characterization method. We introduced a live imaging technique based on two-photon microscopy (2PM) to non-invasively monitor RtOgs' long-term development. Fluorescence Lifetime Imaging Microscopy (FLIM) was used to quantify the metabolic trajectory, and hyperspectral imaging (HSpec) was applied to characterize structural and molecular changes. Time-dependent metabolic and structural developmental trends were observed in this study.

Chapter 5 includes several pilot test results on RtOgs-related research. We examined the effect of immunosuppressant using FLIM, and applied an advanced electrophysiology testing system to further verify the functionality of matured RtOgs cultured in the bioreactor platform. Preliminary data were summarized. Finally, potential future work was suggested to verify and extend the current research results.

A majority of the materials in this dissertation was published in three journal papers. The materials in Chapter 2 were submitted and accepted for publication as a review article in 2022 issue with the *Asia-Pacific Journal of Ophthalmology*. The bulk of Chapter 3 was published in [1], and Chapter 4 in [2].

Chapter 2 : Literature Review – The Prospects for Retinal Organoids in Treatment of Retinal Diseases

2.1 Introduction

Vision is arguably the most critical sense for humans to perceive the surrounding. The retina originates as an outgrowth of the forebrain during embryonic development. The visual pathways start at the retina where light is transduced into neuronal signals that are ultimately conveyed to the visual cortex for visual perception. The retina is a laminated organ that is broadly composed of retinal ganglion cells (RGCs), amacrine cells (ACs), bipolar cells (BCs), horizontal cells (HCs), Müller cells (MCs) and photoreceptors (PRs). Upon absorption of photons by visual photopigments in the PRs, a series of biochemical reactions occurs whereby light signals are transduced into neuronal signals. Whereas surgical treatments for diseases that damage light transmission through the cornea and the lens have been well established, permanent vision losses caused by damage to the RGCs as a result of glaucoma, loss of PRs and RPE from age-related macular degeneration (AMD) and inherited retinal degenerations (IRDs) and damage to all layers of the retina from diabetic retinopathy are irreversible and no therapies to reverse cell death are available.

Recent decades have witnessed the development of stem cell technology for a variety of clinical uses. Under specific culturing conditions, stem cells can be differentiated into self-assembled and layered retinal tissue spheroids that are called retinal organoids (RtOgs). RtOgs have been applied to different applications such as disease modeling [3-7],developmental biology [8-11], drug screening [12], gene therapy testing [4, 13-16], and transplantation therapies [17-23]. In this review, we focus on transplantation studies in

recent years. We briefly review common retinal degeneration diseases, summarize common rodent models with IRD used for RtOg transplantation studies, and explore current methodologies used for RtOg culture and analysis. Lastly, we focus on post-transplantation evaluations and their functional effectiveness. Gene therapy in a dish is outside the scope of this review and is not discussed.

2.2 Retinal Degeneration Diseases and Rodent Disease Models

AMD is marked by the degeneration of the PRs and RPE in the human macula and is the leading cause of irreversible blindness in people over 65 years old in industrialized countries [24]. In the early and intermediate stages, AMD is marked by the accumulation of drusen, a yellowish retinoid breakdown product in the macula beneath the retina. Advanced AMD consists of two main categories – "wet" and "dry" AMD. Wet AMD involves abnormal choroidal blood vessel growth and can be treated by anti-vascular endothelial growth factor (anti-VEGF) [25]. However, there is no proven treatment for dry AMD characterized by RPE and subsequent PR death. The only promising approach may be cellular replacement therapy with transplantation [26].

Retinitis Pigmentosa (RP) is an IRD disease initially affecting peripheral vision progressing to loss of central vision in the end stage. Many gene mutations can yield the RP phenotype, and this heterogeneous genotypic etiology leads to significant difficulties in studying the disease and developing effective treatment [27]. In mutations affecting rod-specific proteins, rod PRs will gradually deteriorate over decades, causing losses of night vision in adolescence, peripheral vision in young adulthood, and central vision in later life

[28]. The functional progression of vision loss is consistent with the characteristic death of rod PRs prior to cone PR death.

Neurons and PRs are highly differentiated cells and lack the ability to repair or regenerate after irreversible damage. Gene therapy has gained popularity in IRD treatment in recent years as summarized in several reviews [29, 30]. For example, a recent study applied subretinal gene therapy that delivered human melanopsin gene (OPN4) and showed vision restoration in retinal degeneration 1 (rd1) mutation mouse model [31]. Several additional studies demonstrated an improvement in PR survival in RP models when animals were administered oral N-acetylcysteine (NAC) [32-34]. While oral and gene therapy approaches demonstrated promise to prevent or halt disease progression, they were not able to restore PRs or RPE that were already lost [35]. Cell and tissue replacement therapy offers an additional avenue for hope to patients with advanced retinal degeneration. Transplantation of hPSC-derived RtOgs offers one pathway to replace segments of dead tissue.

Rodent models used in transplantation studies are summarized in **Table 2.1**. Mutations in rodent models primarily yielded retinal degeneration marked by PR loss. Preclinical studies have also focused on immune rejection of transplantable RtOg materials. The native retina is known to be immune-privileged similar to the brain [19]. A recent study showed that RtOgs elicited minimal immune response when transplanted [36], thereby allaying some concerns for future clinical application. However, to use allogeneic cells for transplantation research, immune rejection is still an important factor to consider in the long term [37], as cell rejection can occur months after transplantation [38]. Human RtOgs xenografted into animal models raises concern of heterologous tissue rejection. Zhu

et al. reported that immunosuppression before transplantation allowed for better integration of graft cells and improved functionality [39]. Thus, for RtOg transplantation studies, immunosuppression remains a primary consideration, in which animal models for the studies may receive immunosuppression using pharmacological agents (e.g., Cyclosporine A, Mycophenolate, Tacrolimus), or genetically immunodeficient animals are used [18, 21, 40, 41].

Table 2.1: Summary of Rodent Disease Models

Rodent Diseases models	Gene modification	Affected cell type	Degeneration time frame	Refs
rd1 mice	• Null mutation in the Pde6-β	• Rod Photoreceptor cells	• 97% of rods lost by P17 and cone apoptosis around P30 • Loss of a functional ONL by 6-10 postnatal weeks	[42-46]
rd1/Foxn1 nude mice	• Null mutation in Pde6-β • Null mutation in Foxn1	• Photoreceptor cells • Immune cells (no T-cells)	• Immunodeficient • Complete loss of rods • Absence of Mouse Cone Arrestin^{+} cells from the central retina at 3 months postnatal	[47]
NOG-rd1-2J mice	• Pde6-β allele from rd1 mouse into NOG mice	• Photoreceptor cells • Immune cells (loss of T-, B- and NK cells)	• Immunodeficient • Loss of photoreceptors within 3-4 postnatal weeks	[48]
L7-GFP/*rd1* mice	• Crossing *rd1-2J* and L7-GFP mice	• Photoreceptor cells	• Labeled bipolar cells • End-stage RD marked by the loss	[23, 49]

		• Rod bipolar cells express GFP		of majority of rod cells by P30	
IL2rγ$^{-/-}$ mice	• IL2rγ knockdown; • Crx mutant.	• Photoreceptor cells (slow photoreceptor degeneration • Immune cells (10-fold reduction of lymphocytes, absence of NK cells)	• Immunodeficient • Mutation in the Crx gene leads to congenital blindness		[39]
Cpfl1/Rho$^{-/-}$ mice	• Rhodopsin knockdown; • Cpfl1 mutation, cone function loss	• Photoreceptor cells (dysfunctional rods and cones)	• 2-3 rows of photoreceptors at the age of 9 weeks		[46]
SD-Foxn1 Tg(S334ter)3 LavRrrc nude rats	• Crossing SD-Tg(S334ter)3Lav rat and NTac:NIH-Whn rats.	• Photoreceptor cells • Immune cells (loss of T-cells)	• immunodeficient • Loss of ONL thickness and photoreceptors as early as P30 • Loss of most photoreceptor by 10 postnatal weeks		[18, 50, 51]
RCS nude (Hsd:RH-Foxn1rnu) rats	• Deletion in the Mer tyrosine kinase (MerTK) receptor. • Null mutation in Foxn1	• RPE cells • Immune cells (loss of T-cells)	• immunodeficient • Failed RPE phagocytosis, causing outer segment debris accumulations and leading to photoreceptor death		[21, 52]

2.3 RtOgs Culture and Analytical Methods

2.3.1 Stage Specific RtOgs Development

Culture protocols for pluripotent stem cell (PSC)-derived Mouse and Human-RtOgs were summarized and evaluated in previous reviews [53-55]. Although timing is different, in most protocols, the basic procedure consists of two steps: 1) initiation of embryonic bodies (EBs) from stem cells by neuro induction media; and 2) long-term differentiation of RtOgs by adding retinal differentiation media. Stage specific morphologies are shared by PSC-derived RtOgs regardless of induction protocols. Capowski *et al.* identified three distinct morphological stages of RtOg development by investigating 16 hPSC lines [56] (**Fig. 2.1A-C**). RtOgs in stage 1 are characterized by a neuroblast layer, rich in RGCs and rare ACs. Stage 2 RtOgs represent a transition period, when different cell types such as PRs, HCs and ACs start to differentiate and RGCs start to degenerate. Lastly, stage 3 RtOgs are marked by PR layer and outer segment structures with very few RGCs left in the inner layer. The emergence of Müller glia (MG) that form the structural framework of RtOgs is also one of the stage 3 markers [56]. The stage-specific morphological features are accompanied by a shift in metabolic activity, which was confirmed by recent research. Xue *et al.* identified these three stages of RtOgs differentiation by analyzing the free to bound nicotinamide adenine dinucleotide (NADH) ratio of the RtOgs' surface using fluorescence lifetime imaging microscopy (FLIM) [2]. RtOgs in the early stage were more glycolytic because they mostly consisted of progenitor cells. During the differentiation stage, a metabolic shift from glycolysis to oxidative phosphorylation was observed (**Fig. 2.1**). At the maturation stage, the RtOgs developed glycolytic PR layers [2].

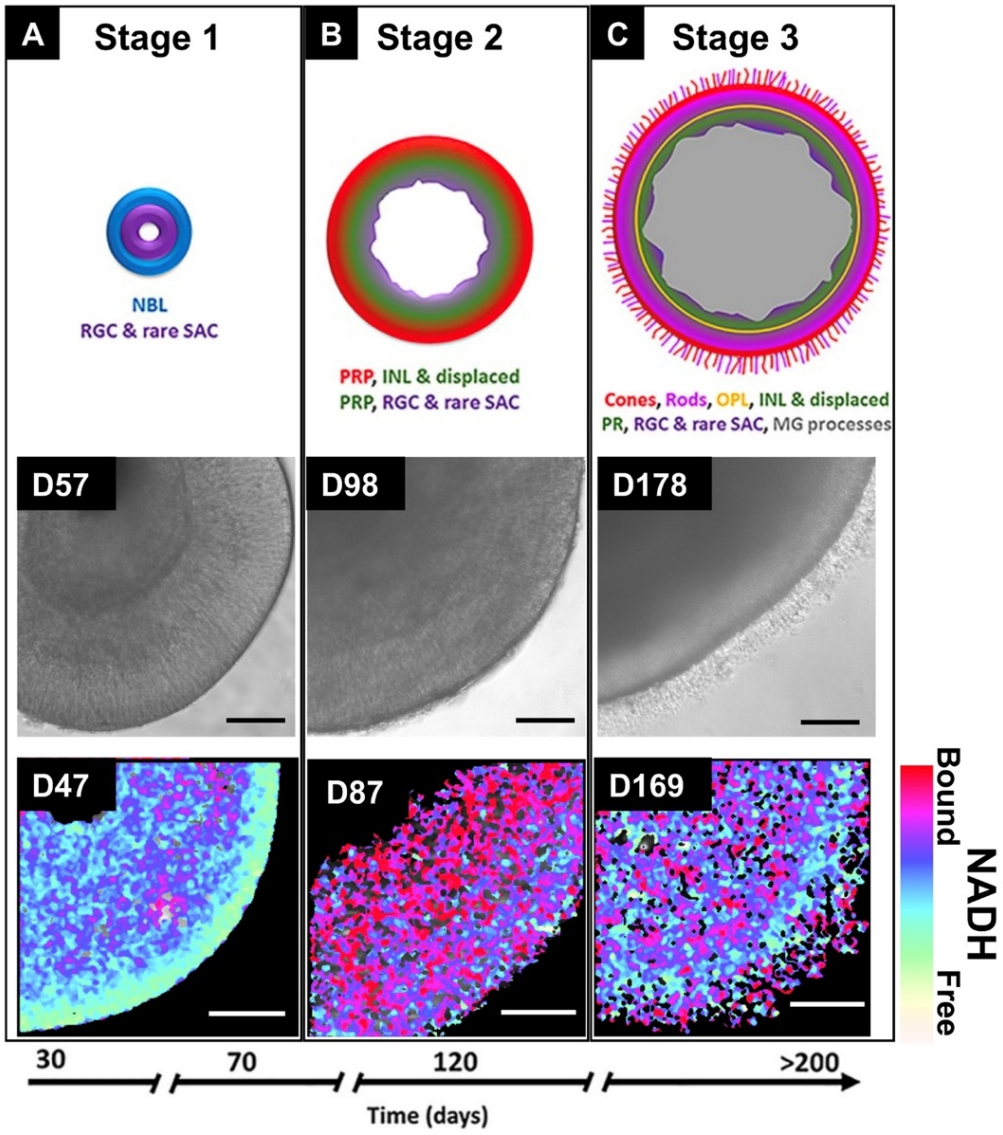

Figure 2.1: Three developmental stages of retinal organoids as shown by phase contrast microscopy and FLIM imaging.

The schematic diagram in the first row was taken from [56] (Figure 10 republished with permission of The Company of Biologists Ltd, from Capowski *et al.* Reproducibility and staging of 3D human retinal organoids across multiple pluripotent stem cell lines. *Development* 2019;146:dev171686. DOI: 10.1242/dev.17168; permission conveyed through Copyright Clearance Center, Inc.). The FLIM NADH map in the third row was taken from [2] (Figure 1A) (Scale bars: second row – 200 μm; third row – 50 μm).

2.3.2 RtOg Differentiation Methods

Methodologies for optimizing RtOgs quality published in recent years can be categorized into three types: 1) adjustment of the supplemental reagents in culture media; 2) testing different EB formation approaches; and 3) investigation of alternative 3D suspension culture approaches beyond conventional tissue plate culture.

For the first category, Zerti *et al.* found that addition of specific reagents such as retinoic acid and triiodothyronine (T3) at selected differentiation duration stages could provide high quality RtOgs that contained specific PR subtypes [57]. Protocols to accelerate development of rod PRs by supplementing with 9-cis retinal are reported [58-60]. Pan *et al.* employed COCO (a multifunctional antagonist of the Wnt, TGF-β, and BMP pathways) to promote RtOg differentiation. They found increased number of PR precursors in early stage RtOgs (main difference observed were CRX+ cells showing on Day 45). While the difference was not significant in later stages, they found COCO treatment reduced NRL, RHO, and green opsin (OPN1MW) expression and increased blue opsin expression (OPN1SW), which indicated that an enhanced fate of cones and decreased fate of rods were apparent in late stages [61].

The latter two categories will be expanded in the following paragraphs according to the chronological order of RtOg differentiation.

In most differentiation protocols, the first step in RtOg production is to initiate EBs, which are 3D aggregates of pluripotent stem cells to develop into neurospheres. Different EB formation methods were tested by Mellough *et al.* [62] where they studied three approaches: 1) mechanical cutting, 2) enzymatic dissociation of stem cell colonies into small pieces, and 3) dissociation into single cells followed by force reaggregation [63, 64].

Their results showed that mechanically cutting EBs from 2D culture under static conditions (vs. shaker condition) produced most consistently laminated, mature and functional RtOgs [62].

Once EBs are formed, they are further differentiated in 2D matrix culture using growth factor reduced Matrigel or other hydrogels. When the eye field structures are formed, the RtOgs are excised and transferred to 3D suspension culture [65, 66]. Afterwards, the 3D culture continues for months while RtOgs follow typical gestational development and eventually develop mature PR layers on their outermost surface.
To improve 2D differentiation, Dorgau *et al.* placed EBs onto an extracellular matrix that contained decellularized peptides from neural retina and RPE. They observed an improvement in RPE differentiation, RtOgs synaptogenesis, and light responsiveness [67]. Compared to conventional extracellular matrix, decellularization provided necessary biochemical and biophysical components, as well as the biological scaffold for cell engraftment and differentiation [67].

However, the 2D differentiation on extracellular matrix is not necessary for all protocols. Hunt *et al.* skipped the 2D differentiation and encapsulated EBs into different hydrogels including RDG-alginate, hyaluronic acid (HA) and HA/gelatin hydrogels. They found that up to day 45 in culture, the 0.5% RGD-alginate enhanced the derivation of RPE and increased the yield of EBs compared to suspension cultured control group [68]. However, to confirm that hydrogel-assisted 3D differentiation is better than suspension culture, longer differentiation duration is needed. In another example, Kim *et al.* mixed hESCs aggregates in ice-cold Matrigel and dispersed in medium supplemented with N2 and B27 on day 0 for floating culture. They transferred the single-lumen cysts to 24-well plates

for attachment culture on day 4-5, and enzymatically lift by Dispase on day 15 with 3D RtOg culture immediately initiated. Using this protocol, they successfully developed cone-rich RtOgs, which are of particular interests in transplantation studies [69].

Some studies for RtOg production focused on improving the long-term 3D differentiation of RtOgs. Besides conventional 3D suspension culture in tissue culture plates, several research teams designed and fabricated autonomous long-term culture devices to improve RtOgs long-term culture quality and to reduce variability. Ovando-Roche *et al.* applied a stirred-tank bioreactor to culture RtOgs and improved the laminar stratification and increased the yield of PR cells [70]. Similarly, DiStefano *et al.* used a rotating wall vessel (RWV) for RtOgs 3D culture and as a result accelerated differentiation and improved overall quality [71]. Micro- and/or millifluidic bioreactors can minimize shear stress on developing RtOg while allowing targeted long-term imaging and reduce the total culture medium consumption [1, 72, 73]. Xue *et al.* developed a shear stress-free micro-millifluidic bioreactor that produced RtOgs with comparable quality as those in static culture, while allowing real time functional imaging with the all-transparent design [1]. Studies comparing RWV and low-shear systems will address whether shear stresses damage the outer segment structures in mature organoids.

2.3.3 RtOgs Validation and Characterization

The heterogeneity and variability of RtOg production necessitates validation of RtOg tissues prior to their use in downstream applications. Common methods for organoid validation include immunohistochemistry (IHC), flow cytometry (FCM), single cell transcriptomics [74] and single cell RNA sequencing (scRNA seq) [75-77]. Transmission

electron microscopy (TEM) enables visualization of micro/nano structures such as outer segments, inner segments with mitochondria, connecting cilia and disc structures. However, the detrimental nature of these commonly used methods is the mortal requirement to either fix the tissue or to dissociate the tissue into single cells. Destructive characterization halts organoid use in downstream applications including transplantation. Therefore, noninvasive and nondestructive characterization methods are gaining popularity in organoid research.

Several noninvasive characterization methods are reviewed in this article, including optical coherence tomography (OCT), confocal imaging of genetically-engineered reporters, FLIM and hyperspectral imaging (Hspec).

OCT was proposed for assessing 3D cultured RtOgs by Browne *et al.* in 2017 [78]. Further, OCT was implemented to visualize surface topography and internal anatomy by Capowski *et al.* [56]. Scholler *et al.* developed a dynamic full-field OCT system to achieve label-free visualization of organelle motility with sub-micrometer spatial resolution and millisecond temporal resolution [79]. OCT performs well in cross sectional and surface imaging. However, OCT cannot be used to identify cell types within RtOgs.

To visualize the lamination and cellular composition in RtOgs at cellular resolution, confocal laser scanning microscopy shows better performance. Pluripotent stem cell reporter lines have been widely used for identifying cell lineages, subtypes and RtOg's developmental stages in live culture. Using CRISPR/Cas-9 genome editing, Philips *et al.* created the first human rod reporter line, which tagged GFP to the Neural Retinal Leucine zipper (NRL) gene of the WA09 hESC line [80]. Using zinc finger nuclease technology, Collin *et al.* generated a Cone-Rod Homeobox (CRX)-reporter hESC line [81], which could be

applied to isolate PR precursors [81] and for use in transplantation [45]. Vergara *et al.* developed a 3D automated reporter quantification (3D-ARQ) system to effectively monitor the RtOgs' developmental process, fluorescence intensity changes, reproducibility evaluation and realized high throughput screening [82]. Compared to reporter lines that required genetically-engineered fluorescence label, two-photon imaging that integrates FLIM and Hspec on RtOgs can realize label-free imaging by exciting intrinsic fluorophores, offering the advantage of visualizing the metabolic signatures and molecular distribution within RtOgs [2, 78]. Further investigation is required to identify metabolic signatures with specific cell types.

Another important aspect is to evaluate the functionalities of RtOgs in advanced stages for light sensitivity and synapses generation. Common methods for RtOg electrophysiological functional analysis include patch-clamp [65, 83], fluorescent calcium imaging [84-86], two-photon microscopy [87] and micro-electrode arrays (MEAs) [88], reviewed by Afanasyeva et al [89]. In more recent studies, Li *et al.* systematically characterized the electrophysiology of RtOgs at different stages (D90, D150, and D200) using patch-clamp recording and found that photoreceptor cells in RtOgs after D200 showed similar characteristic currents as those in human retina [90]. Cowan *et al.* compared RtOgs with human retina in transcriptomes, and they further characterized the functionality of RtOgs by measuring the light responsiveness and imaging synaptic layers and functional synapses [91]. Furthermore, Bharathan *et al.* applied human RtOgs as a model system to study the synaptogenesis in human retina, identified stages of human outer plexiform layer (OPL) development and successfully recapitulated key aspects of synaptogenesis between PRs and bipolar cells [11].

2.4 Retinal Organoids for Transplantation

RtOg transplantation is becoming a promising therapeutic approach for retinal degeneration diseases. The current transplantation strategies for treating degenerative diseases can be categorized into four types: selected types of cells, transplanting RtOg sheets, RPE and co-graft of RPE and RtOg pieces. In this section, we summarize recent research of each method and discussed their pros and cons (**Table 2.2**; **Fig. 2.2**).

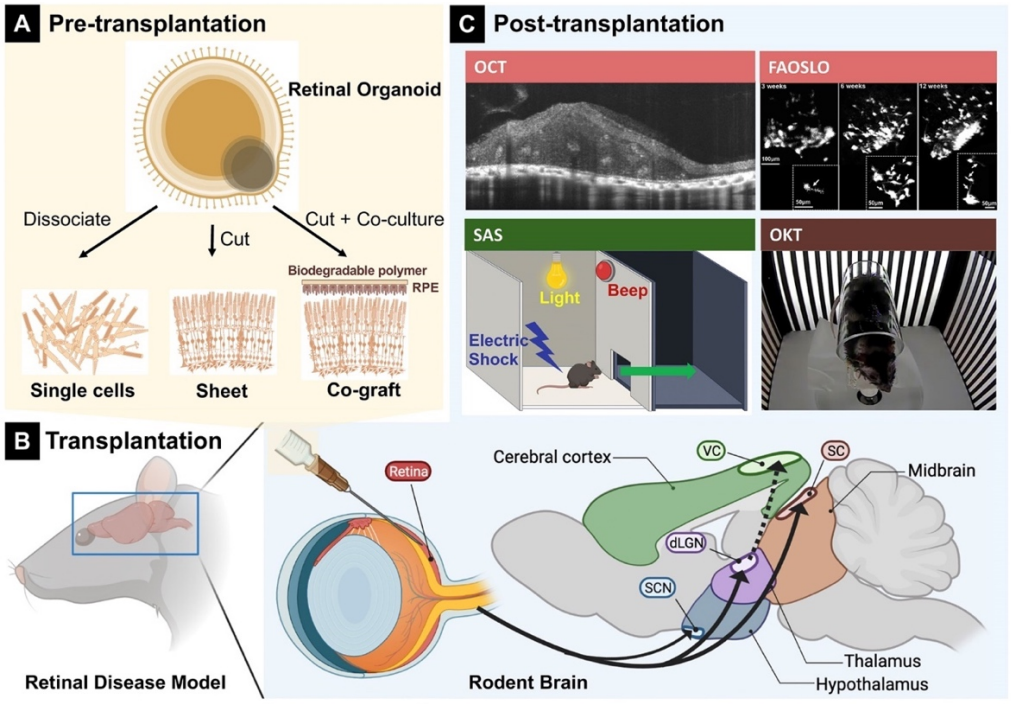

Figure 2.2: Overview of different transplant types from RtOgs and post-transplantation testing.

A) Three different transplant types obtained from RtOg: B) Schematic diagram of transplantation procedure. C) Post transplantation analysis that target on different regions in the brain. FAOSLO image was taken from [92] (Figure 4C); SAS schematic diagram was modified from [49] (Figure 3A). OCT and FAOSLO targeted on retina, SAS targeted on visual cortex (VC) and OKT targeted on superior colliculus (SC) (color-coded).

2.4.1 Transplant Selected Cells

Single-cell transplantation offers advantages including 1) targeted treatment for loss of certain cell types; 2) controllable purity and quality of the isolated cells; and 3) a potentially larger contact area between host and graft cells because the cells can spread over a larger area in the subretinal space.

So far, neural and retinal progenitors [49, 93], immature PR precursors [42, 94-98] and fully mature [99] PRs have been used for transplantation. Among them, immature but no longer dividing rod and cone precursor cells that can continue differentiation in the host retina are considered as the most feasible donor cell types [43, 100]. For cell selection and purification, fluorescence-activated cell sorting (FACS) was used. Lakowski *et al.* established a cell surface biomarker combination for PR precursor enrichment from hPSC-differentiated RtOgs and fetal retinae (CD73+/CD29-/SSEA1-) [43]. This combination of markers was also capable of eliminating mitotically active cells to avoid possible tumor development [43]. Collin *et al.* developed a hESC line that produced transplantable cone dominant PR precursors [45, 76]. Recently, Zerti *et al.* transplanted CRX-GFP labeled hESC-derived PR precursors (dissociated from 90DD RtOgs) (DD: days of differentiation) into end stage degeneration *Pde6brd1* mouse models. Light sensitivity restoration and up to 1.5% of cell integration into the putative host ONL were observed [42]. Ribeiro *et al.* transplanted purified cone precursors from human PSCs to immunodeficient rd1 mice and demonstrated vision improvements [47] (**Fig. 2.3A**).

Retinal progenitor cells are also a common source for transplantation. Chao *et al.* injected one million retinal progenitor cells into a nonhuman primate, *Saimiri sciureus*, and

observed extended axonal projections into the host retina and optic nerve without the need for immunosuppression for 3 months. No obvious PR integration was detected [101]. However, compared to sheet transplantation, single-cell transplants lack integrity and mechanical stability, which reduced the donor cell survival and further development within the host tissue. Cells injected as a bolus usually aggregated in the subretinal space but only a subpopulation would migrate into the host retina and there were issues with long-term survival [43, 102-104]. Further, the orientation of photoreceptor cells was also hard to control.

2.4.2 Transplant RtOg Sheets

Compared to single-cell transplantation, the advantages of transplanting RtOgs sheets are that 1) the RtOg sheet preserves the complete layered structure of retina, which is easier for integration into host retina; 2) the survival rate of transplanted tissue is higher due to the intact interneural connectivity; and 3) the tissue piece offers higher mechanical support and provides a better microenvironment for the retinal cells to differentiate and function.

Mandai *et al.* transplanted mouse iPSC-derived RtOg pieces (DD11-17) into end-stage rd1 mice model and observed light-responsive behaviors [49]. Iraha *et al.* transplanted hESC/iPSC-derived RtOg sheets (DD64 to 66) into immunodeficient IRD mouse models with the graft tissue showing long-term survival and maturation (DD200 to 220). Host-graft synapse formation was observed and light responses were detected from retinal wholemounts [48]. Tu *et al.* transplanted human iPSC-retinas (DD58 to DD78) into rhodopsin mutant SD-Foxn1 Tg(S334ter)3LavRrrc nude rats and performed IHC and

electrophysiology recording with a multi-electrode array (MEA) after sacrificing the animal (5 to 10.5 months). Light responses were detected at the grafted area in 4 of 7 transplanted rat retinas [50]. In the same study they also transplanted RtOgs (DD62 and DD53) into a cynomolgus monkey and a rhesus monkey. Visually-guided saccades (VGS) test revealed a mild recovery of light perception after 1.5 years of transplantation in rhesus monkey [50]. In different studies, RtOg sheets (DD 30-65 and 70) were transplanted into immunodeficient rhodopsin mutant SD-Foxn1 Tg(S334ter)3LavRrrc nude rats [18] (**Fig. 2.3B**) and immunodeficient RCS rats [21]. Improvement of visual responses was demonstrated by optokinetic tests and recording from the superior colliculus in both IRD models. Interestingly, RtOg transplants improved visual responses in RCS rats in spite of the absence of functional RPE cells. PR development and synaptic connectivity were identified with IHC.

However, the disadvantage of this method includes the requirement of a highly-trained operational skillset and a larger retinal incision compared to transplantation of dissociated cells since the RtOg sheet needs to be placed flat into the subretinal space in the correct orientation. Also, uniformity and retinal cell purity of the RtOg sheets are critical to avoid tumorigenesis or fibrosis resulting from contamination with undifferentiated or non-retinal cells. In addition, although the transplants form retinal layers, PRs frequently form spherical structures called rosettes, with PR outer segments in the center (mostly disconnected from RPE **(Fig. 2.3B**) [18, 21, 36, 49, 50]. This may be related to possible rosette formation in organoids before transplantation, and trauma to organoid pieces during transplantation.

2.4.3 Transplant Co-Graft of RPE and RtOg Sheet

Besides RtOg sheets, PSCs-derived RPE is also a promising tissue source for transplantation and vision restoration. RPE plays critical roles in vision by performing vital functions such as 1) transporting nutrients, ions and water to the PRs, 2) supplementing 11-cis-retinal in the visual cycle by isomerization of all-trans-retinal, 3) protecting against photooxidation and light absorption, 4) removing shed PR outer segment membranes with phagocytosis, and 5) secreting essential extracellular molecules (e.g. laminin, collagen and hyaluronic acid) to maintain retinal integrity, functionality and PR viability [105, 106]. Several studies used hESC/iPSC derived RPE sheets (or "patches") for retinal degenerative therapy in animal models [107-110] and clinical trials [111-114] (reviews [115, 116]). These studies reported maintenance or improvement of visual function and delated retinal degeneration. However, this approach has not been successful in stopping disease progression.

Considering the limited performance of mere RPE or RtOg transplantation, some research groups proposed that combination of these two tissues might provide enhanced effects. Early studies found that *in vitro* co-culture of rat neural retina and RPE cells promoted PR integration and axonal growth by increasing the synthesis of rhodopsin [117]. Further, reduced apoptosis, gliosis and increased glutamate synthesis were observed compared to retinal culture alone [118]. However, since the culturing conditions are different for RPE and RtOg, the co-cultures of these two tissues were usually short-term in the range of a few days [117, 118]. As a result, it was challenging to co-culture RPE and RtOg to the stage ready for transplantation.

A more promising option was to culture RPE and RtOg separately until ready for transplantation, and then put them together with bio-adhesives as co-graft and transplant

into the host [52]. Previous research demonstrated the feasibility of transplanting grafted sheets of fetal retinal progenitor cells with its RPE into animal models [51, 119] and human [120] to address the challenges of the lack of physical cell-cell interactions and undesirable host environment for development [121]. However, the use of fetal retina was ethically controversial, and access to the tissue has been very limited. Recently, Thomas *et al.* combined RtOgs and polarized RPE sheets using bio-adhesives (gelatin, growth factor-reduced Matrigel, and medium viscosity alginate). Long-term survival (up to 6.5 months) of the co-graft in immunodeficient RCS rats' subretinal space and improvement in visual function were observed [52] (**Fig. 2.3C**). This study has proven the feasibility of co-graft transplantation for severely degenerated retina [52]. Challenges remain due to the complexity of the donor tissue preparation and rosette formation in the RtOg transplants.

2.4.4 Transplant with Biomaterial Scaffolds

Researchers also turned to engineering approaches to realize outer retinal reconstruction. Specifically, biomaterial scaffolds constructed by synthetic polymers, silk, alginate, hyaluronic acid and extracellular matrix were used as reviewed by Hunt *et al.* [122]. Recently, Lee *et al.* designed and fabricated an ultrathin (30 μm) biodegradable scaffold patterned with micrometer-level precision [123], which was called "poly(glycerol sebacate) (PGS) ice cube tray". Compared to their previous "wineglass" design [124] that only achieved single-layer PR seeding, the ice cube tray design supported multiple layers of hPSC-PRs with more than 300k cells in a single 5-mm diameter scaffold similar to the area of a human macula. This design presented slower degradation *in vitro* (up to 30 days)

[123]. However, more investigations are needed to scale up manufacturing, delivery strategies to animal models and *in vivo* functional tests.

Table 2.2: Advantages and Disadvantages of Three Tissue Sources for Transplantation

Tissue type	Advantages	Disadvantages	Refs
Single cells	• Larger contact area between host and graft tissue likely improved chance of integration; • Targeted treatment for loss of certain cell types and avoiding inappropriate synapse formation; • Easy control of purity and quality of cells to avoid tumorigenesis.	• Lacks integrity and mechanical stability; • Reduced survival rate prevented further development within the host tissue; • Difficult to control the orientation of photoreceptor cells in the graft; • Cytoplasmic transfer to host cells if host ONL was present resulting in rescue of host photoreceptors but not replacement.	[39, 42-47, 98, 101, 125]
RtOg sheet	• Complete layered structure of retina easier for integration into host retina; • Intact interneural connectivity improved survival rate; • Higher mechanical support and better microenvironment for the retinal cells to differentiate and function.	• Highly trained surgical skills required. • Uniformity and retinal cell purity within the ROs sheet critically needed to avoid tumorigenesis or fibrosis; • Potentially excessive and inappropriate bipolar to bipolar cell synapses between graft and host. • Rosette formation.	[18, 23, 48-50]
RPE-RtOg co-graft	• Physical cell-cell interactions between RPE and photoreceptor layer already formed at time of transplantation.	• More complex tissue culture and preparation process before transplantation;	[52]

	• Reduced apoptosis, gliosis and increased glutamate synthesis; • Improved developmental environment in the host retina.	• Extensive manual labor required to transplant the co-graft tissue; • RtOg transplants still forming rosettes; optimal embedding matrix yet to be determined • Rosette formation.

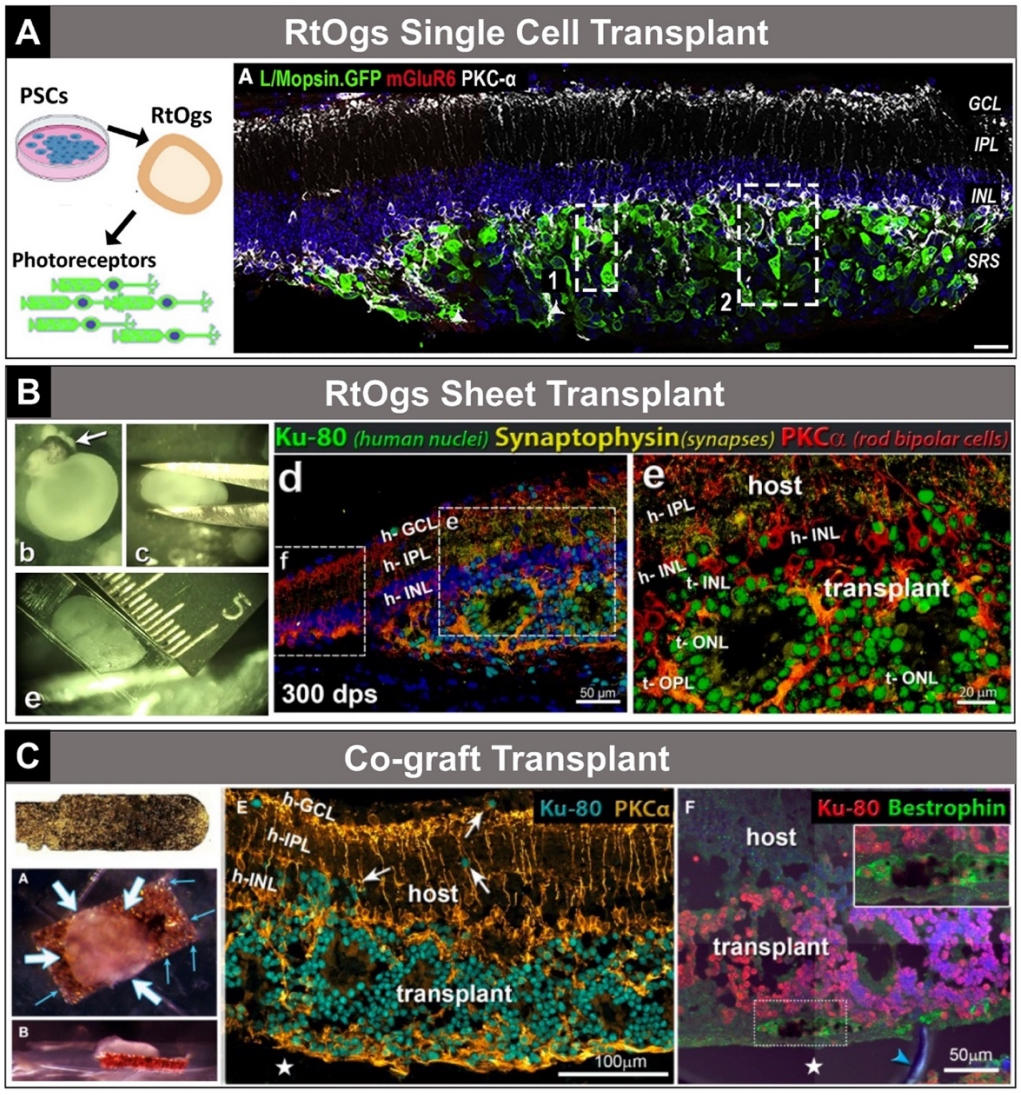

Figure 2.3: Transplantation examples– single cell, sheet, co-graft.

A) Single cell transplantation. Taken from [47] (graphical abstract; Figure 3A). B) Sheet transplantation. Taken from [18] (Supplemental Figure 1; Figure 7 d, e; republished with

permission of Investigative Ophthalmology & Visual Sciences, from McLelland *et al.* Transplanted hESC-derived retina organoid sheets differentiate, integrate, and improve visual function in retinal degenerate rats. *Invest Ophthalmol Vis Sci* 2018;59:2586-2603; DOI 10.1167/iovs.17-23646; permission conveyed through Copyright Clearance Center, Inc.). C) Co-graft transplantation. Taken from [52] (Figure 1 I; Figure 3 A,B; Figure 7 E,F).

2.5 Post-Transplantation Analysis

Finally, to evaluate the effectiveness of transplantation, different post-transplantation tests have been performed with animal models. The host used in these studies had intact neural pathway from the optical nerve to the visual cortex, despite the loss of PRs (**Fig. 2.2C**). Therefore, the transplantation performance was a direct result of the integration, differentiation and function of the grafted tissue within the host retina. Thus, post-transplantation tests normally focused on examining the following performance: 1) light and contrast sensitivities and visual acuity of subjects with behavioral tests; 2) connectivity of the visual pathway between retina and visual cortex with retinal and brain electrophysiology recordings; and 3) integration, differentiation and synaptogenesis between graft and host tissue with OCT, histology and analysis of retinal and synaptic markers in correlation to functional results. Common post-transplantation tests are categorized and summarized in **Table 2.3** and shown schematically in **Fig. 2.2**.

2.5.1 Behavioral Tests

Behavioral tests are advantageous because they are noninvasive and can be repeated at any time points after transplantation. In particular, optokinetic test (OKT) is one of the most popular behavioral tests. Rodents show slow horizontal head and body movements when a virtual-reality visual field (black and white stripes of varying density)

is rotated around them. The stripe density eliciting a response determines the spatial threshold. For each eye, only a field rotation in the temporal-to-nasal direction evokes the tracking response, making it possible to distinguish between a transplanted and a non-surgery eye in the same animal. Lesions of the visual cortex had no effect on OKT, suggesting that OKT was driven by subcortical and contralateral pathways [126]. Several studies have shown improvements in optokinetic responses after RtOg sheet transplantation [18, 21, 52].

Multiple behavioral tests for visual functions had been used in different studies. For example, Mandai *et al.* adapted a shuttle-avoidance system (SAS) to test for light sensitivity and response in animals after transplantation. A warning light was presented to the mouse before an electric shock was administered to train the mouse to move into another chamber through a small opening as soon as it saw the warning light [49] (**Fig. 2.2C**). Similarly, a light avoidance system used bright light as a cue to test animal's light response capability [23, 42]. Another light avoidance test measured the animal's preference to evade light without using electric shocks [46, 47]. Tu *et al.* applied visually-guided saccades (VGS) test on rhesus monkeys, in which the animal facing a color LCD monitor was trained to gaze at a central fixation spot followed by a random presentation of a target spot somewhere else in the monitor. The resulting saccades landing within a 50 x 50 pixels square containing the visual target were judged as correct responses [50].

2.5.2 Electrophysiological Tests

Global or full-field electroretinogram (ERG) represents mass electrical response of the retina to photic stimulation. The basic approach of global ERG is to stimulate the eye

with a bright light source such as a flash produced by LEDs or a strobe lamp while monitoring electrical activities in the eye. The flashes of light should elicit a biphasic waveform (the a- and b-waves) recordable from the cornea. Full-field ERGs are in general not sensitive enough to detect visual improvements once retinal degeneration has progressed too far. E.g., Lin *et al.* could only detect ERG response improvements at 2 months post-transplantation of RtOg sheets to immunodeficient RCS rats [21] but rodent models with more severe retinal degeneration had never shown recordable ERGs [127]. To circumvent this shortcoming, MEA-based micro-electroretinography (mERG) technique was used to ascertain the effectiveness of transplantation [46, 48-50]. Compared to full-field ERGs, which only detected changes in mass retinal field potentials, local and multilocal ERGs offer higher signal-to-noise ratio and thus are more suitable for tracking degenerative processes or functional recovery. Fujii *et al.* has tested an MEA-based mERG system on rd1 mice with progressive PR degeneration, and were able to record light-evoked mERGs with consistent RGC spike responses [128]. Garita-Hernandez transplanted optogenetically transformed iPSC PR precursors, to *Rho-/-* mice. They were either derived from neonatal mice expressing *Natronomonas pharaonis* halorhodopsin (NpHR) coupled to a rod promoter; or derived from iPSC-RtOgs expressing hyperpolarizing chloride pump *Jaws*, a redshifted cruxhalorhodopsin couple to a cone promoter [46]. Function of the transplanted PRs was demonstrated by behavioral tests (light-dark box), MEA recordings, and patch-clamp recording from GFP+ donor PRs (in the absence of functional outer segments) that were specific for the action spectrum of these bacterial opsins (580 nm) [46].

Another very sensitive technique is electrophysiological recording from the superior colliculus (SC) [18, 21, 52] in the midbrain, which plays a central role in

integrating multiple sensory inputs to motor behaviors such as eye and head movements [129]. In this test, a microelectrode is directly placed on the surface of SC; under full-field retinal stimulation at specific light intensities, visual thresholds and visual responses (spike counts) of specific retinotopic areas of the SC were recorded.

2.5.3 In vivo Imaging Tools to Determine Transplant Survival and Differentiation

Spectral-domain OCT (SD-OCT) is widely used to examine the transplanted regions [18, 21]. SD-OCT offers high axial resolution to show different layers of the retina and visualize the transplanted region thickness. However, SD-OCT cannot provide specific morphological information, and the resolution is not high enough to visualize single cells. Aboualizadeh *et al.* studied the dynamic nature of transplanted cells at cellular resolution utilizing near infrared fluorescence adaptive optics scanning light ophthalmoscopy (FAOSLO). They tracked the survival, migration and neurite outgrowth of individual fluorescent PR precursors in the living monkey eyes in the long-term [92] (**Fig. 2.2C**). Similarly, Liu *et al.* applied confocal scanning laser ophthalmoscopy (cSLO) to evaluate *in vivo* biomarkers of transplanted PR cells qualitatively and quantitatively. They were able to observe migration of the transplanted tissue as well [44]. While these two techniques demonstrated high resolution and dynamic imaging, it relied on genetically engineered reporter cell lines ($CRX^{+/tdTomato}$ and $Rho^{+/GFP}$) to emit fluorescent light, which is not applicable for future clinical use in human subjects.

2.5.4 Analysis of Transplant Differentiation and Connectivity

RtOg sheets and retinal progenitor cells derived from RtOgs were usually transplanted while they were in an immature state to facilitate integration and further

development in the host. IHC for specific retinal markers was commonly used to identify the differentiation within the transplant over time (e.g., [18, 48, 49]).

A critical indicator of transplanted tissue viability was the formation of synapses between neurons or within the photoreceptor ribbon synapse. IHC was considered a robust and high throughput analytical tool to visualize synaptogenesis. This included combining donor label with staining for synaptic markers [18, 21, 48]. Akiba *et al.* has proposed an automatic synapse quantification method that could not only quantify the number of synapses, but also estimate the probability of "synapse-ness" from IHC images. This method was named as "Qualitative and Quantitative Analysis using Bayes Theorem Optimized for Synapse Evaluation (QUANTOS)" [20]. Because the transplanted RtOg sheet also contained bipolar cells, which might cause inappropriate bipolar to bipolar cell synapses between graft and host, Matsuyama *et al.* generated mouse RtOg retinal sheets with reduced numbers of retinal bipolar cells and demonstrated improved visual recovery and better integration after retinal transplantation [23]. Similar results were achieved with genetically modified human RtOgs [130]. He *et al.* transplanted retinal progenitor cells derived from mouse C-Kit-mXCherry and Rosa-lsl-CGaMP5 mESC-derived retinal organoids to the subretinal space of 21d-old RCS rats [131]. Retinal progenitor cells expressing CaMP5 were enriched by cell sorting for C-Kit. Transplanted cells were observed to have migrated into the degenerating retina. The development of functional synapses was shown by IHC for pre- and postsynaptic markers and with 2-photon calcium recording of donor cells [131].

2.5.5 Cytoplasmic Material Transfer Between Transplant and Host

Several studies in recent years have demonstrated that transplanted dissociated PR precursors exchanged cytoplasmic material (proteins and RNA) with remaining host PRs and thus might result in rescue of host PR function [102-104, 132, 133] (review [134, 135]). This transfer can be bidirectional, from donor to host and vice versa [102, 132, 133]. In addition, transfer of mitochondria between mesenchymal stem cells and different ocular cell lines has been demonstrated *in vitro* [136]. This may explain the beneficial effect of transplants on host PRs. It was thought that material exchange required PR-to-PR communication, which could not occur in severe retinal degeneration when the PR layer is completely gone [134, 137]. Cytoplasmic transfer between PRs also occurs during normal retinal development [138]. However, transfer can also be seen from PRs to the MCs and ACs in the inner nuclear layer when grafting cells to rats with normal outer nuclear layer [102]. Thus, the identity of donor cells in the host retina needs to be clearly demonstrated by nuclear labels (e.g., male donor into female host [46, 102, 104, 132], or a human nuclear marker for hPSC-derived transplants in rodent hosts [18, 21, 50]).

Table 2.3: Summary of Post-Transplantation Tests

Categories	Methods	Examined Features	In vivo	Refs
Behavior tests	Shuttle avoidance test (SAS)	• Light-dark discrimination • Light threshold (shock)	Yes	[23, 42, 49]
	Light avoidance test	• Light-dark discrimination	Yes	[47]
	Optokinetic tracking (OKT)	• Visual acuity • Contrast sensitivity	Yes	[18, 21, 52]
	Visually-guided saccades test (VGS)	• Eye movement: Latency, amplitude and peak velocity	Yes	[50]

Electrophysiology	Electroretinogram (ERG)	• Electrical activity of retina in response to light stimulation	Yes	[21]
	MEA based mERG (micro-ERG)	• Local electrical potential changes evoked by light	No	[46, 48-50]
	SC recording	• Spike counts after light stimulus (different light intensity) • Correlate visual responses in SC to certain retinal areas	Yes	[18, 21, 52]
Graft differentiation, integration and synaptogenesis	SD-OCT	• Location and overview of transplant • Graft thickness	Yes	[18, 21, 52]
	Fluorescence adaptive optics scanning light ophthalmoscopy (FAOSLO)	• Survival, migration and neurite outgrowth of fluorescent labeled transplant cells	Yes	[44]
	IHC	• Labels specific proteins in tissue to reveal certain cell types, synapses and the overall structure of transplant and host	No	Most studies applied

2.6 Conclusions

In conclusion, methods to derive RtOg from pluripotent stem cells have significantly improved and become more efficient in recent years. Meanwhile, more novel technologies are applied to characterize and validate RtOg quality. However, there is still room for differentiation protocol optimization to achieve better RtOg reproducibility. In order to screen high quality RtOgs for downstream applications, approaches such as non-invasive and label-free imaging, and electrophysiological functional testing are promising and worth

more investigation. Lastly, transplanted RtOg-derived tissues have allowed improvements in visual function in several retinal degeneration models, and this is promising for clinical applications in the future.

Chapter 3 : Retinal organoids on-a-chip: a 3D printed micro-millifluidic bioreactor for long-term retinal organoid maintenance

3.1 Introduction

Retinal degeneration (RD) is a leading cause of vision impairment and blindness worldwide. Visual degeneration can originate in any of the cell types in the retina. Some of the more common visual degenerations arise from death and/or dysfunction of the photoreceptors (PR) and retinal pigmented epithelial (RPE) cells**.** Irreversible cell damage is the root to vision loss in diseases like age-related macular degeneration (AMD) and retinitis pigmentosa (RP)[139, 140]. Retinal sheets and dissociated retinal cells are candidates for retinal tissue replacement therapy. However, both tissue sources have inherent limitations. Historically, retinal sheets derived from fetal neurosensory retina and RPE transplanted into the subretinal space demonstrated utility to restore vision and neurosensory functions [127, 141-146] in animals [147-149] and humans [120]. However, the use of fetal tissue carries complex social, ethical, and political implications. Transplantation of dissociated photoreceptor precursors overcomes the ethical issues intrinsic to fetal tissues and demonstrated some visual function improvements [150, 151]. However, transplantation of dissociated cells [94, 152-154] suffers from insufficient cell type differentiation, lack of cellular polarization and eventual cell death.

With the advent of new techniques to manipulate human embryonic (hESCs) [155] and induced pluripotent stem cells (iPSCs),[156] stem cell-derived retinal organoids (RtOgs) have emerged as tools that exhibit the combined advantages of retinal sheets and differentiated retinal cells. RtOgs are 3D spheroids that arise from stem cells and self-

organize into layered retinal tissues containing retinal ganglion cells, rods and cones [63, 157, 158]. Transplantation of RtOgs have been shown to restore vision in retina degenerated rats [159], mouse [160] and primate [161] models with RD. Even so, current state-of-the-art RtOg production methods are highly heterogeneous due to their use of different stem cell lines, tissue maintenance methods, high manual labor and imprecise tissue selection for use in multiple applications [53]. A comparative study revealed that RtOgs differentiated from iPSCs showed stage specific, cell line and methodological differences [62]. This heterogeneity and imprecision limit human RtOg procurement for preclinical trials [53] and *in vitro* investigations. Many approaches, including bioreactors [70, 71, 162-166] and optimized production protocols [53, 167] are investigated to standardize RtOg production and maintenance over months. Controlled and predictable RtOg production is important to ensure a quality-controlled tissue product that is suitable for transplantation.

In recent years, many *in vitro* cell culture platforms have emerged for organoid differentiation and maintenance at the macro- [168], milli- [169], and microscales [170]. Macro-scaled platforms are typically utilized for their ease and effectiveness in producing organoids, while milli-scaled systems (≥ 1 mm) are employed to achieve relatively high flow rates and to study cell-cell interaction. Milli-scale systems also reduce frequent media changes, therefore mitigating organoid perturbation and probability for damage [163]. Considering the costs associated with the relatively high media volumes required by the macro-scaled bioreactors, microscale devices (< 100 μm) are steadily growing in popularity [171]. Microfluidic devices share the advantages of millifluidic devices, with the advantage of lower media consumption. However, the dimensional limits of traditionally fabricated

microfluidics devices hinder their application to organoids research since organoids are 3D spherical tissues that can grow up to several millimeters in size. **Fig. 3.1** summarizes published organoid bioreactors and their advantages and disadvantages. The integration of micro- and millifluidic features into a single device is a promising solution for organoids differentiation and maintenance.

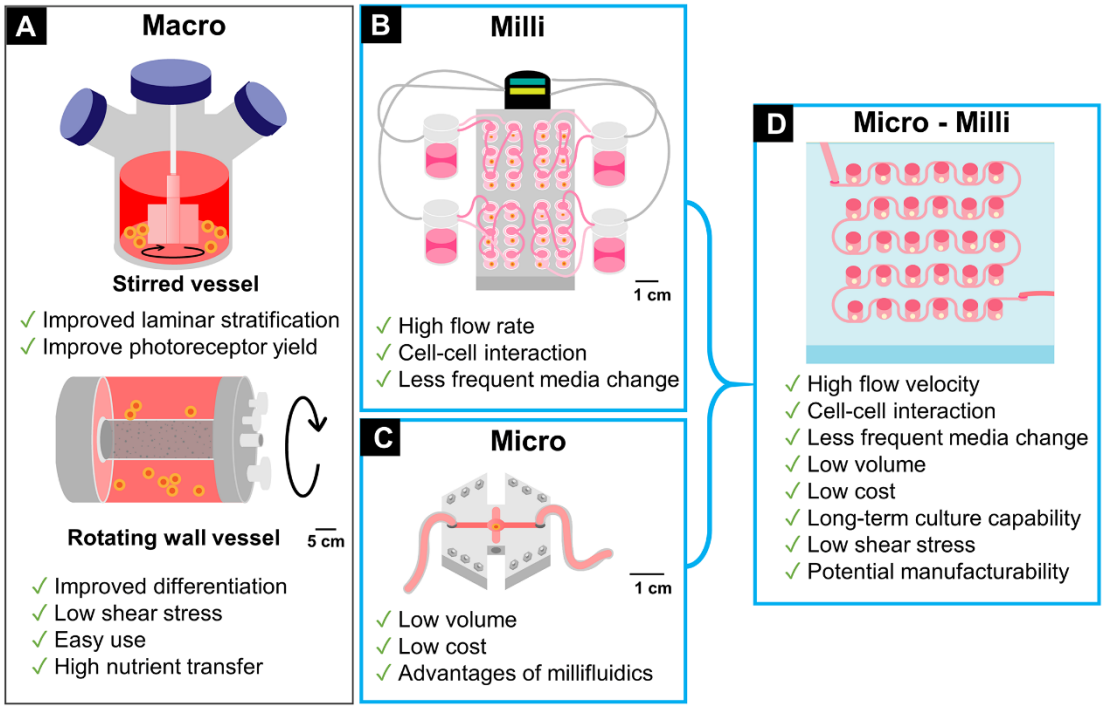

Figure 3.1: Review of Organoid Bioreactors.

(A) Macro scale bioreactors: stirred/spinning and rotating wall vessels [168]; (B) Millifluidic bioreactor [169]; (C) Microfluidic bioreactor [170]; (D) Micro-millifluidic bioreactor in this article.

In this study, we designed and fabricated a shear stress-free micro-millifluidic bioreactor for use in RtOg culture and maintenance. We used a high resolution (25 µm) stereolithography (SLA) 3D printer to fabricate the mold for Polydimethylsiloxane (PDMS) molding. 3D printed molds easily combine micro and millimeter features in one design with

very low cost and short manufacturing time. First, we simulated the fluidic design parameters in COMSOL to optimize the fluidic transports in the chip design. We evaluated 3 different factors that could affect mass transfer efficiency and uniformity. We then successfully cultured RtOgs in 3 different differentiation stages on the designed chip platform for more than one month (31~37 days). Finally, we did a comparative study to characterize the RtOgs produced by dish culture (denoted as "static" because there was no constant media flow through the dish) and chip culture. We studied living organoids and fixed organoids post-vivo using qualitative and quantitative methods.

3.2 Methods

3.2.1 COMSOL simulation

The simulation was performed using finite element analysis software, COMSOL Multiphysics (COMSOL, Inc, Palo Alto, CA, USA). COMSOL was used to evaluate different chip designs and flow channel configurations to optimize mass-transport dynamics in culture chambers with different heights. Three major factors that affected the mass transfer rate were taken into consideration: 1) channel width (1000 or 500 μm wide), 2) channel configuration relative to culture chambers (linear single-sided chambers, serpentine alternating side chambers, serpentine with integrated mixer) and 3) the culture chamber height (2 or 4 mm tall).

The simulation parameters are listed in **Table 3.1**. The initial concentration of the whole system was set to zero, which was considered the most extreme condition. The left end of the channel was set as the inlet with concentration of 1 mol/m^3 as the boundary condition.

Table 3.1: Simulation parameters

Physics	Laminar flow & Transport of diluted species
Study type	Time dependent
Material	Water
Diffusion coefficient (m^2/s)	6.00E−10
Boundary conditions (mol/m^3)	$c_{initial} = 0$, $c_{inlet} = 1$

3.2.2 Chip design and fabrication

The mold was designed using SolidWorks (SolidWorks Corp., Waltham, MA, USA) and the final design used for RtOg culture had the dimensions shown in **Fig. 3.2A** with channel height of 200 μm and chamber height of 2 mm. The chambers were arranged in a 6 x 5 array with the distance between each chamber at 9 mm, which was the same as that of a 96-well plate for compatibility with subsequent imaging steps. The mold was produced with 25 μm resolution with the Formlabs Form 3B printer (Formlabs, Somerville, MA, USA) using standard clear resin (Formlabs) (**Fig. 3.2B**). After printing, the mold was cleaned with 90% isopropanol to remove any resin residue. The mold was then air dried for 24 hours and cured with ultraviolet light for 30 minutes.

The bioreactor was fabricated from the printed mold similar to the molding steps in soft lithography [172]. Polydimethylsiloxane (PDMS) Sylgard 184 (Dow Corning, Midland, MI, USA) was mixed manually for 10 minutes at a 10:1 ratio (base elastomer/curing agent). After degassing in a vacuum chamber, the PDMS was poured over the 3D-printed mold until the level reached the top of the culture chamber features and degassed again in a

vacuum desiccator to remove bubbles (**Fig. 3.2C**). After 48 hours of curing under room temperature, the molded PDMS piece was carefully peeled off from the mold. The fluidic inlet and outlet were created with a biopsy punch. Finally, the PDMS piece was treated with air plasma (Harrick) (Harrick Plasma, Ithaca, NY, USA) for 1 min. to promote adhesion and then pressure-bonded to a cover slip (#1.5, 64*50 mm, ClariTex) (Ted Pella, Inc., Redding, CA, USA) (**Fig. 3.2D**).

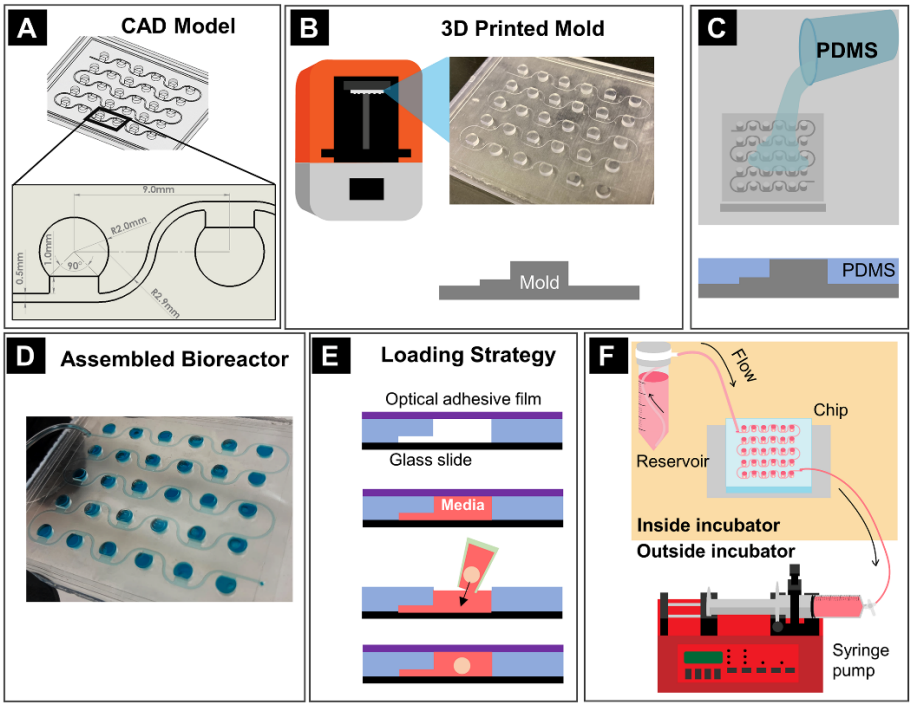

Figure 3.2: Fabrication methods.

(A) Mold design with CAD software; (B) Mold printing; (C) PDMS casting on the mold; (D) Assembled bioreactor; (E) Cross-section view of organoid loading procedure whereby microchannels were filled with media first, then an organoid was placed in the open well, and the wells were sealed using adhesive optical film; (F) On-chip culturing system assembly.

3.2.3 Stem cell culture and retinal organoids initiation

3.2.3.1 Stem cell line 1

Retinal organoids were differentiated from genetically modified NIH-registered cell line H9 human embryonic stem cells (hESCs) with green fluorescent protein (GFP) tagged to CRX gene which encodes cone-rod homeobox protein and is specifically expressed in photoreceptor cells [76, 81, 173]. Stem cells were maintained by feeding mTeSR 1 media (STEMCELL Technologies, Vancouver, BC, Canada) daily and passaged every 4-7 days by ReLeSR (STEMCELL Technologies) when cells reached ~80% confluency. Cells were expanded on Vitronectin XF™ (STEMCELL Technologies) coated plates at 37°C in a humidified 5% CO_2 incubator (Nuaire, Plymouth, MN, USA).

To initiate organoid formation, Accutase (Nacalai Inc, Kyoto, Japan) was added to the stem cells into a single cell suspension when 2-dimensional culture reached ~80% confluency. The cells were then placed in an 800-µm micro-well EZSPHERE 12-well plate (Nacalai USA, Inc., San Diego, CA, USA) and centrifuged at 100*g* for 3 min. to evenly distribute the stem cells throughout the bottom of each well. From day 1 to 7, the stem cells self-aggregated into embryonic bodies (EBs) in the EZSPHERE microwells. From day 8, the EBs were seeded onto a 1% growth factor reduced Matrigel (Corning, Corning, NY, USA) coated culture dish. The EBs spread onto the Matrigel and began 2D differentiation. Retinal eye fields were cut from the Matrigel between day 38 and 50 and transferred to ultra-low attachment 24-well plates (Corning Costar) (Corning, Corning, NY, USA) for 3D culture to be loaded into the bioreactor chip. Media used for retinal organoid differentiation was modified from Zhong *et al*. [174] From day 0 to 18, the organoids were gradually transitioned from mTeSR1 medium into neural induction media (NIM) containing Dulbecco's modified eagle medium (DMEM)/F12 (1:1) (Gibco, Waltham, MA, USA), 1% N2

supplement (Gibco), 1x minimum essential media non-essential amino acids (NEAA) (Gibco), 1x L-glutamine (Gibco), and 2 μg/ml heparin (Sigma-Aldrich, St. Louis, MO, USA), with daily media changes. From day 19 to 41, the media was switched to NIM containing DMEM/F12 (1:1) supplemented with 2% B27 supplement (50X) (minus vitamin A, Gibco), 1x NEAA, 1x L-glutamine, and 2 mg/ml heparin. From day 42 and beyond, the organoids were cultured with media containing DMEM/F12 (1:1) supplemented with 2% B27 Plus Supplement (50X) (Gibco), 1x NEAA, 1x L-glutamine, 2 ug/ml heparin, 100 μM taurine (Sigma), and 10% fetal bovine serum (FBS; Gibco). The media was changed 3 times a week and the organoids were maintained at 37°C in a humidified 5% CO_2 incubator.

On day 41, 87, and 128 of differentiation, 12~15 RtOgs were randomly selected to load one each into every other chamber in the bioreactor chip. After about one month (30~37 days) of on-chip culture, RtOgs were used for histology, single-cell RNA sequencing. Same tests for the same age RtOgs in static culture group were performed. The detailed information of experimental groups was summarized in **Table 3.2**.

Table 3.2: Summary of Experimental Groups

Cell line	Total time	Static & Bioreactor	PC	FLIM	IH	GFP	scRNA	qPCR	SEM TEM
CRX-GFP	D38-D72	D41-D72 (31 days)	**D41** **D71**	**D38** **D71**	**D72**		**D72**		
	D87-D124	D87-D124 (37 days)	**D88** **D124**	**D98** **D120**		**D98** **D120**		**D124**	
	D125-D159	D128-D159 (31 days)	**D158**	**D125** **D158**	**D159**		**D159**		**D159**
CSC-14	D70-D105	D70-D105 (35 days)						**D105**	

*PC – phase contrast imaging; FLIM – fluorescence lifetime imaging; IH – immunohistology; scRNA – single-cell RNA sequencing.

3.2.3.2 Stem cell line 2

We applied a second stem cell line in this study. The hESCs (cell line CSC14, NIH registration no. 0284; AIVITA Biomedical, Inc) were maintained on Matrigel coated flasks and cultured in a xeno-free custom formulated media supplemented with low levels of bFGF and Activin-A (Peprotech, Rocky Hill, NJ, USA). Media was replaced daily, and flasks kept in a 37ºC, 5% CO_2 tissue culture incubator. Every 4-5 days, colonies were passaged by enzymatic dissociation using collagenase IV (Gibco, 2 mg/ml) and transferred to a fresh Matrigel coated TC flask.

To initiate differentiation, growth factors are omitted, and media is replaced with a serum-free composition containing a GMP manufactured basal media, and Vitamin-A free B27 supplement (Gibco). Stem colonies are enzymatically released with collagenase IV (2 mg/mL) and aggregates allowed to form embryoid bodies (EB) for seven days in ultra-low adherence flasks. After seven days, EBs were transferred to Matrigel coated dishes and allowed to attach. Culture continues for 21 to 36 days with media replacement every 2-3 days. When refringent annular structures showing visible laminated morphology appear in the culture, these are the retina organoids to dissect and place in suspension culture. At day 55 of 3D culture, media is changed to B27 with Vitamin A (Gibco) and 10% (v/v) fetal bovine serum (Gibco) for long term culture. Retina organoids are fed every 2-3 days until needed.

Ten RtOgs on day 70 of differentiation were randomly selected and cultured on the chip for a month (35 days) until day 105. The organoids were divided into two groups for gene expression qPCR analysis afterwards. The same tests were performed for RtOgs in the static culture group.

3.2.4 Bioreactor system assembly and organoid loading

The chip and the associated tubing were disinfected with 70% ethanol and 30 min. in a UV and ozone cool clave (CoolCLAVE Plus) (Genlantis, San Diego, CA, USA). Each chamber was treated with anti-cell adherence solution twice (STEMCELL Technology) and washed by Dulbecco's phosphate-buffered saline (DPBS) without calcium and magnesium (STEMCELL Technology). The on-chip culturing system was assembled as shown in **Fig. 3.2F**. The media reservoir was comprised of a 50 mL Steriflip-GP sterile centrifuge tube (MilliporeSigma, Burlington, MA, USA) and a filter cap with a pore size of 0.22 μm. Before loading the organoids, the chip chambers were sealed by pasting a slice of MicroAmp™ optical adhesive film (Thermo Fisher Scientific, Waltham, MA, USA) on the top surface. Then the syringe was slowly withdrawn to apply negative pressure to fill the channel with fresh media drawn from the media reservoir. Tubing clamps were then applied to block both the inlet and outlet tubing, so that the adhesive film could be removed without disturbing the fresh media level in the channel. One organoid was loaded into each chamber by 20 μL pipette tips with tips cut off. Lastly, the top of the chambers was resealed with sterile optical adhesive film (**Fig. 3.2E**). The flow rate used for long-term culture was 250 μL/h. Under this flow rate, 50 mL media was sufficient for about 8 days of culture. When changing the media, the inlet and outlet tubing were clamped, and fresh media was

refilled in the centrifuge tube. All these steps were performed in an ESCO Class II Type A2 biosafety cabinet (Labculture, ESCO) (ESCO Micro Pte. Ltd., Singapore) to avoid contamination.

3.2.5 In vitro dye test

The dye test experiment was performed to compare the uniformity of the concentration in chambers between the four different channel designs. Four chips with 3x3 chamber array were fabricated with 2-mm chamber height. The channels were first filled with blue food dye solution following similar steps as the organoid loading procedure (**Fig. 3.2E**). The flow was then blocked by clamping both the inlet and outlet tubing, and the inlet was switched to a yellow dye solution. Lastly, a syringe pump was used to draw the yellow dye solution into the chip at a rate of 600 μL/h. The whole flow process was recorded with a camera. The grayscale value of each chamber was obtained by ImageJ to quantify concentration changes of each chamber from the images.

3.2.6 Fluorescence life-time imaging

Fluorescence lifetime imaging (FLIM) was used to study the intrinsic fluorophore Nicotinamide adenine dinucleotide (NADH) in the RtOg. The fluorophore's emission decay curve was obtained by photon counting to calculate the fluorescent lifetime (**Fig. 3.3A**). FLIM data was displayed on a phasor plot after Fourier transform, with the intensity decay curve of fluorescence for each pixel represented by the *g* and *s* coordinates. Using this method, the decay and spectrum for each pixel could be depicted on the phasor plot (**Fig. 3.3B**).

The metabolic trajectory was visualized using the phasor approach [175]. The phasor plot has a universal circle, with boundaries of each point representing a single exponential lifetime of one type of molecule. Different components on the phasor plot followed a linear relationship, thus, the ratio of the linear combination could be used to determine the fraction of each component. The lifetime of free and lactate dehydrogenase-bound NADH was about 0.37 ns and 3.4 ns, respectively [176]. Free NADH was linked to more glycolysis and a more proliferative state, while bound NADH was correlated with more oxidative phosphorylation and a more differentiated state [177]. The lifetime of lipid was 7.89 ns associated with long lifetime species (LLS) (**Fig. 3.3B**), the presence of which indicated oxidative stress [178]. The fraction of each component was calculated as **Fig. 3.3B** suggested, F1/F2 was the free/bound NADH ratio, and F3 was the ratio of LLS. Based on the above mechanism, we evaluated the metabolic state of RtOgs quantitatively by calculating the free/bound NADH ratio and LLS ratio in representative image cross-sections. Qualitatively, the metabolic differences were visualized by applying a pseudo color gradient to the phasor plot (**Fig. 3.3C**).

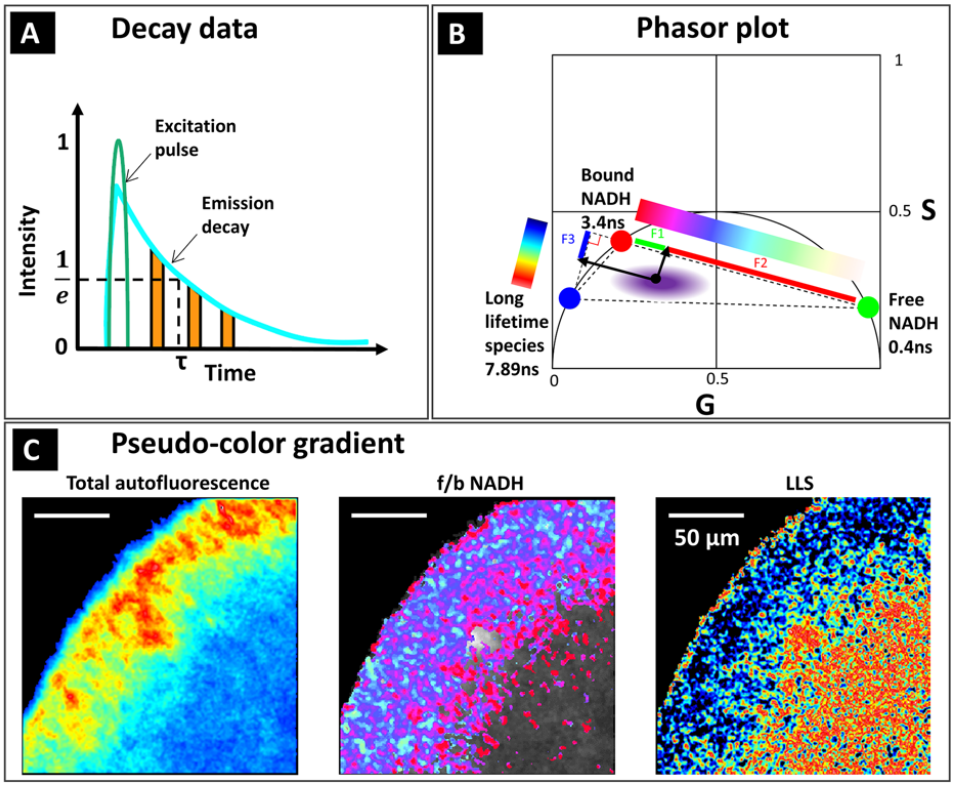

Figure 3.3: Fluorescence lifetime imaging and analysis using the phasor approach.

(A) Fluorescence lifetime was acquired by quantifying emitted fluorescent photon over time after an excitation pulse was supplied to obtain an emission decay curve; (B) Phasor plot produced a 2-dimensional space for intrinsic fluorophores with different lifetimes corresponding with different types of metabolism (oxidative phosphorylation favors bound NADH and glycolysis favors free NADH) and different amounts of oxidative stress (long lifetime species). The free/bound NADH ratio and long LLS ratio were obtained by calculating projecting the 3-dimensional photon count histogram onto the Bound-Free axis and LLS axis respectively; (C) A representative images of RtOg analyzed by the phasor approach. The autofluorescence images encapsulated all total fluorescence, while the f/b NADH and LLS are pseudocolor images based on the phasor analysis of quantized fluorescent emission. f/b NADH was free to bound NADH ratio. LLS was long lifetime species.

Images were taken by a Zeiss LSM 780 microscope using a Plan-Apochromat 20x/0.8 M27 objective (Carl Zeiss, Jena, Germany). The excitation wavelength was 740 nm,

produced by Mai Tai multi-photon laser source (Spectra-Physics Mai Tai, Mountain View, CA). Imaging settings used were as follow: 256 x 256 frame size, 1.66 μm pixel size, 25.21 μs pixel dwell time and 8-bit pixel depth. Emission laser passed through an MBS 690+ and an SBS SP 610 filters and the lifetime data was collected by the photomultiplier tube (H7422p-40, Hamamatsu, Japan) and a320 FastFLIM FLIMbox (ISS, Champaign, IL). Before imaging, the system was calibrated on frequency factor and lifetime by coumarin 6 solution with the known lifetime of 2.5 ns. FLIM data were collected after 100 counts in the brightest pixel of the image were acquired. During imaging, fresh medium flowed into the bioreactor continuously, while RtOgs in static groups were moved into Nunc® Lab-Tek® II Chambered Coverglass (Thermo Fisher) for imaging.

3.2.7 Phase contrast imaging

The phase contrast microscopy images were acquired using an Olympus IX71 (Olympus, Tokyo, Japan) and a QICAM FAST1394 CCD camera (Teledyne QImaging, Surrey, BC, Canada) under two magnifications by UPlanFL N 4x/0.13 PhL and UPlanFI 10x/0.30 PhL objectives.

3.2.8 Green fluorescent protein imaging

Green fluorescent protein images were acquired using a Zeiss LSM 780 microscope using Plan-Apochromat 20x/0.8 M27 objective (Carl Zeiss, Jena, Germany). The excitation wavelength was 488nm with a pixel dwell time of 1.58 μs. We used the frame size of 512 x 512 , and each pixel is 0.42 μm.

3.2.9 Quantitative polymerase chain reaction analysis

The primers for qPCR test are listed in Appendix (Qiagen, Germantown, MD, USA). We used 12 retinal progenitor and photoreceptor genes and 1 housekeeping gene to identify and quantify the gene expression profile in retinal organoids. Human adult retinal tissue was used as a positive control (n = 3). For CRX-GFP hESCs derived RtOgs, each sample was analyzed on days 122 to 124 of differentiation (n = 3 for both static and chip groups); for CSC14 hESCs differentiated RtOgs, each sample was analyzed on day 105 (n = 2 for both static and chip groups). Each sample consisted of 4 RtOgs. Trizol reagent (Qiagen), DNase I digestion (Invitrogen, TURBO, Waltham, MA, USA), and phenol-chloroform extraction (Fisher) were used to isolate RNA, and an RT^2 cDNA synthesis kit (Qiagen) was used to synthesize cDNA. RT^2 SYBR Green with ROX qPCR master mix (Qiagen) was used for amplification, which was performed under the following conditions: 95°C (15 minutes), 40 cycles at 95°C (15 seconds each), 55°C (30 seconds each) and 72°C (30 seconds each). The annealing temperature was 60°C. The double delta cycle threshold (Ct) method was used to calculate the fold expression, and day 0 undifferentiated hESC (line CSC14) was used as a control. For analysis and heatmap generation, non-detected amplification in the control tissue and organoids were assigned cycle threshold values of 40. Heat maps were generated using Graphpad Prism software (Graphpad Software LLC, La Jolla, CA, USA), the heat map has the value of $\log_2$(Fold Expression).

3.2.10 Single cell dissociation

Eight to twelve RtOgs on day 72 and 159 (chip vs. static, four experimental groups in total) were dissociated using papain-based enzymatic digestion by Worthington papain dissociation system (Worthington, Lakewood, NJ, USA), followed the standard dissociation

protocol provided by Worthington. Briefly, the papain vial was dissolved in 5 mL of EBSS buffer in 37°C water bath for 10 minutes to yield a solution at 20 units of papain per ml in 1 mM L-cysteine with 0.5 mM EDTA. After adding 250 µl DNase (2000 units/ml deoxyribonuclease in EBSS) into the papain solution. The RtOgs were added in the papain solution and incubated at 37°C incubator on a rocker platform for 1 hour. Post incubation, the tissue was further triturated using 18G needle and syringe. The dissociated tissue mixture was centrifuged at 300*g* for 5 minutes at room temperature. After removing the supernatant, the cells were resuspended in the albumin-inhibitor solution with 2.7 ml EBSS, 150 µl DNase and 300 µl ovomucoid solution (10 mg/ml Egg White/BSA in EBSS). The single-cell solution was then carefully layered on top of 5 ml albumin-inhibitor solution and centrifuged at 70*g* for 6 minutes at room temperature. The supernatant of dead cells was discarded, and the pelleted cells were immediately resuspended in 1% BSA/PBS solution. The cell viability was tested by 0.4% trypan blue using a hemocytometer (>90%) and the concentration was adjusted to ~870 live cells/ul. The samples were sent for scRNA-seq library preparation within 5 minutes.

3.2.11 Single-cell RNA-seq library preparation

Sequencing libraries were prepared using the protocol from 10X Genomics Chromium Single Cell 3' Reagent Kit v3.1 (10X Genomics, Pleasanton CA). Briefly, the 10X workflow was followed using 10,000 cells as the capture target. The resulting Gel-in-Emulsions (GEMs) were transferred to PCR tubes and incubated in a Bio-Rad C1000 Thermocycler (Bio-Rad Laboratories, Hercules, CA) for the reverse transcription protocol.

The GEMs were cleaned up using Dynabeads MyOne SILANE (Life Technologies, Carlsbad CA) and then amplified using 11 cycles according the 10X workflow. The cDNA was cleaned using 0.6X SPRIselect (Beckman Coulter, Indianapolis, IN) size selection and then quality control assays using Qubit DNA HS assay (Life Technologies, Carlsbad CA) and Agilent 2100 Bioanalyzer DNA HS (Agilent, Santa Clara, CA) were performed. The endogenous cDNA fraction was then processed according to the 10X workflow for library construction. The cDNA was fragmented, end repaired and then A-tailed. After a SPRIselect cleanup the adapters were ligated on the cDNA. Sample indexes were added by PCR and a double-sided size selection using SPRIselect was performed. The libraries were assayed for quality using Qubit DNA HS assay, Agilent 2100 Bioanalyzer and quantified by Kapa qPCR Library (Roche, Basel, Switzerland) quantification for Illumina platform. The libraries were sequenced in the Illumina NovaSeq 6000 (Illumina, San Diego, CA) using 28 cycles for read 1, 8 cycles for the index read and 100 cycles for read 2.

3.2.12 Single-cell RNA-seq data analysis

Raw reads were first subjected to quality control QC analysis with FASTQC software and aligned to the reference transcriptome Grch38 using a short-read aligner STAR68 through the 10X pipeline software cellRanger v.3.1.0. Gene level expression for each valid cell was then quantified using UMI (Unique Molecular Identifier) and normalization was performed. Dimension reduction was then used to visualize and explore major features in single cell RNA-seq data. PCA, t-distributed Stochastic Neighbor Embedding (t-NSE) and UMAP was performed using cellRanger followed by unsupervised clustering methods such

as K mean clustering to identify sub populations and cell types in the sample. Loupe browser v.5.0.1 was then used to visualize the further explore marker gene expression.

3.2.13 Immunohistology

RtOgs were fixed with cold 4% paraformaldehyde in 0.1M Na-phosphate buffer for 1 hour, cryoprotected (30% sucrose) and frozen in optimum cutting temperature (OCT) compound (PolarStat Plus, StatLab, McKinney, TX, USA). Organoids were then cryo-sectioned into 10 µm serial sections and stored at –20°C. Histo-VT One (Nacalai) was used for antigen retrieval at 70°C. Primary and secondary antibodies used are listed in Appendix. Organoid sections were incubated in primary antibody dilutions at the concentrations listed overnight at 4°C. The following day, sections were left incubating in primaries at room temperature for an hour before washing. Sections were then incubated at room temperature for at least 30 minutes in fluorescent secondary antibodies. Following 30 minutes of incubation in 4,6-diamidino-2-phenylindole (DAPI) at a concentration of 50 µg/ml, slides were coverslipped using Vectashield Vibrance Antifade Mounting Medium (Vector Labs, Burlingame, CA, USA).

Fluorescent sections were imaged using a Zeiss LSM700 confocal microscope (Zeiss, Oberkochen, Germany). Tiled stacks of 5-8 µm thickness were taken at 20X and 40X magnifications. Images were extracted using the Zen 3.3 Software (Zeiss). Regions of interest for cell counting were outlined in Adobe Photoshop software (San Jose, CA, USA). Cell counting was performed using ImageJ Software (U.S. NIH).

3.2.14 SEM & TEM sample preparation and imaging

Samples were fixed in Karnovsky's fixative (2% Paraformaldehyde/2.5% Glutaraldehyde in 0.2 M sodium cacodylate buffer) and stored at 4°C overnight. The tissue was then washed by 0.1 M cacodylate buffer and post fixed in the solution (1:1 mixture of 0.1 M cacodylate buffer: 0.2 M cacodylate buffered 2% osmium tetroxide) for 2 hours on ice. The tissue was dehydrated in 35%, 50%, 70%, and 95% ETOH for 15 minutes each.

The organoids were cut into halves in 100% ETOH and washed again with 100% ETOH. Starting from this step, half of each organoid was prepared for SEM and the other half was used for TEM. For TEM samples, after two changes of propylene oxide (15 minutes each), the tissue was then infiltrated in a 1:1 mixture of propylene oxide:Epon Araldite resin overnight. The next morning, this mixture was changed out to fresh Epon Araldite for 2 hours. The sample was then placed into flat embedding molds and polymerized at 60°C for 48 hours. The resin blocks were then cut by Leica EM UC7/FC7 cryo-ultramicrotome (Leica, Wetzlar, Germany). The TEM used in this study was JEOL 2100 (JEOL USA Inc, Pleasanton, CA, USA). The montages were processed by the program Etomo (University of Colorado, Boulder).

For SEM samples, the organoids samples were processed by a Leica critical point dryer. The surface of the sample was sputter coated with platinum using a Leica ACE200 sputter coater before imaging. The SEM used in this study was FEI Magellan 400 XHR (FEI Company, Fremont, CA, USA) with an Everhart-Thornley detector (ETD) and a Through-the-Lens detector (TLD).

3.2.15 Statistical analysis

Data in the plot were presented as means with standard deviations. Graphpad Prism software was used for all statistical analyses. In the GFP MFI, immunohistology cell count, free/bound NADH and LLS ratio figures, one-way ANOVA tests were performed. In the qPCR heatmap, two-way ANOVA tests were performed. The significance was determined by a p value less than 0.05.

3.4 Results

3.4.1 Microfluidics design and testing

The bioreactor chip was designed with the distance between chambers matching a 96-well plate to retain microscope compatibility. Preliminary designs in which chambers were located on one side of a 1000 μm wide perfusion channel revealed two problems: 1) heterogeneous media concentration changes between chambers and 2) low mass transfer efficiency (**Fig. 3.4**). Therefore, not all wells in the preliminary design received comparable fresh media exchange. To optimize the design and improve mass transfer rates, three different variables were evaluated with COMSOL simulation: channel width, channel alignment and chamber height.

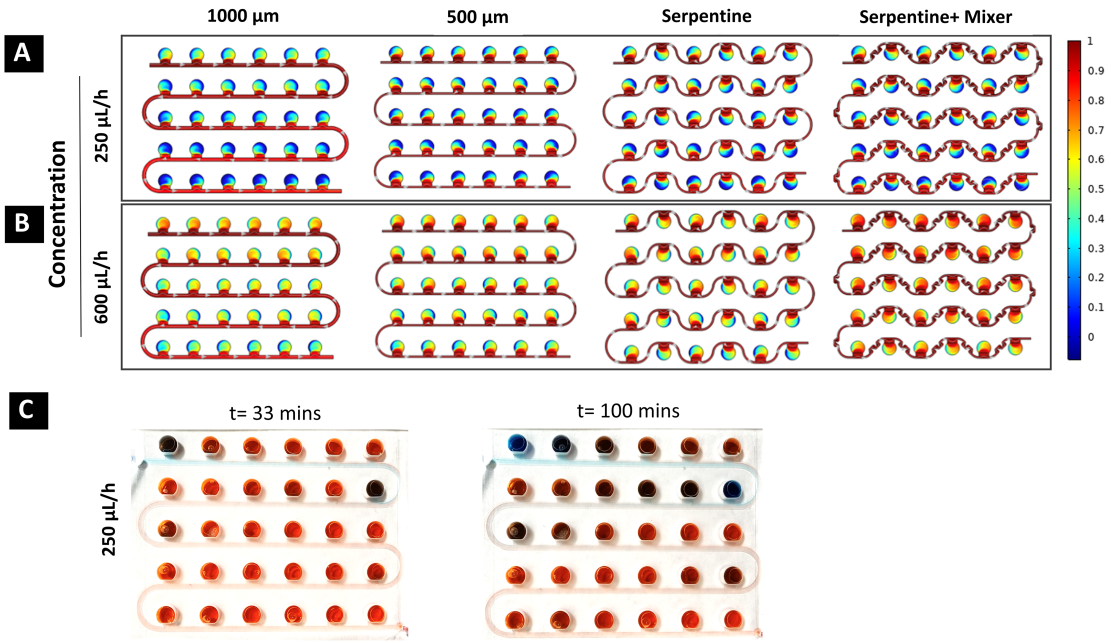

Figure 3.4: COMSOL simulation and dye test of 5*6 arrays bioreactor.

(A) Concentration distribution after 30 minutes of slow flow (250 µL/h); (B) Concentration distribution after 30 minutes of fast flow (600 µL/h); (C) Concentration pattern of the wide channel (1000 µm) design (5*6 array) after 33 minutes and 100 minutes of 250 µL/h flow.

The channel width determined the cross-section area and thus affected the flow velocity (v) as indicated in Equation (1). Holding volume flow rate (Q) constant, the larger the cross-sectional area (A), the slower the flow velocity (v) would be.

$$Q = Av \qquad (1)$$

According to the definition of Péclet number (Pe_L, the ratio of advective transport rate to diffusive transport rate, Equation (2)), a larger flow rate would lead to a higher advective transport rate, accelerating mass transport.

$$Pe_L = \frac{Lv}{D} \qquad (2)$$

where L is the characteristic length, v the local flow velocity, and D the mass diffusion coefficient. Therefore, narrowing the channel width would facilitate an increase in flow velocity. Based on the simulation results, under both flow rates, the narrow channel (500 μm) designs showed faster mass transfer (**Fig. 3.5A-B**) and therefore, a theoretically faster delivery of media to each culture chamber.

Incompressible fluid flow within the microfluidic device, due to its small size, should be laminar with a parabolic velocity profile when flow reaches steady state. As a result, the velocity next to the channel walls should be close to zero. Thus, the designs with all chambers on one side of each channel should show a higher velocity in the fluid close to the channel wall connected to a chamber than the flow velocity on the opposite wall without a connected chamber. **Fig. 3.5A-B** demonstrate that single-sided channel had a concentration gradient from the first chamber to the last chamber in each row and then entire series of chambers. This difference was even more pronounced in a larger series of 5 x 6 chambers (**Fig. 3.4**). To minimize this effect, a serpentine channel was designed to promote comparable media diffusion from both sides of the channel. To further improve concentration distribution, a mixer unit was added between each chamber [179]. Simulation demonstrated that narrow channels with or without mixer showed comparable qualitative performance as indicated with the color map representation of the concentration variations between the first and last culture chambers in each row and those between rows.

The third variable evaluated with simulation was the chamber height. By tracking the point concentration on the same top corner of each chamber, the 3D COMSOL simulation results showed that doubling the height of the chamber to 4 mm caused a

dramatic change (4~10 folds difference) in mass transport efficiency (**Fig. 3.5D**). To maximize the transport efficiency, we chose 2 mm as our final chamber height for bioreactor fabrication. **Fig. 3.5E** shows the 3D concentration patterns in four different bioreactor designs.

To confirm simulation results and examine the functionalities of the four designs, a dye test was performed to confirm the optimum design for culturing RtOgs. A 3 x 3 chamber array was fabricated for each channel design with a 2 mm tall culture chamber. Blue dye was used to fill each channel followed by 30 and 48 minutes of 600 μL/h flow of yellow dye (**Fig. 3.5F**). The grayscale photogrammetry from pictures taken on each chamber were quantified (**Fig. 3.5G**). The serpentine channel with mixer design showed the smallest standard deviation, indicating that this design had the most uniform concentration among the four. The serpentine channel without mixer exhibited the next best performance based on variability after 48 minutes of flow. The simple serpentine channel without an integrated mixer showed higher fabrication success with 3D printing and lower probability of trapped air bubbles in the microfluidic channels than the serpentine channels with mixer.

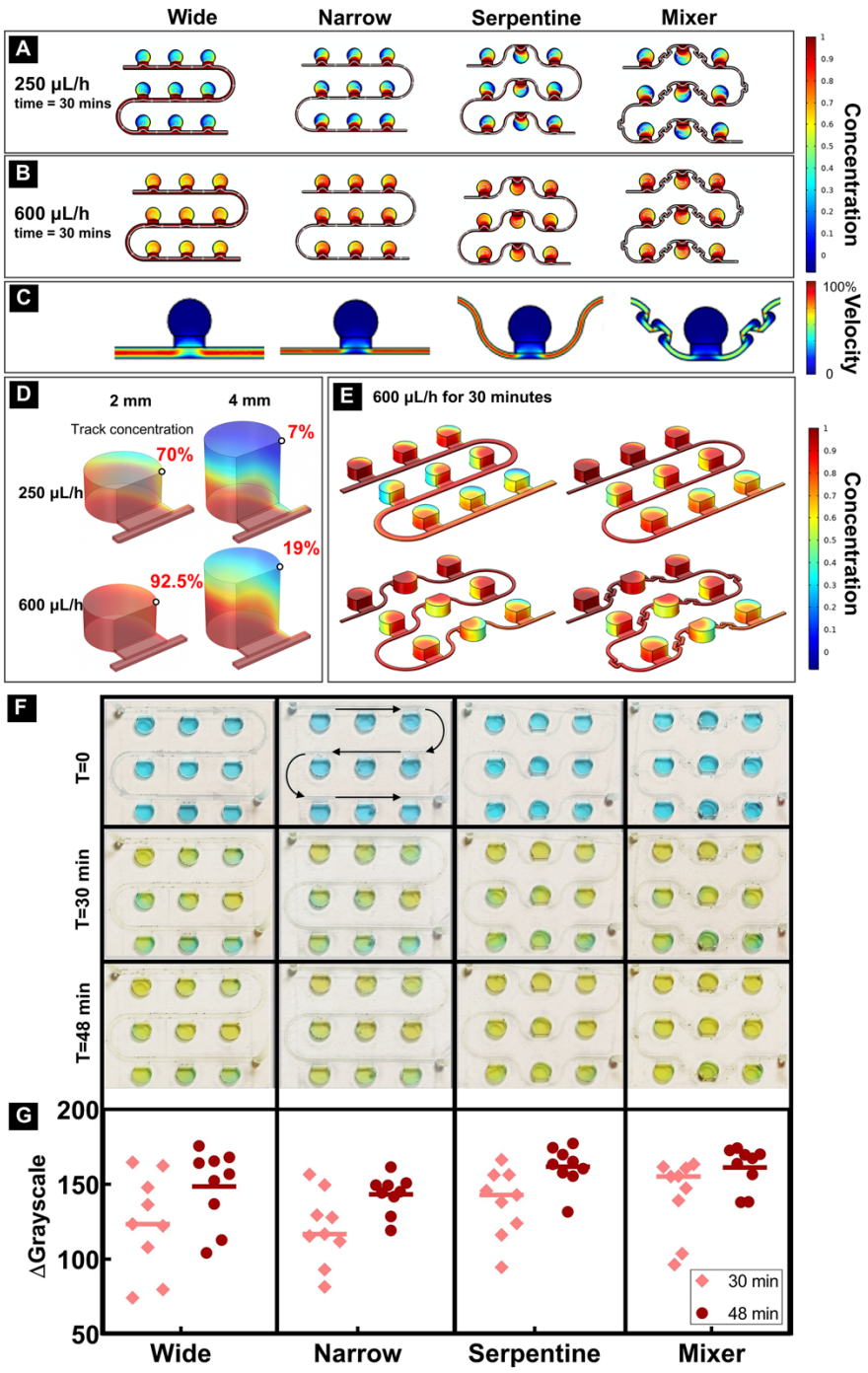

Figure 3.5 COMSOL simulation and dye test of 4 different channel designs.

(A) Concentration distribution after 30 minutes of slow flow (250 µL/h); (B) Concentration distribution after 30 minutes of fast flow (600 µL/h); (C) Velocity distribution – zero velocity in all chambers demonstrated shear stress-free culture environment. A single culture chamber and adjacent flow channels is shown because focal flow velocity was

identical for every culture chamber and interconnecting microfluidic channels in the linear series; (D) Mass transfer efficiency comparison between different height chambers under two different flow rates after 30 minutes. Black circles represent the location of concentration determination at 30 minutes; (E) 3D concentration pattern of four different designs. (F) Diffusion pattern of four different designs (flow rate was 600 μL/h); (G) Grayscale change of each well after 30 minutes and 48 minutes.

3.4.2 Retinal organoid culture methods comparison

3.4.2.1 Phase contrast imaging

Representative phase contrast images in **Fig. 3.7A-D** showed the key stages of RtOg differentiation from human embryonic stem cells. The EZSPHERE microwell aggregated stem cells into uniformly sized embryonic bodies which were then plated on Matrigel coated dishes. Eye fields cut from Matrigel were maintained in ultra-low attachment 24-well plate as they assembled into RtOgs. In this study, RtOgs were put on the bioreactor on days 41, 87 and 128 of differentiation, respectively.

At an early differentiation stage from day 41 to day 71, RtOgs in both static and bioreactor groups showed a significant size change (**Fig. 3.6A-B**) and developed hollow center and transparent edge. **Fig. 3.6C-D** showed a representative RtOg in both groups on day 88 and day 124 of differentiation, respectively. The transparent and laminar outer surface, which was observed in both groups, indicated the development of photoreceptor layer. In later differentiation stages from day 128 to day 158, the RtOg's edge became more mature and developed outer segment-like structures on their surface (**Fig. 3.6E-F**). Overall,

there was no observable morphological difference between static and bioreactor cultured organoids.

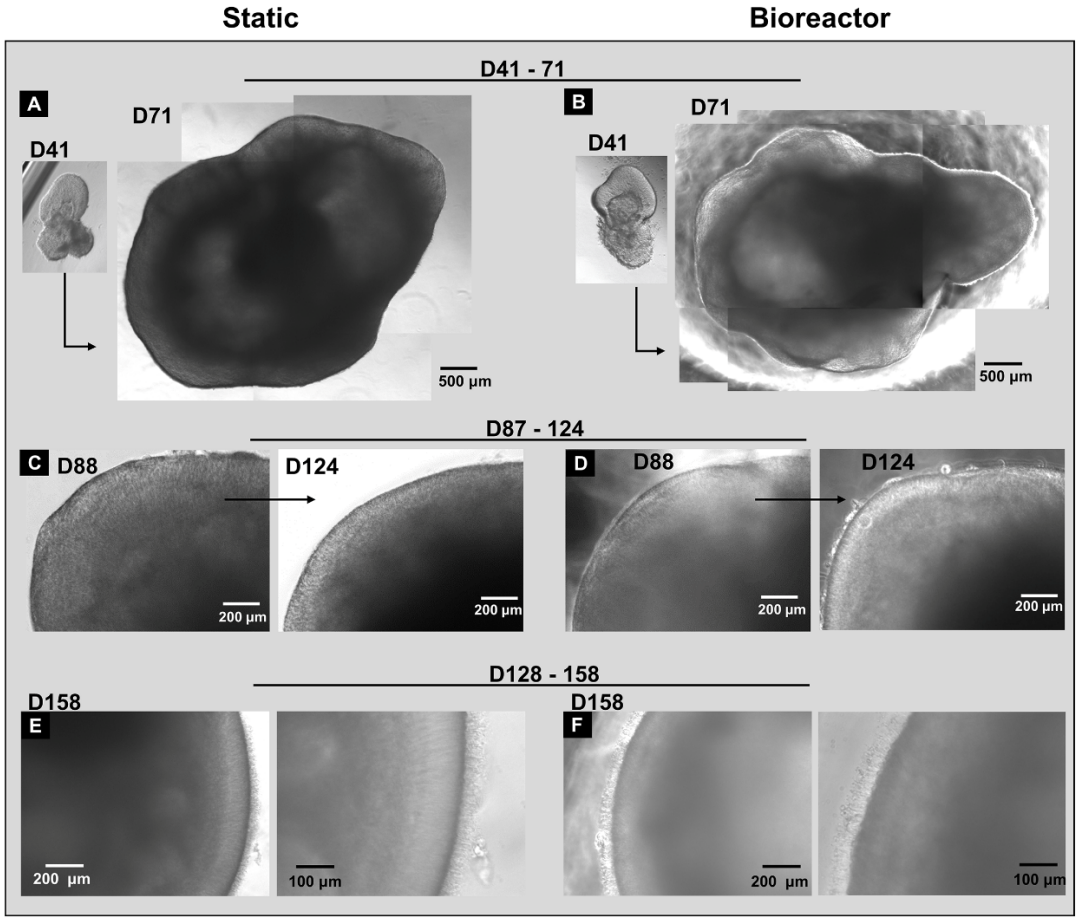

Figure 3.6: Representative phase contrast images of organoid differentiation in bioreactors and static culture during different stages of development.

The same RtOg in static culture (A) and bioreactor culture (B) from day 41 to 71 demonstrating the magnitude of RtOg growth (Day 41 insets share the same 500 µm scale bar as Day 71 larger insets); (C) The same RtOg in static culture from day 88 to 124; (D) The same RtOg in bioreactor culture from day 88 to 124; (E-F) RtOgs on day 158 of differentiation showed outer segment structures in both static and bioreactor groups. (C-F) Higher magnification figures were shown on the right.

3.4.2.2 Fluorescence lifetime imaging

The bioreactor chip platform was continuously supplied with nutrients while the RtOgs in conventional dish culture received nutrient exchanges every 3 days. FLIM was used to measure the metabolic activity in a non-invasive and non-destructive way as described in the method section.

Four imaging modalities were used to visualize the same cross-section in RtOgs. Conventional fluorescence microscopy demonstrated green fluorescent protein (GFP) in photoreceptors and their progenitors in the CRX-GFP organoids (**Fig. 3.7E-H**). Multiphoton infrared stimulation was used to acquire total autofluorescent images showing the total NADH (**Fig. 3.8A-D**), which delineated cellular structures and viability of RtOgs. Multiphoton lifetime imaging revealed metabolic changes in NADH from its free to bound form and their associated free:bound ratio (f/b NADH) (**Fig. 3.8E-H**). Long lifetime species analysis highlighted oxidative stresses in the tissues (**Fig. 3.8I-L**). The above two values were calculated based on the location of the datapoints on the phasor plot (**Fig.3.8M**).

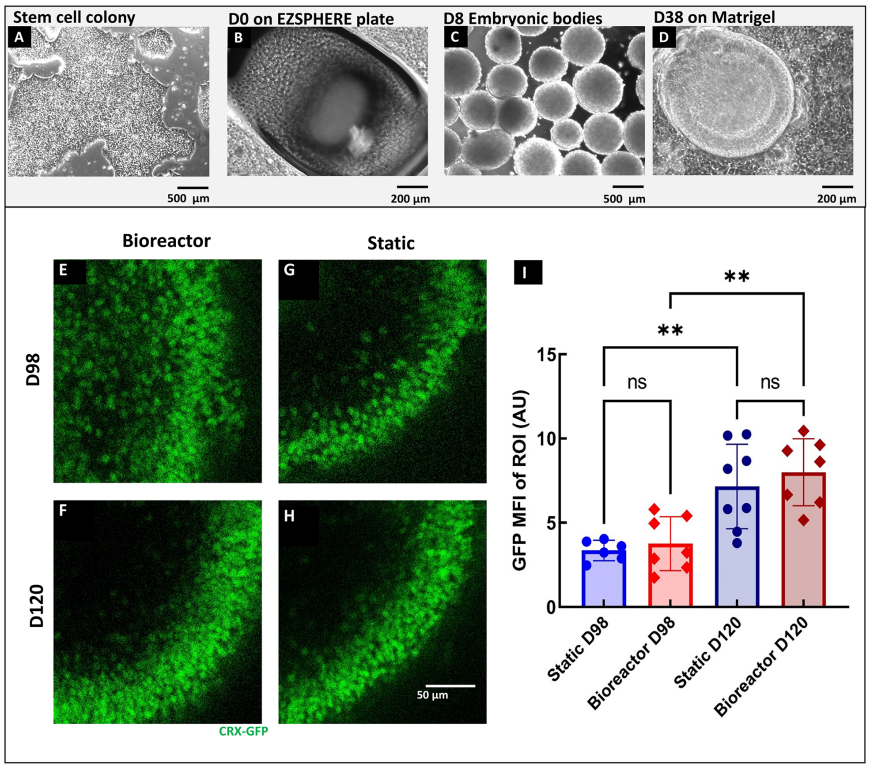

Figure 3.7: Phase contrast and CRX-GFP fluorescence imaging results.

(A) Human embryonic stem cell colony; (B) Day 0 of differentiation, dissociated CRX-GFP stem cells in EZSPHERE microwell plate (well size: 800 µm); (C) Day 8 of differentiation, embryonic bodies ready for seeding on Matrigel; (D) Day 38 differentiation on Matrigel; (E-H) Fluorescence images showed distinct cell nuclear layer corresponding to the CRX-GFP fusion protein localized in nuclei; (I) The mean fluorescence intensity of GFP signals at region of interest (One-way ANOVA test was performed: Static D98, n = 6; Bioreactor D98, n = 7; Static D120 n = 8; Bioreactor D120, n = 7).

RtOgs at different differentiation stages were imaged. For the D41-72 and D128-158 groups, RtOgs were imaged 3 days before the bioreactor and static comparison experiment started (D38 and D125). After approximately one month of culture under two conditions, RtOgs were imaged again at the endpoint (D71 and D158). For the D87-124 group, RtOgs were imaged at two time points (D98 and D120) during the culture period.

RtOg differentiation in both static and bioreactor groups demonstrated a shift from more glycolytic to more oxidative phosphorylated metabolism according to the f/b NADH ratio (**Fig. 3.8N**). On day 38 of differentiation the f/b ratio was the highest (**Fig. 3.8N**). The pseudo color-coded f/b NADH distribution from day 98 to day 120 of differentiation visualized the developmental trend from more glycolytic (yellow-green) to more oxidative phosphorylation (red) (**Fig. 3.8E-H**). A higher total fluorescence NADH metabolic signature was present in bioreactor cultured organoids (Comparing **Fig. 3.8G** and **3.8H**). When comparing the f/b ratio of bioreactor and static culture RtOgs, no significant difference was identified in the f/b NADH ratio on day 71, 120 and 158 (**Fig. 3.8N**).

LLS is a marker for oxidative stress and RtOgs in both groups showed a significant increase of LLS ratio over time (**Fig. 3.8O**). RtOgs on the bioreactor experienced significantly lower LLS signatures on FLIM imaging than RtOgs in static culture at all imaged timepoints (**Fig. 3.8O**). False color LLS images showed a distinct color difference between two groups (**Fig. 3.8K-L**). **Fig. 3.8L** highlights that the innermost layer (where progenitor cells, ganglion cells and Müller glia are located) of the static cultured organoid experienced a higher LLS signal (more red) than the bioreactor cultured RtOgs. The outer layer (where photoreceptors are located) of static cultured RtOgs experienced lower LLS signal (more blue) than bioreactor cultured RtOgs. The time-dependent metabolic shifts and the metabolic difference between two groups were visualized on G-S phasor plot, which highlights the metabolic fingerprint of RtOgs before and after culture in static or bioreactor conditions. The G-S plot demonstrates differential clustering of RtOgs cultured under static or bioreactors conditions at 3 stages of differentiation (**Fig. 3.8M**).

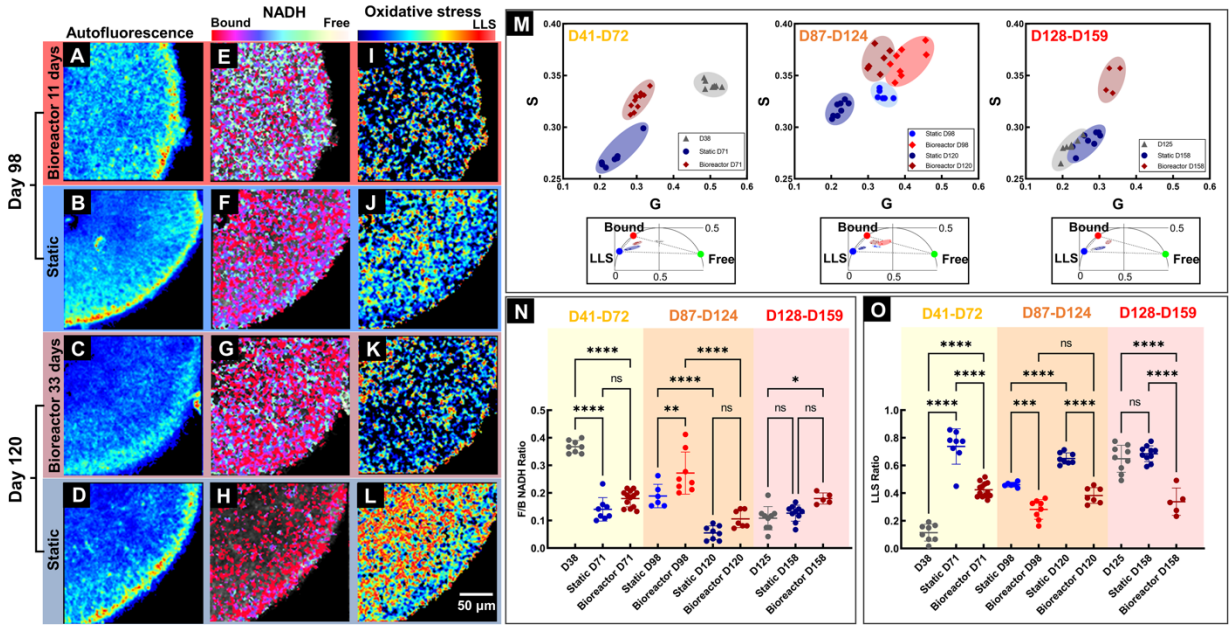

Figure 3.8: Qualitative and quantitative comparison of RtOgs in two culture methods.

(A-D) Total NADH autofluorescence images demonstrated the cellular structures within RtOg cross sections; Pseudo color-coded free/bound NADH distribution (E-H) and LLS distribution (I-L) images were generated based on two photon lifetime within the 2-dimensional phasor space; (M) Scatter plots of and the clustering of different groups of RtOgs on the FLIM phasor diagram; (N) Plot of free/bound NADH ratio to evaluate metabolism (higher f/b value represented glycolysis, and lower f/b indicated greater oxidative phosphorylation.) Metabolism is not significantly different between static and bioreactor RtOgs after 1 month in culture for RtOgs of different ages; (O) Plot of LLS ratio to evaluate oxidative stress. LLS is significantly different between static and bioreactor maintained RtOgs of different ages after 1 month in culture. The values of f/b NADH ratio and LLS ratio reflect the average lifetimes of the organoids cross-section imaging frame. (One-way ANOVA test was performed: D38, n = 8; Static D71, n = 8; Bioreactor D71, n = 13; Static D98, n = 6; Bioreactor D98, n = 8; Static D120 n = 8; Bioreactor D120, n = 7; D125, n = 9; Static D158, n = 10; Bioreactor D158, n = 4; The RtOgs placed into the bioreactor D41-72 were imaged on D38 at the outset of the experiment. The RtOgs placed into the bioreactor D128-159 were imaged on D125 at the outset of the experiment.)

3.4.2.3 *Gene expression profile by single-cell RNA sequencing and qPCR*

We focused on the gene expression profile of RtOgs at several stages of differentiation and compared their cellular profiles maintained in bioreactors and static culture condition. We used scRNA seq to study static- and bioreactor-cultured RtOgs on day 72 and day 159 of differentiation. The genes to distinguish and identify specific cell populations were previously described[180, 181] (**Fig. 3.9A-D**). We also performed qPCR analysis for two different stem cell lines – CRX-GFP (day 124) and CSC-14 (day 105) (**Fig. 3.9F-G**).

Single-cell RNA seq provided a comprehensive overview of cell types within RtOgs. RtOgs that had been maintained in either static culture or bioreactor culture for approximately 1 month were studied at two different time points: D72 and D159. For both static and bioreactor cultured RtOgs, the three predominant cell types on day 72 were retinal progenitor cells (Prog), retinal ganglion cells (RGC) and photoreceptor progenitor cells (PR Prog). Many cells were also in the transition phase 1 (T1) as identified by ATO7 (a marker cells differentiating from retinal progenitor cells to other cells types)[180, 181](**Fig. 3.9A, C**). The population difference of each cell type between static and bioreactor group on day 72 was very small (**Fig. 3.9E**).

Within mature RtOgs after 1 month of static or bioreactor culture on day 158, more advanced cell types emerged and formed more distinct clusters on the scRNA seq UMAP (**Fig. 3.9B, D**). The percentage of RGC decreased, while the proportion of bipolar cells (BC) and Müller glia (MG) increased. PR progenitor cells further differentiated into rods and cones. Compared to static culture RtOgs, those in the bioreactor group contained a higher percentage of retinal progenitor cells. The bioreactor group showed a similar population of

rods and cones, while static group RtOgs contained more rods. Both groups have differentiated cell types that corresponded to cell types found *in vivo* mature human retina. Analysis using qPCR included a short list of retinal genes (detailed information in Appendix). RtOgs derived from CRX-GFP hESCs expressed retinal progenitor genes (CHX10, NRL and RAX) that were comparable to those of human adult retina in both static and bioreactor groups (**Fig. 3.9F**). Both groups also expressed rod and cone genes including RCVRN, ARR3, SAG, PRPH2, GNAT and GNAT2. However, both static and bioreactor cultured RtOgs showed low mature photoreceptor gene expression. Gene expression levels by qPCR were not significantly difference between the static and the bioreactor groups (two-way ANOVA test, $p>0.05$). Similar results were obtained from the CSC-14 hESCs derived RtOgs at 105 days of differentiation (**Fig. 3.9G**); there was no significant gene expression difference between static and bioreactor culture conditions (two-way ANOVA test, $p>0.05$).

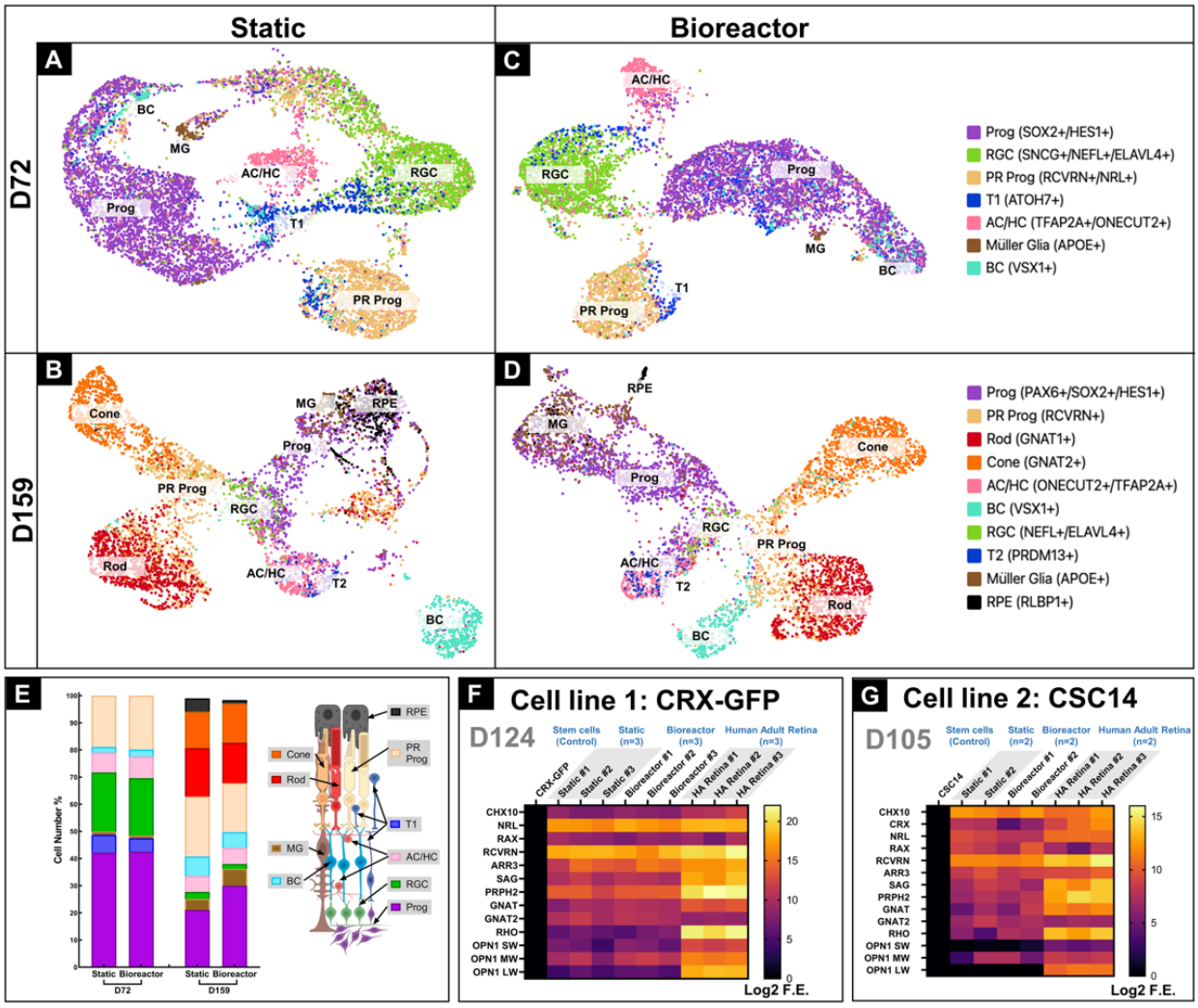

Figure 3.9: Gene profiles of RtOgs at different ages.

Single-cell RNA seq generated UMAP identified cell types of RtOgs cultured under static on day 72 (A) and day 159 (B),under bioreactor culture on day 72 (C) and day 159 (D); (E) Cell number quantification: Cell number percentage of different type of cells, organized by the order of photoreceptor layers and the schematic image was shown on the right side; (F) qPCR gene analysis of CRX-GFP hESCs (negative control) generated RtOgs on day 124 of differentiation; (G) qPCR gene analysis of CSC-14 hESCs (negative control) generated RtOgs on day 105 of differentiation; Log2 F.E – Log_2 (Fold Expression); Cell identities in (A-E): Prog – retinal progenitor cell; RGC – retinal ganglion cell; PR prog – photoreceptor

progenitor cell; T1 – transition phase 1; AC/HC – amacrine cells and horizontal cells; BC – bipolar cells; T2 – transition phase 2; RPE – retinal pigment epithelium cell.

3.4.2.4 Immunohistology and electron microscopy

RtOgs maintained in both conventional static culture or the bioreactor for approximately 1 month were fixed on day 72 and 159 of differentiation. Cryostat sectioning was performed to acquire immunohistology images to visualize cell types and structures. On day 72 of differentiation, RtOgs in both groups demonstrated layered cellular structures (**Fig. 3.10**). The apical aspect was composed of photoreceptor progenitor cells, marked by orthodenticle homeobox 2 (OTX2), and retinal progenitor cells, which were immunoreactive for visual system homeobox 2 (CHX10/VSX2) (**Fig. 3.10A, C**). The basal aspect contained amacrine cells which were immunoreactive for calretinin (CAL2) (**Fig. 3.10A, C**). There were also some retinal ganglion cells marked by brain-specific homeobox/POU domain protein 3A (BRN3A, also known as POU4F1) (**Fig. 3.10B, D**). The expression of synaptophysin (SYP) indicated synaptogenesis (**Fig. 3.10B, D**).

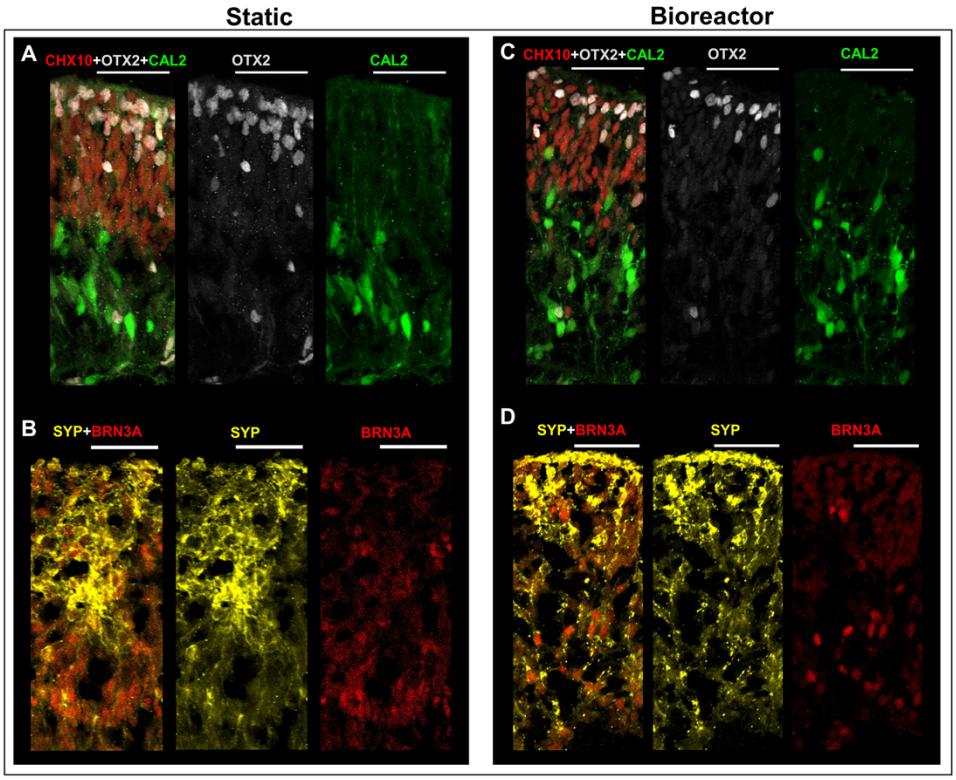

Figure 3.10: Immunohistology images of RtOgs on day 72 of differentiation after 1 month of tissue culture in static or bioreactor conditions.

(A-B) Static cultured RtOgs; (C-D) Bioreactor cultured RtOgs. Antibody marked cells: CHX10 – retinal progenitor cells; OTX2 – photoreceptor progenitor cells; CAL2– amacrine cells; SYP – evidence of synaptogenesis; BRN3A – retinal ganglion cells. (scale bar: 50 μm)

On day 159 of differentiation, RtOgs in both groups (**Fig. 3.11**) demonstrated a distinct and compact photoreceptor outer nuclear layer (ONL), marked by the immunoreactivity for neural retina-specific leucine zipper protein (NRL) (**Fig. 3.11A, D**) and OTX2 (**Fig. 3.11C, F**). When comparing **Fig. 3.11A** and **Fig. 3.11D**, the bioreactor group had a thicker ONL. However, this difference is not significant, as shown in the NRL+ cell counting result in **Fig. 3.11H**. Photoreceptor outer segment structures were shown on the apical aspect, marked by rhodopsin (RHO). The basal aspects were composed of retinal

progenitor cells (CHX10) and amacrine cells (CAL2) (**Fig. 3.11C, F**). Rod bipolar cells immunoreactive for protein kinase (PKC)-α formed the inner nuclear layer (INL) (**Fig. 3.11B, E**). The expression of synaptophysin (SYP) indicated synaptogenesis through the inner plexiform layer (IPL) to ONL (**Fig. 3.11B, D**). High-resolution SEM images showed that RtOgs in both static and bioreactor groups differentiated matured photoreceptor cells with inner segment (IS), connecting cilium (CC) and outer segment (OS) (**Fig. 3.11G, I**). More electron microscopic images are shown in **Fig. 3.12**. Cell counting from the immunohistology staining sections showed no significant difference between static and bioreactor groups (**Fig. 3.11H**).

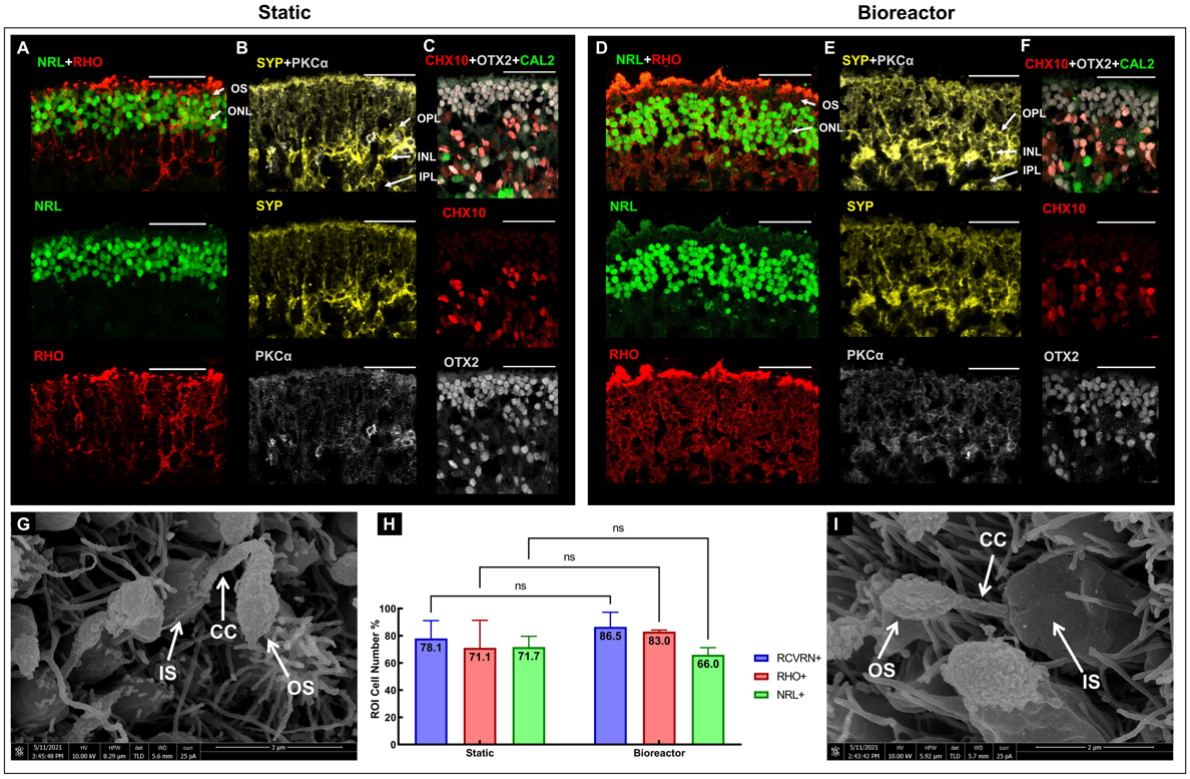

Figure 3.11: Immunohistology and SEM images of RtOgs on day 159 of differentiation.

Immunostaining images of static (A-C) and bioreactor (D-F) cultured RtOgs. SEM images of static (G) and bioreactor (I) cultured RtOgs; (H) Cell counting from selected

immunohistology slides (RCVRN+: n_{static} = 2, $n_{bioreactor}$ = 3; RHO+: n_{static} = 3, $n_{bioreactor}$ = 3; NRL+: n_{static} = 3, $n_{bioreactor}$r = 3). Antibody marked cells: RHO – rod photoreceptors; NRL – photoreceptors; CHX10 – retinal progenitor cells; OTX2 – photoreceptor progenitor cells; CAL2 – amacrine cells; SYP – synaptophysin; PKCα – rod bipolar cells. Arrow markers: OS – outer segment; IS – inner segment; CC – connection cilium. ONL – outer nuclear layer; OPL – outer plexiform layer; INL – inner nuclear layer; IPL – inner plexiform layer. (scale bar: 50 µm)

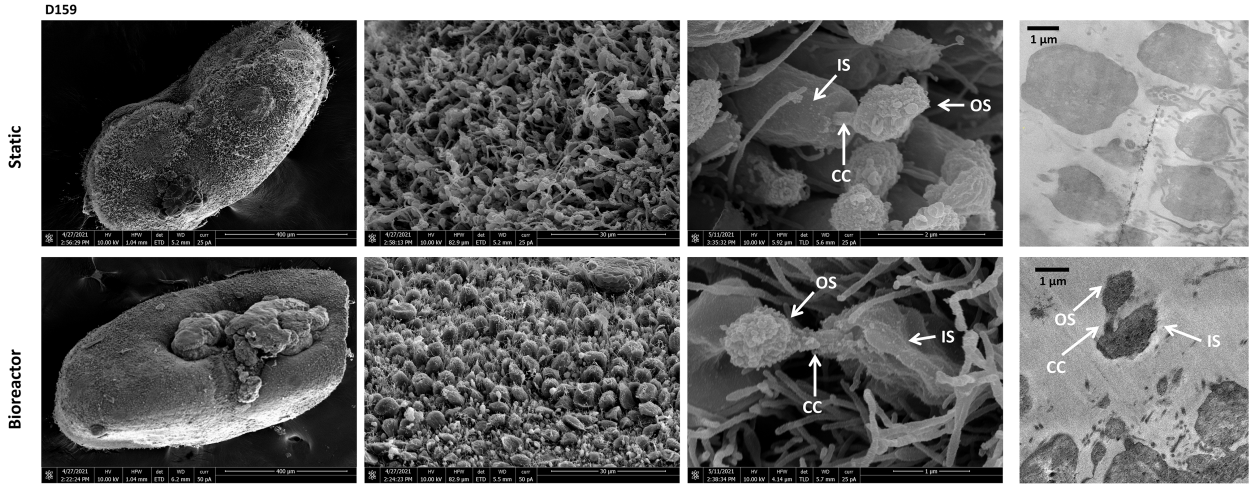

Figure 3.12: SEM and TEM images of RtOgs on day 159 of differentiation showed outer segment-like structures.

Arrow markers: IS – inner segment, OS – outer segment, CC – connecting cilium.

3.5 Discussion

The overall goal of this study was to improve current RtOgs culture techniques by reducing manual labor required for organoid culture and improve the RtOgs reproducibility and quality. Two main differences between *in vivo* retina and conventional *in vitro* RtOg culture were targeted: consistency of nutrition supply and fluid mechanical stability. In the human body, the visual system is the highest energy-consuming system in

the brain [182] and photoreceptor cells are identified as the most metabolically active cells. Retinas in the human body are continuously nourished by the dual blood supply from the choriocapillaris and the retinal vasculature. Additionally, the retina *in vivo* is isolated from mechanical forces, by virtue of the non-compressible fluid contents for the globe and the outermost structural support provided by the sclera. In its natural configuration, the photoreceptors are isolated from dynamic fluid forces, whereas organoids in tissue culture develop photoreceptors surrounded by turbulence in multi-well culture plates. Shear stress can impact the stem cell differentiation phenotypes [183], destroy circulating tumor cells [184], induce cells' metabolite production [185], and cause RtOgs to lose the outer segment like structures [186]. Loss of photoreceptor outer segments is also seen clinically in patients with retinal detachments who develop glaucoma as a consequence of outer segment shedding [187].

Bioreactors for organoid culture to overcome the drawbacks of conventional tissue culture have been described in recent years. Existing challenges for bioreactor designs include minimizing the volume of media used, minimizing shear stresses on tissues and reducing their incompatibility with longitudinal non-invasive imaging. At the macro level, stirred and rotating wall vessel (RWV) [168] platforms have been used for retinal organoid differentiation. The former has been shown to produce retinal organoids with improved laminar stratification and increased yield of photoreceptor cells with outer segment structure, with drawbacks of damage to these fragile structures from sheer stress [186]. The latter has the advantages of improved differentiation, easy use, and high nutrient transfer, and has also been used to culture bladder, lung, intestinal, and vaginal epithelial cell types into three-dimensional cell aggregates [71], [188-191]. However, these larger

systems share the disadvantage of high cost due to the high volume of media required to maintain the organoids [166]. At an intermediate scale is the millifluidic system used to manipulate fluids for organoid maintenance [171]. These bioreactors have been used for development of kidney organoids and long-term maintenance of human midbrain and liver organoids [163, 192, 193]. Millifluidic systems have the advantages of supporting relatively high flow rates, cell-cell interaction, and less frequent media changes and thus less organoid perturbation but has the disadvantage of intermediately high volume and cost, and low throughput. At the microscale, microfluidic devices have the added advantages of lower volume and lower cost compare to millifluidics [171]. Microfluidic devices have been used to culture human intestinal, lung, hepatocyte, and cardiac organoids, [194-196]. For both the milli- and microfluidic devices, shear stress can be minimized by placing organoids in wells or chambers at a set distance from the flow channels. Therefore, we sought to reduce shear stress while creating a perfused environment to house and isolate individual organoids for long term non-invasive imaging.

First, we developed a hybrid bioreactor design that incorporated both micro- and millifluidic components. This design was made possible with the novel fabrication method based on SLA 3D printers to create a mold incorporating micro-, milli- and even macroscopic features (**Fig. 3.2A-D**). 3D printing also enabled rapid prototyping bioreactor designs to iteratively optimize the design. This additive manufacturing offers cost savings and reduced facility requirement compared with traditional microfabrication methods and serves as an attractive alternative to manufacturing bioreactors [197].

We used computer simulation to first demonstrate that each millifluidic culture chamber could be supplied with media from a microfluidic channel. We evaluated flow

velocity inside culture chambers and found no active flow (**Fig. 3.5C**), which satisfied the design goals to minimize turbulence and shear stresses on retinal organoids by eliminating fluidic movement in the culture chamber. We further optimized channel geometry relative to the culture chambers and flow rate of media through the bioreactor. The endpoint for determining success in each design iteration was comparing uniformity of media composition in each culture chamber. We performed both COMSOL simulations *in silico* (**Fig. 3.5**) as well as dye tests *in vitro* (**Fig. 3.5**). *In silico* simulations demonstrated that narrow microfluidic channels (500 μm wide x 200 μm tall) allowed greater mass transfer than wider microfluidic channels (1 mm wide x 200 μm tall). We also observed *in silico* that high flow rate (250 vs 600 μL/hr) also improved mass transfer into culture chambers (**Fig. 3.5B**). *In vitro* dye tests to confirm *in silico* modeling predictably revealed that bioreactor designs with all culture chambers arranged on the same side of the microfluidic channel suffered from diffusion from a single side of the channels laminar flow. This resulted in the first chamber in each row of the microfluidic series to have the highest mass transfer of fresh media, while the last chamber had the lowest (**Fig. 3.4A**). To overcome this limitation, we designed a bioreactor with serpentine microfluidic flow line and culture chambers on alternating sides of the microfluidic flow line. These designs were simulated *in silico* to reveal improved concentration uniformity in each culture chamber compared with straight channel designs. *In vitro* dye testing confirmed that media concentration variability between all wells was improved by the serpentine design (**Fig. 3.5G**). Finally, we introduced mixers in the flow channel to determine if mixing would improve culture chamber concentration uniformity. *In silico* simulation demonstrated improved chamber concentration uniformity over the serpentine channel design (**Fig. 3.5A-B**). *In vitro* dye

testing demonstrated a marginal improvement when the mixer was included than when it was not. A decision based on practical implementation was made to exclude the mixer because of the higher probability of trapping bubbles in the mixer elements as well as the mixer having tapered features that exceeded the resolution of the 3D printers employed.

A second major requirement for our design was to enable imaging of retinal organoids maintained in perfused culture. The bioreactor chip design included glass cover slips to seal the microfluidic circuit. Glass cover slips are thinner than microscope slides and, therefore, suitable for both multiphoton imaging and conventional fluorescence microscopy. Multiphoton imaging relies upon optimally efficient photon capture, and thicker glass slide reduces captured photons below threshold of practical imaging.

A third major requirement for our design is to facilitate RtOgs' long-term maintenance in automated culture. Archberger *et al*. demonstrated a chip platform containing tissue chambers seeded with RPE and fed with media via a porous membrane to mimic vasculature in the retina [198]. This platform emphasized human physiological fidelity and minimized shear stress. However, a limitation was the relatively short 7-day maintenance of the chip platform for organoid culture. After optimizing our bioreactor design, we evaluated its performance in sustaining retinal organoids. The protocol for loading organoids into the bioreactor was determined as described in **Fig. 3.2E-F**. In this body of work, we sought to evaluate the bioreactor's ability to maintain RtOgs for 1 month. We compared organoids in three different differentiation stages (41, 88 and 128 days) that were either placed in the bioreactor for 31 to 37 days or remained in conventional plate culture. Non-invasive functional imaging of metabolism and oxidative stress, sustained development of photoreceptors on the organoids outer layer, and terminal gene and

immunohistology analysis of RtOg tissue were endpoints for comparing culture conditions. Phase contrast microscopy revealed that RtOgs maintained in conventional culture and bioreactors developed a comparable semi-translucent outer layer on day 128 and outer segment-like structures on day 158 of differentiation (**Fig. 3.6C-F**).

We previously used FLIM for live RtOg characterization [78]. The hypothesis in this study was that chip cultured RtOgs would experience less oxidative stress caused by reactive oxygen species (ROS), and the sufficient nutrients supply would benefit RtOgs survival and maturation. On day 38 of differentiation the f/b ratio was the highest (**Fig. 3.8N**) since the RtOgs were just cut from the Matrigel. The value decreased over time, which suggested that RtOgs were more differentiated from a stem cell state (glycolytic) [199, 200]. Bioreactor cultured RtOgs at all timepoints presented similar f/b NADH ratio as those in static culture, indicating similar differentiated state [201] (**Fig. 3.8N**). Furthermore, organoids in the bioreactor demonstrated significant lower LLS levels suggesting that they experienced less oxidative stress than organoids maintained in conventional tissue culture while imaging (**Fig. 3.8O**). A significant increase of LLS ratio was shown over time (**Fig. 3.8O**), which suggested a higher demand for oxygen and a trend to a hypoxic environment as RtOgs became more mature.

One potential problem for long-term bioreactor culture that needs to be solved is tissue adherence. We observed that some RtOgs in both day 124 and 158 groups tended to grow beside the chamber wall after 3 weeks of culture on the bioreactor. While this phenomenon was not observed in day 41 to day 72 group. Thus, adding auxiliary steps to prevent adhesion (e.g., a slow-motion rotating device) should be pursued in future

refinements. Understanding of cell migration, adhesion and mechanics may be further clarified using scRNA seq.

Differences between different stem cell lines were further confirmed by qPCR. For the selected retinal genes, there was no significant difference between RtOgs maintained in conventional culture or the bioreactor in both CRX-GFP and CSC-14 hESC lines (**Fig. 3.9F-G**). However, both static and bioreactor cultured RtOgs on day 105 and 124 showed low mature photoreceptor gene expression, which was expected, as RtOgs typically do not reach full maturity until day 150 of differentiation. Immunohistology and scRNA seq analysis of organoids maintained in the bioreactor or in conventional culture showed cellular and structural similarities. Finally, we observed outer segment-like structures through high resolution SEM imaging in day 159 organoids in both culture conditions (**Figs. 3.12G, I**).

3.6 Conclusion

In this study, we designed and optimized a bioreactor for long term RtOg culture in a low shear stress environment that was also compatible with multimodal imaging. We found that higher flow rate through narrower channel with culture chambers on alternating sides of the perfusion channel enabled optimal and practical concentration uniformity between culture chambers. We subsequently achieved RtOgs culture on a shear stress-free micro-millifluidic bioreactor for 1 month and identified key similarities and differences between RtOgs maintained in either static culture or the bioreactor. We found that: 1) bioreactor cultured RtOgs developed cell types and morphology comparable to

static cultured ones and exhibited similar retinal genes expression levels; 2) the outer surface region of bioreactor cultured RtOgs had comparable free/bound NADH ratio and overall lower long lifetime species (LLS) ratio than static culture RtOgs during imaging. Therefore, the micro-millifluidic bioreactor in this study has demonstrated its potential to sustain RtOgs of comparable quality to those maintained in static culture, while achieving this goal with reduced labor and a sheer stress-free system. Additional investigation is warranted to understand the differences in oxidative stress between RtOgs maintained in static and bioreactor tissue culture.

Chapter 4 : Long-term Functional Characterization of Retinal Organoids Using Two-Photon Fluorescence Lifetime and Hyperspectral Microscopy

4.1 Introduction

With the increase in life expectancy and the resulting aging population, blindness has become a global health problem. Age-related macular degeneration (AMD) is the most common retinal disease among people over 60 years old in the United States [202]. There is a lack of effective drug therapy for most retinal diseases. In recent decades, stem cell-based therapies are showing promises as effective treatments [203]. Human embryonic stem cells (hESCs) or induced pluripotent stem cells (iPSCs) derived retinal organoids (RtOgs) are self-organized tissues that recapitulate *in vivo* retinal development [63-65, 204]. RtOgs exhibit similar structures and cell types as *in vivo* retina, and are used for many applications, including drug screening [53], disease modeling, developmental biological research [55], and transplantation therapies [18, 21, 52, 161].

However, a significant obstacle in RtOg research is the lack of techniques to noninvasively monitor developmental progress and to perform quality control. Currently, most researchers applied immunostaining techniques [205, 206] to identify protein distribution and expression within RtOgs. While immunostaining has high specificity and can highlight the different structures in the tissue with amplified signals [206], the main drawback of this technique is that it requires the tissues to be fixed, which are then no longer available for further studies. Due to the high heterogeneity in the RtOg culturing techniques and the resulting RtOg quality [62], a more reliable approach with consistent outcomes is needed for live organoid characterization.

In recent years, 2-photon microscopy (2PM), which is an imaging technique that functions with fluorescence and pulsing laser [207], has become an alternative for single-photon imaging due to its reduced phototoxicity and photodamaging effects on the imaged tissues [208] while offering higher imaging resolution [209, 210]. 2PM utilizes two photons to simultaneously excite fluorophores in the tissues, reducing the energy per photon by half compared to single-photon microscopy. Lower energy deposited in the specimens extends the limit of imaging duration without adversely affecting the viability of the tissues under examination due to photodamage [211]. Furthermore, 2PM uses red or infrared laser sources, allowing better penetration depth [212] for use in ophthalmological research [213]. Finally, native fluorophores intrinsic within cells can be excited in this wavelength range eliminating the need to introduce extrinsic fluorophores. This label-free live imaging eliminates errors stemming from nonspecific binding of external fluorescent dyes [214].
In 2PM applications, two advanced modalities are used for live organ imaging: fluorescence lifetime imaging microscopy (FLIM) and hyperspectral imaging (HSpec) (**Fig. 4.1**). FLIM is commonly used to observe the metabolic states of live samples [215]. Briefly, an impinging photon excites a molecule to a higher potential state. While returning to its ground state, the molecule emits fluorescence light at an intensity that decays over time. The lifetime of this fluorophore emission depends on its molecular environment regardless of the fluorophore concentration [216]. Intrinsic fluorophores such as auto-fluorescent metabolic coenzymes nicotinamide adenine dinucleotide (NADH) and flavin adenine dinucleotide (FAD) are commonly targeted in FLIM [217]. The spatial distribution of fluorescence is imaged with a charge-coupled device (CCD) camera [218]. Currently, FLIM has been used to observe the intracellular environment of single cells [219] and RtOgs [78]. When FLIM is

integrated with an ophthalmoscope (fluorescence lifetime imaging ophthalmoscope, FLIO), it can be used to help with retinal disease diagnoses [220, 221].

One effective way to analyze FLIM imaging results is the phasor approach [175]. In particular, the distribution map of the fluorescence lifetime of a sample or specimen represents the lifetime signature [178]. NADH exhibits a shorter decay time in its free form in solution (0.4 ns) than when bound to lactate dehydrogenase (3.4 ns) [222]. The ratio of free/bound NADH can be represented on a phasor plot to show their linear relationship to quantify the metabolic state of a specimen (**Fig. 4.1D**) [216]. Free NADH indicates glycolysis and a more proliferative state (stem cell-like), while bound NADH is correlated with more oxidative phosphorylation and a more differentiated state [177]. Hyperspectral imaging (HSpec), on the other hand, collects fluorescence spectral data associated with each pixel composing an image [223]. Each pixel is therefore decomposed to multiple wavelength components and the spectral composition of a pixel is correlated with its chemical composition. HSpec generates higher-resolution three-dimensional datasets than multispectral imaging and thus capable of discerning distinct chemical species (such as retinol and retinoic acid) through overlapping spectra [224] and phasor approach (**Fig. 4.1E**) [78]. The phasor approach to analyzing hyperspectral data facilitates data decomposition by mapping complicated spectra to a 2-dimensional phasor plot by using a pair of Fourier sine and cosine transforms. Each pixel in the fluorescence image is mapped specifically to a location of the phasor plot by way of a determined phase monitor and angular position [225]. HSpec has been applied to imaging human retinal pigment epithelium (RPE) *ex vivo* to identify specific spectral signatures [226]. It has also been used

in vivo to measure oxygen saturation in human retina [227] and to discern potential Alzheimer's disease biomarkers [228].

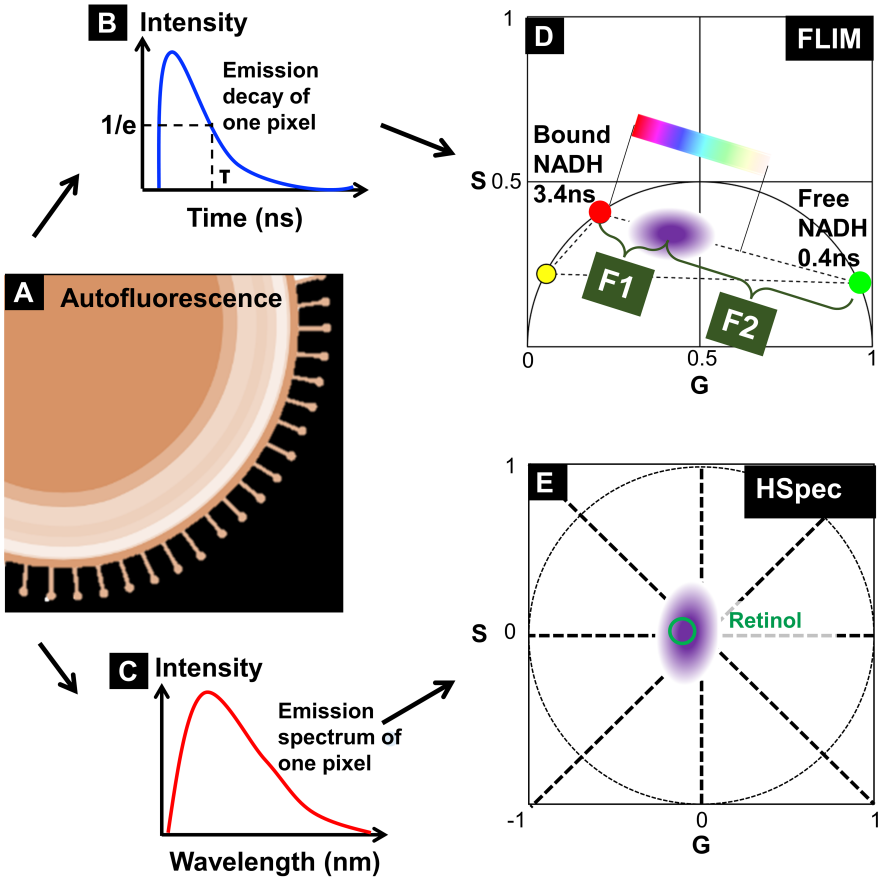

Figure 4.1: FLIM and HSpec techniques used in this study.

(A) Schematic of an autofluorescence intensity map of a live RtOg's cross section generated by 740 nm pulse laser excitation composed of pixels. Each pixel was analyzed to generate an emission intensity decay curve (B) and the spectrum curve (C). The lifetime τ is the time point when the intensity decreased to 1/e of the peak autofluorescence intensity (B). The lifetime (B) and spectrum (C) curve were then transformed mathematically to two a lifetime and hyperspectral phasor plot. (D) Phasor plot of FLIM showed a 2D diagram for intrinsic fluorophores with different lifetimes (bound NADH is indicative of oxidative phosphorylation and free NADH represents glycolysis). On the phasor plot components followed a linear relationship, thus, the fractions of free and bound NADH were F1 and F2, respectively. The free/bound ratio was obtained by calculating F1/F2. (E) Phasor plot of

hyperspectral imaging showed the distribution of the intrinsic retinol fluorophore located within the point cloud representing the hyperspectral phasor analysis.

In this study, we applied 2PM to noninvasively examine the metabolic and structural changes in RtOgs long-term development. RtOgs derived from two stem cell lines were investigated with 2PM. In FLIM imaging we focused on the metabolic signatures indicated by free and bound NADH. In HSpec imaging we primarily investigated retinol, which is one of the retinoids produced in the visual cycle [229]. The accumulation of retinol is a marker of functional photoreceptor cells [78]. We further validated the functional imaging results with endpoint qPCR, single-cell RNA sequencing (sRNA seq), and immunohistology.

4.2 Methods

4.2.1 Stem cell culture and retinal organoid differentiation

The stem cell culture and RtOg initiation procedures were detailed in our previous publication [1], which were based on RtOgs differentiated from two hESC lines (cell line CSC14 with NIH registration no. 0284 and H9 (WA09) CRX-GFP with NIH registration no. 0062 [81]). In the present study, we focused on CSC14-derived RtOgs in 10 GMP-compatible batches to perform long-term functional imaging and qPCR analyses. Subsequently, selected RtOgs were used for sRNA seq and immunohistology analyses. In addition, long-term imaging data from RtOgs differentiated from CRX-GFP hESCs were used in repeatability tests.

4.2.2 Two-photon FLIM and HSpec imaging

A Zeiss LSM 780 microscope (Carl Zeiss, Jena, Germany) equipped with a multi-photon laser source at 740 nm (Spectra-Physics Mai Tai, Mountain View, CA) was used to perform both FLIM and HSpec 2P imaging through a Plan-Apochromat 20x/0.8 M27 objective (Carl Zeiss).

FLIM imaging settings used in this study were the same as in our previous publication [1]. Before imaging, the system was calibrated on frequency factor and lifetime with coumarin 6 solution, which has the known lifetime of 2.5 ns. Briefly, imaging settings used were as follow: 256 x 256 frame size, 1.66 μm pixel size, 25.21 μs pixel dwell time and 8-bit pixel depth. Emission laser was collected by the photomultiplier tube (H7422p-40, Hamamatsu, Japan) and a320 FastFLIM FLIMbox (ISS, Champaign, IL). Fluorescence emission photons were counted. The lifetime information of each pixel was extracted according to the intensity decay curve (**Fig. 4.1B**). Using Fourier transform, the lifetime information of each pixel was mapped to a phasor plot, which contained on the so-called universal circle. Each point on the boundary of the universal circle represents a single exponential lifetime of one type of molecule and the proportion between molecules followed linear relationships. In this study we focused on the lifetime of free (0.4 ns) and lactate bound (3.4 ns) NADH (**Fig. 4.1D**). Additional details for FLIM imaging and data and data analysis using the phasor approach with SimFCS software (Globals Software G-SOFT INC, Champaign IL, USA) have been published previously [1, 175]. The fraction of free and bound NADH was normalized to the orthogonal intersection value on the metabolic NADH trajectory line by mapping the phasor plot center of mass directly to the free-bound NADH axis. As demonstrated on the phasor diagram (**Fig. 4.1D**), F1 is the fraction of free NADH and F2 is the fraction of bound NADH. Free/bound ratio equals to F1/F2. To overlay the

metabolic color map on the structural image of the RtOg, we assigned a color bar along the free and bound NADH line and assigned a color value to each pixel in the image depending upon its location on the phasor plot as shown in Supplementary **Fig. 4.1D**.

Similarly, HSpec imaging settings were detailed in our previous publication [78]. Briefly, the fluorescence emission spectrum of 410 nm to 690 nm was collected with a 32-channel detector. The spectrum information of each pixel (**Fig. 4.1C**) was transformed into the data point on the spectral phasor plot (**Fig. 4.1E**). On the phasor plot different molecules have their unique "fingerprints". By using the HSpec image analytical software (Translational Imaging Center, University of Southern California) [230, 231], we were able to circle out the region that retinol located on the phasor plot and recolor that portion of pixels back on the HSpec image, thus the retinol distribution could be visualized.

4.2.3 Quantitative polymerase chain reaction (qPCR) analysis

The primers for qPCR test are listed in Appendix (Qiagen, Germantown, MD, USA). In total, 14 retinal progenitor and photoreceptor genes and one housekeeping gene used as reference gene were examined for gene expression profile. Human fetal (HFE, age 137 days = 4.6 months) and adult retinal (HA) tissue (Eye bank, UCI-20-153-C-T) were used as positive controls. RtOgs aged from day 51 to 159 were grouped according to similar differentiation stages. Each sample set consisted of 3∼5 RtOgs and there were at least three samples in each group. Trizol reagent (Qiagen), DNase I digestion (Invitrogen, TURBO, Waltham, MA, USA), and phenol-chloroform extraction (Fisher) were used to isolate RNA and an RT2 cDNA synthesis kit (Qiagen) was used to synthesize cDNA. RT2 SYBR Green with ROX qPCR master mix (Qiagen) was used for amplification, which was performed with

the following protocol: 95°C (15 minutes), 40 cycles at 95°C (15 seconds each), 55°C (30 seconds each), and 72°C (30 seconds each). The annealing temperature was 60°C. The double delta cycle threshold (Ct) method was used to calculate the fold expression with day 0 undifferentiated hESC (line CSC14) as the negative control. For analysis and heatmap generation, non-detected amplification in the control tissue and RtOgs were assigned cycle threshold values of 40. Heat maps with values in $\log_2$(Fold Expression) were generated using Graphpad Prism software (Graphpad Software LLC, La Jolla, CA, USA).

4.2.4 Single-cell RNA sequencing

To further compare the change of the cellular type of our RtOgs, we chose two typical time points – Day 57 and day 172 – for single-cell RNA sequencing analysis. RtOgs around D57 are in a multipotent state. This corresponds with the RtOg age when they are used in transplantation studies because their differentiation and proliferation potential allows integration with host tissue. In our previous publications we used RtOgs between 30 to 70 days of differentiation for transplantation in the retinal degenerate rat models and observed vision improvement [18, 21]. The other time point D171 corresponds with fully matured RtOgs when photoreceptor cells with outer segment-like structures are present. A total of 14 RtOgs on Day 57 (D57) and 12 RtOgs on D171 were dissociated using papain-based enzymatic digestion (Worthington papain dissociation NJ, USA). Cell viability was tested with 0.4% trypan blue in a hemocytometer (>90%). The concentration was adjusted to ~870 live cells/µl for day 171 samples and ~822 cells/µl for day 57 ones. The samples were prepared for scRNA-seq library within 5 minutes. The cell dissociation, library

preparation, and data analysis were detailed in [1]. The raw data were uploaded to ArrayExpress and the accession number is E-MTAB-11121.

4.2.5 Immunohistology

RtOgs on D118 and D169 of differentiation were fixed with cold 4% paraformaldehyde in 0.1M Na-phosphate buffer for 1 hour, cryoprotected (30% sucrose), and frozen in optimum cutting temperature (OCT) compound (PolarStat Plus, StatLab, McKinney, TX, USA). They were then cryo-sectioned into 10 μm serial sections and stored at −20°C. The primary and secondary antibodies used are listed in Appendix. The staining procedure was detailed in [1]. Fluorescent sections were imaged with a Zeiss LSM700 confocal microscope (Zeiss, Oberkochen, Germany). ImageJ software (NIH, USA) was used for cell counting.

4.3 Results

4.3.1 Functional imaging revealed RtOgs long-term metabolic and structural development

2P functional imaging was performed on the 10 GMP-compatible batches from CSC-14 hESCs derived RtOgs. **Fig. 4.2A** shows the results of representative RtOgs in long-term culture. The FLIM maps showed the spatial distributions of metabolic activities within a section of the RtOgs, confirming overall cellular viability and revealing a long-term developmental trend. RtOgs before D59 showed a higher f/b NADH ratio (**Fig. 4.2B**) than the more mature ones. The FLIM map at D47 showed a more glycolytic surface with higher proliferative activities and the HSpec retinol distribution spread in the inner layer (**Fig.**

4.2A, first column). As the RtOgs progressed through differentiation, a decrease in f/b NADH ratio was observed between D54 and D115 (**Fig. 4.2B**). This was consistent with the false-color FLIM maps showing a shift to a red-dominated profile indicating a more differentiated state (**Fig. 4.2A**, second to fourth columns). However, it was observed that the total metabolic activities partially shifted back toward glycolysis around D120 as shown in the gradual rise in the f/b NADH ratios, which then settled on a value slightly higher than the minimum (**Fig. 4.2B**). At the fully matured stage (D169), the presence of outer segment-like structure in the photoreceptor layer was observed, and the outer nuclear layer exhibited a glycolytic surface (**Fig. 4.2A**, sixth column). The HSpec autofluorescence image also showed a compact outer nuclear layer and a denser retinol distribution.

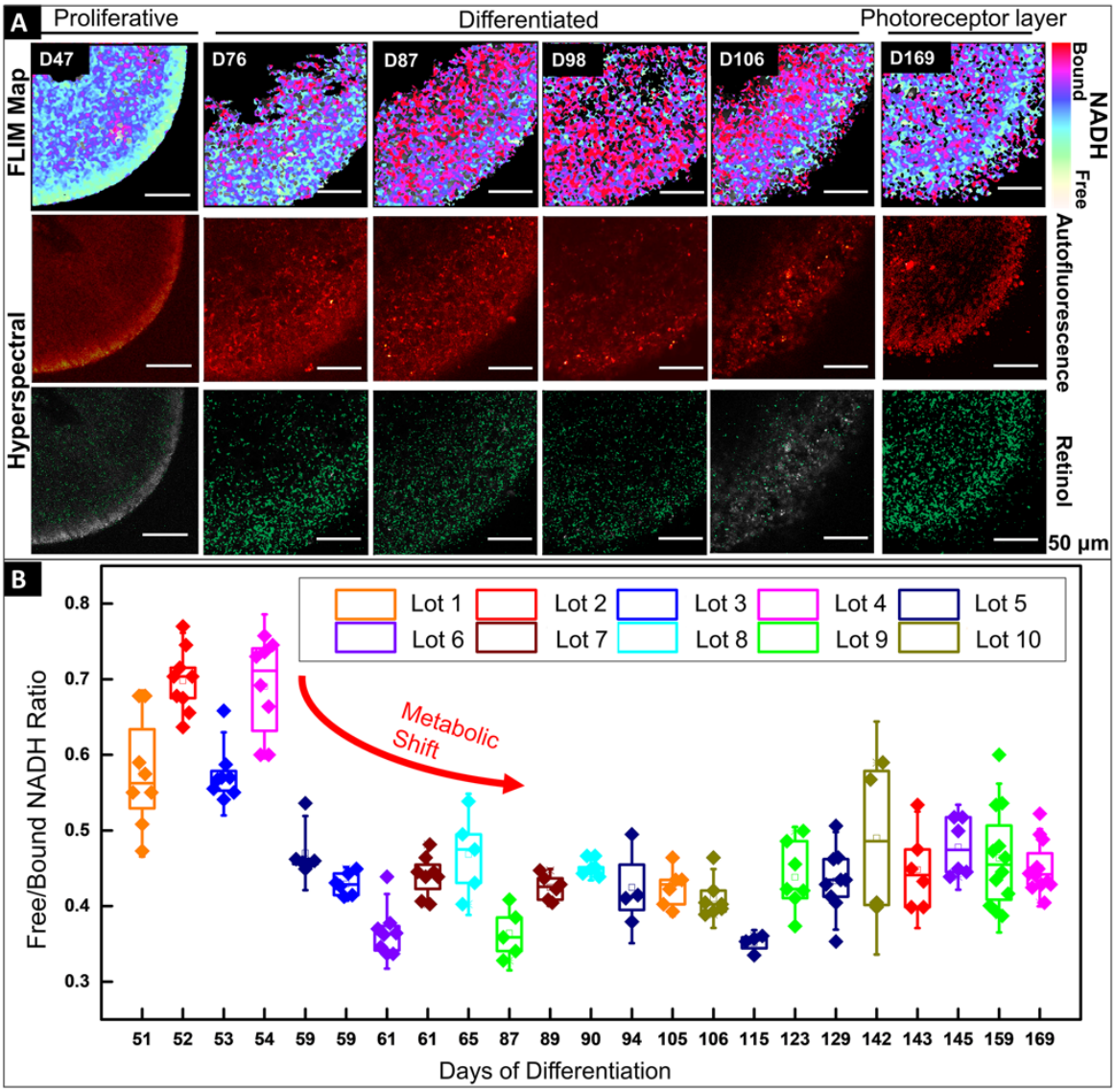

Figure 4.2: Functional imaging results of CSC-14 hESCs derived RtOgs.

(A) FLIM and HSpec images of a typical RtOg. RtOg ages were from D47 to D169 of differentiation. The first row shows the pseudo-color-coded images that indicated free/bound (f/b) NADH ratio distribution. The second row shows the total autofluorescence emission from all intrinsic fluorophores that were excited by a 740 nm laser in HSpec scanning mode. The third row shows the retinol distribution in the imaged cross section and the results were calculated with spectral phasor plots from HSpec images. (B) f/b NADH ratio boxplot that summarized RtOgs from D51 to D169 of differentiation. The data set included 10 GMP-compatible batches of RtOgs. The boxplot indicates the 25th

percentile, median and 75th percentile of the datapoints and the error bar indicates 1.5x standard deviation.

We investigated RtOgs differentiated from a second stem cell line (CRX-GFP hESCs) and performed similar functional imaging. A similar metabolic trend was observed throughout the RtOg development. As shown in **Fig. 4.3A**, the RtOg at a young age (D63) exhibited a larger area of the glycolytic surface in the FLIM map consistent with its proliferative activities than on D176, when only the outermost layer showed elevated glycolytic activities (**Fig. 4.3B-C**), which was the metabolic signature of photoreceptor cells [78]. The HSpec autofluorescence image showed a more distinct layering over time. The retinol also accumulated in the region where photoreceptors were located.

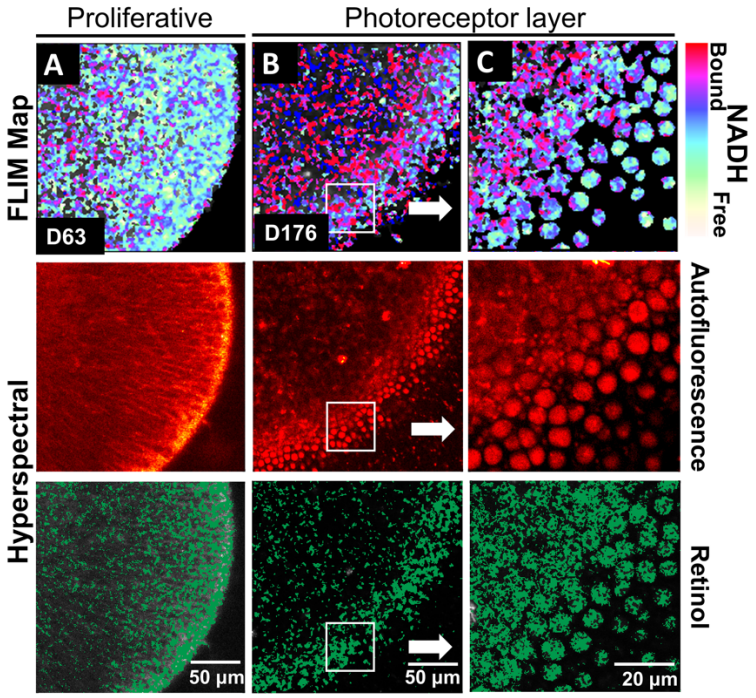

Figure 4.3: Functional imaging results of CRX-GFP hESCs derived RtOgs.

FLIM and HSpec images of a typical RtOg are shown. RtOgs on (A) D63 and (B) D176 of differentiation. (C) The magnified view of the outer surface of the RtOg on D176.

In summary, FLIM demonstrated retinal organoid development with a metabolic transformation from predominantly glycolytic to predominantly oxidative which occurred between 2-3 months of culture.

4.3.2 Molecular analyses validated the developmental changes shown in functional imaging

RtOgs of two different stages (D57 and D171) were analyzed with sRNA-seq and the cell clusters were identified in the UMAP based on previous studies (**Fig. 4.4A-B**) [180, 181]. The young age group on D57 consisted of mainly retinal progenitor cells (51%), retinal ganglion cells (21%), cells in transition phase 1 (12%), and photoreceptor

progenitor cells (7%) (**Table 4.1**). On D171, additional cell types were observed with retinal progenitor cells (24%), bipolar cells (21%), and photoreceptor cells (20%) (**Table 4.2**). Among photoreceptors, 25% were rods and 55% cones (**Table 4.2**).

Retinal progenitor and photoreceptor marker genes were found with qPCR in RtOgs between D51 and D159 (**Fig. 4.4C**). The stem cell group was used as negative control and human retina groups (fetal and adult) as positive control. The data showed that: (1) retinal progenitor genes were expressed in all groups; (2) mature photoreceptor genes were expressed after two months of differentiation consistent with the time point when a shift in f/b NADH ratio in long-term imaging (**Fig. 4.4B**); (3) RtOgs more than 3-month old (D87-D159) exhibited a photoreceptor gene expression level between that of human fetal retina (HFE) and human adult retina (HA); and (4) The RtOgs at 4 months of differentiation showed more OPN1 SW and OPN1 LW (cone opsins) indicating the start of maturation, which was consistent with the f/b NADH ratio settling on a stable value from 4 months and onward (**Fig. 4.4B**).

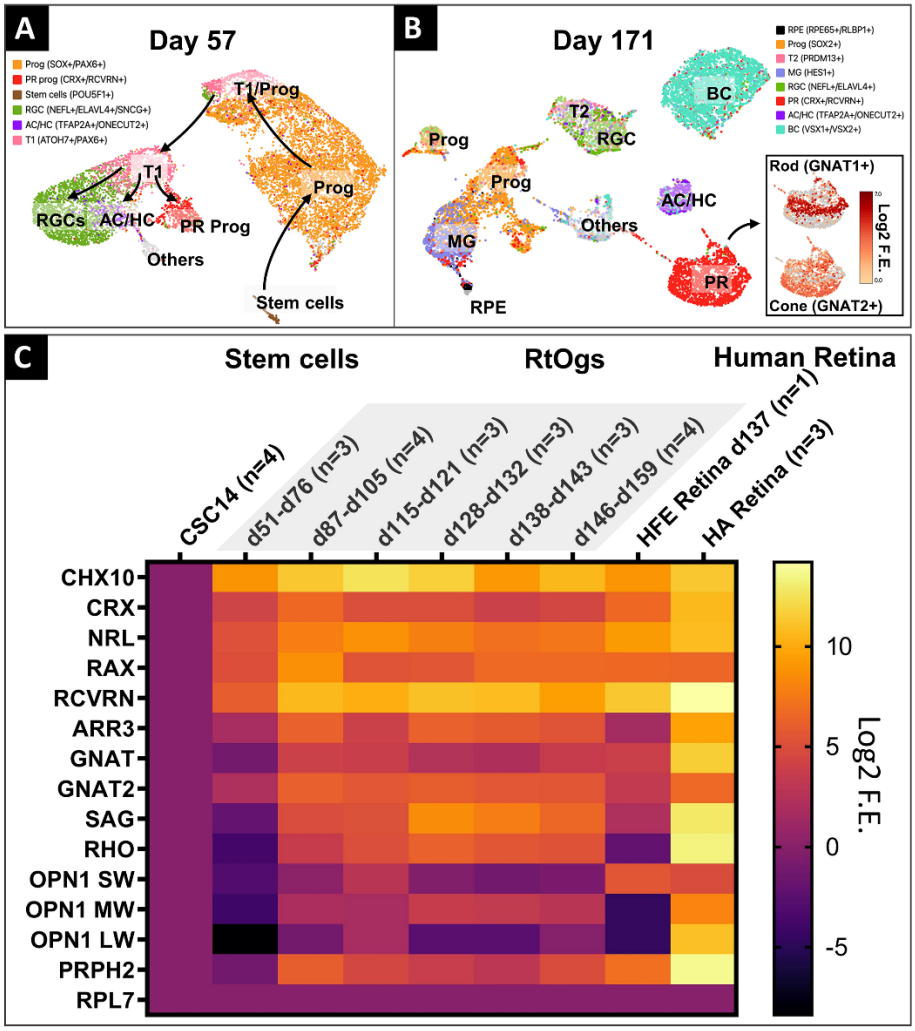

Figure 4.4: Gene profiles of RtOgs at different ages.

(A-B) sRNA-seq UMAP showing the cell types in young (D57) and mature (D171) RtOgs. (C) qPCR heatmaps of RtOgs at various differentiation stages. CSC-14 hESCs derived RtOgs (negative control) were grouped according to similar day ranges. RPL7 was the housekeeping gene used for reference. Human fetal retina (HFE) and adult retina (HA) were used as positive control. Log2 F.E. – Log2 (Fold Expression). Cell legends in (A-B): Prog – retinal progenitor cell; RGC – retinal ganglion cell; PR prog – photoreceptor progenitor cell; T1 – cell in transition phase 1; AC/HC – amacrine cells and horizontal cells; BC – bipolar cells; T2 – cell in transition phase 2; PR – photoreceptor cell; RPE – retinal pigment epithelium cell.

Table 4.1: scRNA seq cell type and percentage – Day 57

Cell type	Cluster gene	Cell #	Cell %
Retinal progenitors	SOX2+, PAX6+	5434	51%
Photoreceptors progenitors	CRX+, RCVRN+	786	7%
Stem cells	POU5F1	157	1%
Retinal ganglion cells	NEFL+, ELAVL4+, SNCG+	2216	21%
Amacrine cells/ Horizontal cells	TFAP2A+, ONECUT2+	179	2%
T1 phase	ATOH7+, PAX6+	1265	12%

Table 4.2: scRNA seq cell type and percentage – Day 171

Cell type	Cluster gene	Cell #	Cell %
Retinal progenitors	SOX2+	2480	24%
RPE	RPE65, RLBP1+	174	2%
Muller glia	HES1+	986	9%
Retinal ganglion cells	NEFL+, ELAVL4+	794	8%
Amacrine cells/ Horizontal cells	TFAP2A+, ONECUT2+	332	3%
Bipolar cells	VSX1+, VSX2+	2212	21%
T2 phase	PRDM13+	358	3%
Photoreceptors	CRX+, RCVRN+	2078	20%
Matured Rods (among Photoreceptors)	GNAT1+	560	25%
Matured Cones (among Photoreceptors)	GNAT2+	1148	55%

4.3.3 2PM versus Immunohistology on photoreceptor imaging

In addition to FLIM and HSpec, 2PM also provided high-resolution brightfield images. **Fig. 4.5A** showed the combination of brightfield and NADH autofluorescence

images of the cross section of a RtOg. The outer segment structures were fully preserved and clearly shown. The 3D representation of the organoid surface as shown in **Fig. 4.5B** was reconstructed from Z-stack images. The 2PM images indicated that NADH autofluorescence was mainly distributed in the outer nuclear region. Immunohistology on the same organoid (**Fig. 4.5F-K**) provided further details on the cell types and laminated structures. However, the outer segment structures were not fully preserved after the sectioning steps necessary for performing immunohistology.

Young RtOgs that preserved proliferative capability and multipotency have expressed more retinal progenitor marker based on our previous studies [18, 21]. The RtOgs fully matured in around 4 months of differentiation. Immunohistology showed that RtOg on D118 developed CRX+ and recoverin+ photoreceptor layer (**Fig. 4.5C-E**). In addition, RtOgs on both D118 and D169 showed distinct inner and outer nuclear layers. The cell counting results from immunohistology slides showed >40% CRX and recoverin+ cells in the outer retinal rim. The percentage of NRL+ cells (rod-specific marker) was lower, indicating a high percentage of cones in the organoids. This result was consistent with the sRNA seq findings that cone photoreceptors were more abundant than rods.

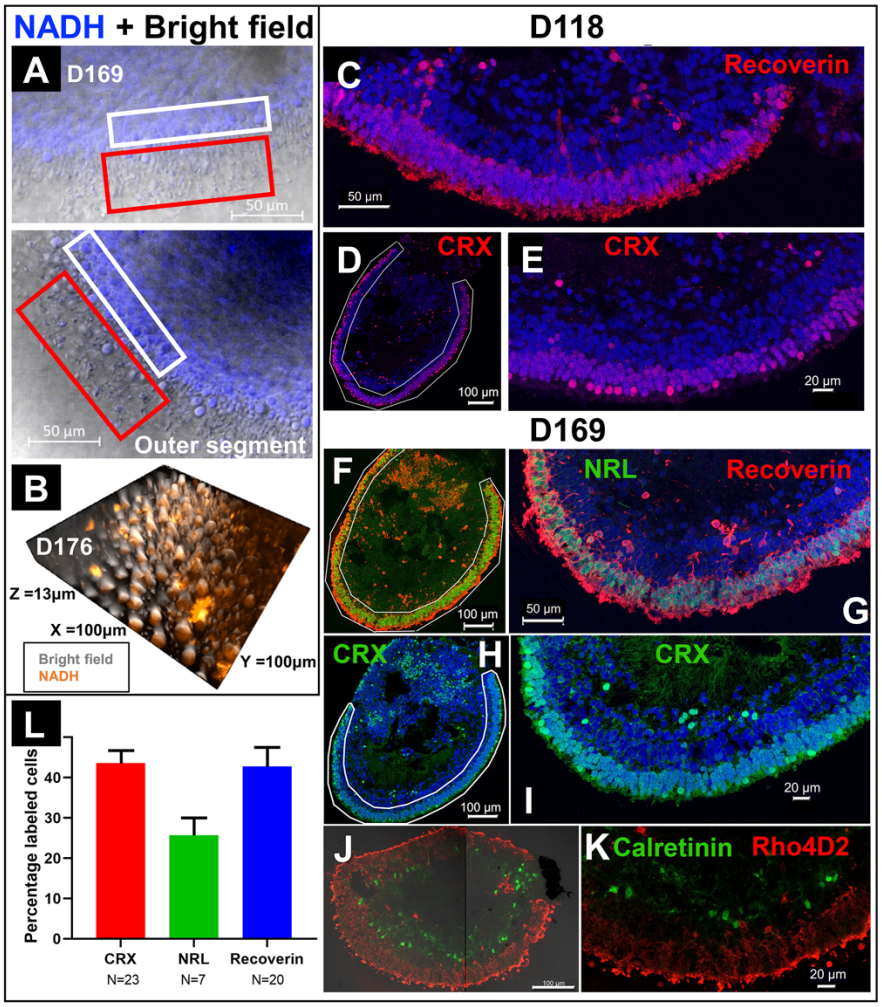

Figure 4.5: Comparison of immunohistology and 2P autofluorescence imaging.

(A) Live imaging of a RtOg on D169 of differentiation using 2P microscopy (combination of brightfield and NADH autofluorescence). The white box frames the outer nuclear layer (ONL) and the red box the outer segment-like structures. (B) 3-D reconstruction from Z-stack images of the surface of a RtOg on D176 with 2P microscopy (combination of brightfield and NADH autofluorescence). (C-E) Immunohistology images of a RtOg at D118. (F-K) Immunohistology images of a RtOg on D169. (L) Cell counting plot from selected immunohistology slides (Error bar is the standard error of the mean). Antibody-marked cells: Recoverin and CRX – photoreceptor cells; NRL – rod photoreceptor cells; Rho4D2 – rod photoreceptor cells; Calretinin – amacrine cells. Nucleus were stained with DAPI (blue).

4.4 Discussion

The functional imaging results in our work showed the different developmental stages in RtOg progression that were consistent with published literature [1, 78]. Stem cells are known to be glycolytic (green/yellow color coding for high f/b NADH ratio). As they differentiate, their metabolic activities progress toward more oxidative phosphorylation (red/purple color coding for low f/b NADH ratio) [200, 232]. As RtOgs mature, their outermost surface develops photoreceptors with a glycolytic signature and retinol accumulation consistent with prior observations [78]. These time-dependent metabolic signatures are powerful indicators in determining and predicting RtOg differentiation stages.

The scRNA-seq data offered a comprehensive profile of RtOgs' cell type in early and mature differentiation stages. Metabolic imaging indicated that RtOgs were more proliferative in the early stage, confirming scRNA-seq and qPCR data that more progenitor cell markers were expressed. Further, FLIM also showed that the shift to a more differentiated stage started between the 2nd to the 3rd month and stabilized in the 4th month and afterwards. The gene expression profile by qPCR also demonstrated this trend because mature photoreceptor genes were gradually expressed after two months of differentiation. However, although higher than human fetal retina, the matured photoreceptor gene expression level of the RtOgs after 4 months was still not comparable to human adult retina, which is one of the intrinsic limitations of *in vitro* organ differentiation.

Compared with conventional RtOg characterization methods such as immunohistology and qPCR, 2PM has the outstanding advantage of noninvasive live tissue

imaging. In section 3.3, we showed that 2PM was superior in examining the outer segment structures than immunohistology, which required preparation procedures including fixation, wash, and microtome that destroyed most of the delicate outer structures. Thus, in immunohistology, only a few slides sectioned at certain orientations showed partial outer segment structures. Further, 2PM FLIM and HSpec can also recapitulate the laminar structures on the RtOg surface at the cellular and molecular levels that are comparable to those obtained from immunohistology. Most importantly, 2PM approaches significantly reduce photodamage, allowing non-destructive RtOg characterization.

However, RtOgs in this study showed tissue heterogeneity initially and as differentiation progressed beyond 3 months. As shown in **Fig. 4.2B**, the variations in f/b NADH ratios were higher during both early and late stages. To ensure analysis uniformity and consistency, we only chose the outer surface of each organoid to image and analyze the f/b NADH ratio. While the gene expression and scRNA-seq validated that photoreceptor cells were differentiated, not all organoids were able to develop an uniform and laminated photoreceptor layer on their outer surface, and the thickness of the laminar structure also varied, especially in the stages that organoids rapidly proliferated or differentiated. Further, only a few RtOg samples in the 4-6-month age range showed outer segment structures. In addition to biological heterogeneity intrinsic to developing RtOgs, the error from manual maintenance of retinal tissue in suspended dish culture may also cause a visible morphological difference among organoids in the 6 months range. To address this issue, we are developing an automated long-term culture bioreactor for nearly labor-free RtOg maintenance [1]. When optimized and integrated with 2PM imaging system, the automated bioreactor can potentially increase imaging efficiency and allow scaled-up

process and characterization of RtOg production. On this matter, 2PM is also a promising noninvasive method to evaluate the consistency of RtOgs quality differentiated from different culture protocols.

Beyond RtOg characterization, 2PM can be developed further as a tool for *in vivo* examination on animal models transplanted with RtOgs. Previous studies showed its applicability in mouse [233] and primate [234] models. The optimized conditions can be achieved by testing and adjusting the laser power [235] and temporal specifications [236]. In addition to the two imaging modalities introduced in this study, there are other noninvasive methodologies can be applied to organoid research. Browne et al. has used optical coherence tomography (OCT) to image live RtOgs and found a reflectivity difference on the RtOgs' surface [78]. Furthermore, Scholler et al. developed a dynamic full-field OCT system to image live RtOgs and provided 3-dimensional color images that reflected organelle motility with sub-micrometer spatial resolution and millisecond temporal resolution [79]. Dutta et al. used vis/near-infrared (NIR) spectroscopy to study the neurodevelopment of brain organoids [237]. Recently, Hedde et al. implemented the sine/cosine snapshot phasor-based hyperspectral imaging method to image zebrafish retina and organelles, and significantly improved imaging speed when working together with light sheet microscopy [225]. Overall, noninvasive imaging technologies are inevitably rising as valuable tools to investigate structural and functional biology.

4.5 Conclusions

We have demonstrated a 2PM-based noninvasive imaging technique to monitor RtOg metabolic and structural changes at the cellular level throughout the entire

differentiation and development process. The long-term functional imaging data showed that RtOgs from different cell lines and different batches exhibited a repeatable and predictable metabolic developmental process from more proliferative at an early stage to more differentiated at a later stage. The metabolic signature stabilized after 4 months, which was consistent with the time point in gene expression profile stabilization. The methodology and the findings of this study are of great value in live RtOgs characterization and monitoring, offering a potentially powerful tool in screening and quality control for RtOg production.

Chapter 5 : Pilot studies and Future Directions

5.1 Introduction

This chapter includes pilot data produced in two feasibility studies that showed promises but required further studies to establish vigorous scientific conclusions. Section 5.2 describes the initial work on testing the effect of different immunosuppressants on RtOgs. Section 5.3 describes the preliminary studies of RtOg function using a high-density Microelectrode array. In conclusion, Section 5.4 discusses possible future directions of RtOgs research.

5.2 Effects of Immunosuppressant Drugs on RtOgs

Organ transplants often require the use of immunosuppressant to prevent organ rejection. As a result, the transplanted organs must be compatible with the use of immunosuppressants. Similarly, RtOg's resilience to immunosuppressing medications is critical to ensure clinical success when used as transplanted tissues into the eye.

In this pilot study, we evaluated how the immunosuppressing drugs Tacrolimus (TAC) and mycophenolic acid (MPA) would affect RtOgs metabolic activity *in vitro*, either alone or in combination at the commonly used dosages [238]. In brief, TAC renders the immune cells inactive by bonding to an immunophilin – FK506 binding proteins (FKBPs). The TAC/FKBP12 complex inhibits calcineurin, which is a key rate-limiting enzyme in T-cell signal transduction, and subsequently results in the biological effect of immunosuppression [239]. MPA is an inhibitor of inosine-5'-monophosphate

dehydrogenase. MPA suppresses immune responses by inhibiting specifically the proliferation of T and B lymphocytes through the depletion of guanosine nucleotides [240].

Results on 2 different sets of RtOgs (TR61 and TR52) indicated that there was no significant difference of free/bound NADH ratio between treated groups and control at 1 and 4 weeks of culture (**Fig. 5.1**).

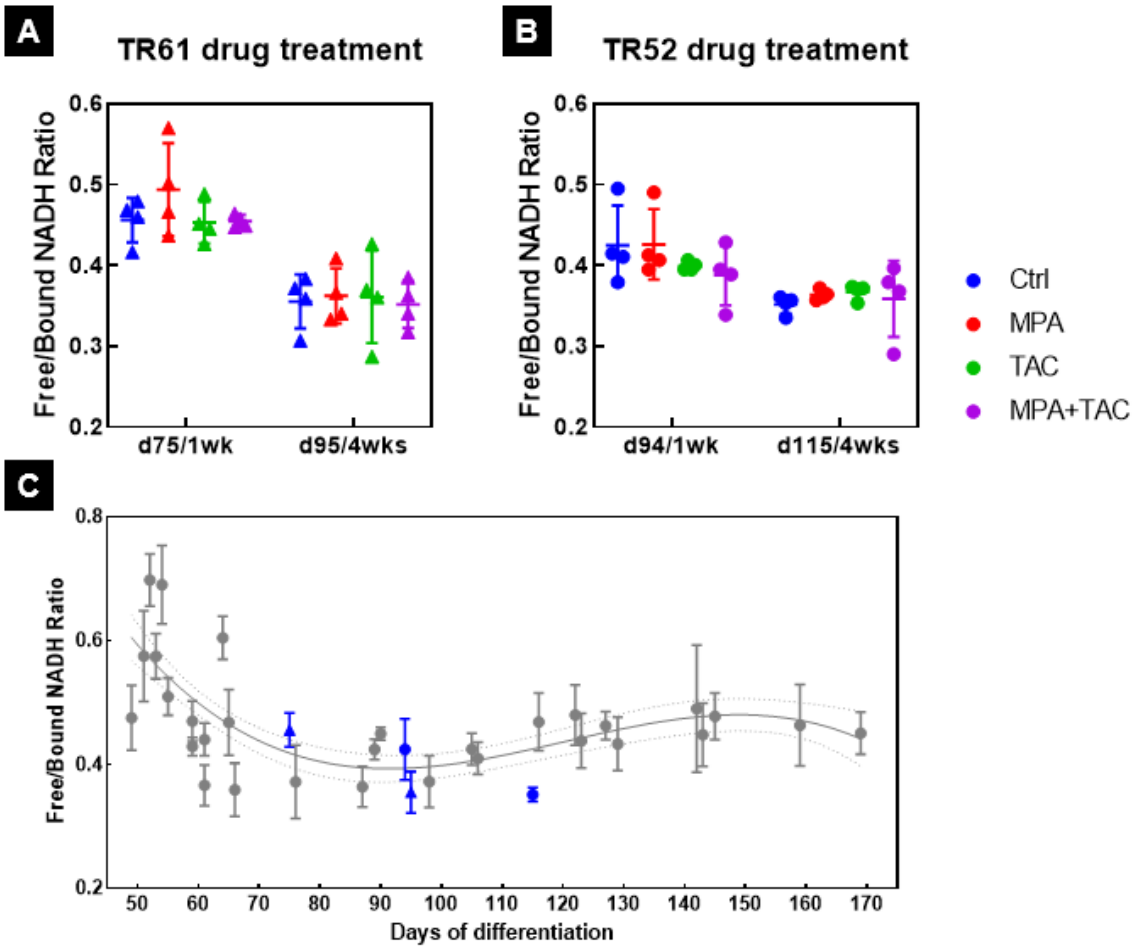

Figure 5.1**: Influence of immunosuppressant drugs on RtOgs long-term metabolic activity.**

Two different sets of organoids (TR61 and TR52) were tested after 1-week and 4-week exposure to MPA (0.5 µg/ml), TAC (3 ng/ml) or a combination of both at the lowest

effective concentration reported for human clinical trials. No significant difference was detected (one-way ANOVA) between drug-treated organoids and controls (n=4 in each group), which is promising towards testing the hypothesis that immunosuppressants at commonly used dosages would be safe for RtOgs. Further studies should involve a rigorous design of experiment with RtOgs at different developmental stages, a broader range of immunosuppressant dosages, and higher number of experiments (*n*) to establish statistical significance.

5.3 RtOgs Functional Test Using High-Density Microelectrode Array

Fully functional RtOgs should respond to light stimuli. The purpose of this pilot study was to apply an advanced electrophysiology testing system (MaxWell Biosystems, Zurich, Switzerland) to verify the functionality of matured RtOgs cultured in the bioreactor platform described in Chapter 3.

Several RtOgs were derived from the CRX-GFP genetically modified human embryonic stem cell (hESC) line [45] and cultured in the microfluidic bioreactor from day 103 to 170. On day 170, two RtOgs with outer segment structures were cut into half, with the inner layer retinal cells facing down and seeded on two high-density microelectrode arrays (HD-MEA) wells. Spontaneous spiking from RGCs and those as a result of light stimulation were measured using the full scan and network recording modes provided by the MaxOne recording system. A qualitative light stimulation test was done by using flashlight from a cell phone scanning on top of the MEA chip (light intensity = 1306 Lux). The second light stimulation experiment used natural light generated from a multi-spectral light source with controlled intensities (ranging from 20.57 to 883.92 lux). CRX-GFP stem

cells were used as negative control in MEA recording with the same light exposure. RtOgs were cultured on the HD-MEA system from day 170 to 204 and dark-adapted before the light stimulation experiment. The procedure is illustrated in **Fig. 5.2**.

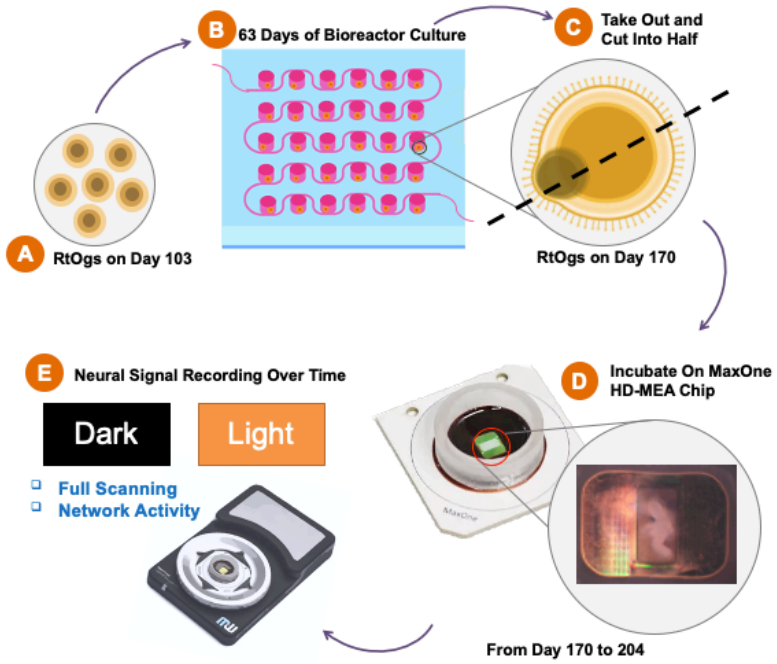

Figure 5.2: Overview of experimental procedure.

(A)–(B) RtOgs cultured on the microfluidic bioreactor system from day 103 to 170; (C) On day 170, two RtOgs with outer segment structures were cut in half, with the inner layer of the RtOg facing down, one on each of the two MaxOne high-density microelectrode arrays (HD- MEA) wells; (D) RtOgs were cultured on the MaxOne HD-MEA wells from day 170 to 204; (E) Spontaneous spiking from retinal cells in contact with the electrodes and spikes as a result of light stimulation were measured using the full scan and network recording modes provided by the MaxOne recording system.

Spontaneous spiking of retinal cells was observed initially on day 184 (**Fig. 5.3C**), the total firing rate (**Fig. 5.3I**) and the number of spikes per burst (**Fig. 5.3J**) increased over time. Denser raster scanning plot, increased firing rate, and higher number of spikes per

burst were all observed as a result of light stimulation, indicating that the retinal tissues could be responding to light stimulation.

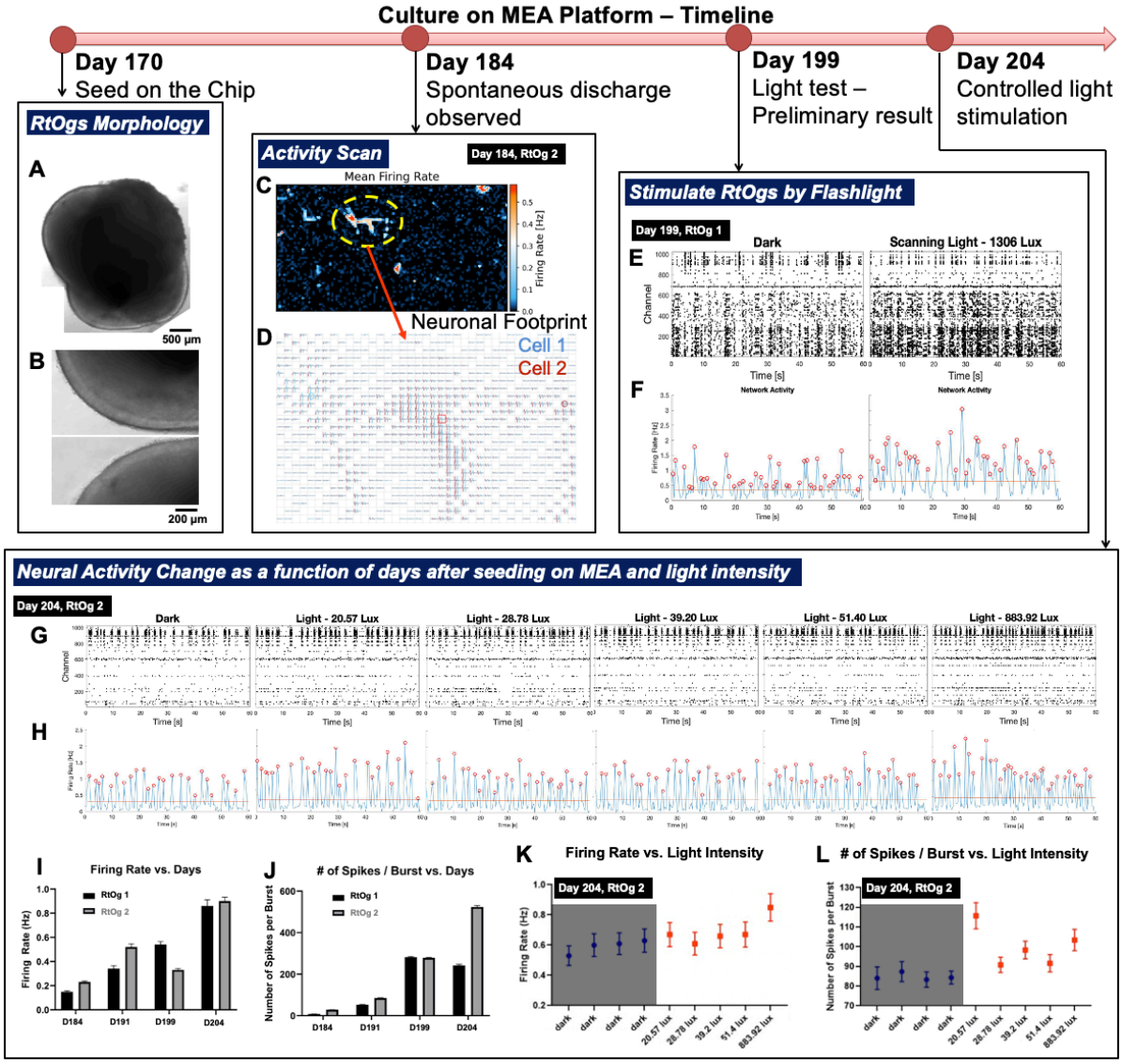

Figure 5.3: Timeline and experiments on the HD-MEA platform.

(A)–(B) Phase contrast image of the tested RtOg on day 170; (C)–(D) Full activity scan showed the mean firing rate across all electrodes on the HD-MEA. Spontaneous discharge of retinal cells was observed on day 184. Neuronal recording was able to decode the action potentials from different cells; (E)–(F) Raster scan and network activity from the flashlight stimulation experiment on day 199; (G)–(H) Raster scan and network activity from the

controlled intensity light stimulation experiment on day 204; (I) Plot of firing rate change with days; (J) Plot of number of spikes per burst change with days; (K) Plot of firing rage change versus different light intensity; (L) Plot of number of spikes per burst versus different light intensity.

In summary, RtOgs cultured in the microfluidic bioreactor system developed inner retinal cells and photoreceptor layers as indicated with histochemistry, and possibly the neural pathway in between. The HD-MEA recording system used in this study achieved *in vitro* longitudinal live recording of the RtOgs' electrophysiological behaviors. The initial results indicated that RtOg spiking activities could be measured and potentially quantified with or without external stimuli. Further studies with well-controlled and quantified light stimuli should elucidate photoreceptor activities in different stages of development.

5.4 Future Directions

Although we have made substantial progress in studying RtOgs, there are still several aspects that can be improved in future research. First, the procedure of RtOgs' initiation should be optimized. The current approach involved 2D differentiation and manual cutting of RtOgs, which is both labor intensive and dependent on technicians' subjective judgment. Switching to all 3D differentiation can improve RtOgs initiation efficiency. More studies can also be done to improve RtOg reproducibility. Second, the current bioreactor designs were based on connecting all chambers in a series with perfusion channels. This design worked well with a limited number of RtOgs. However, if more RtOgs are to be cultured in this design, the downward gradient in media concentration from the inlet to the outlet inside the perfusion channel may unevenly affect

the growth of RtOgs. To improve upon the current design, bioreactors with parallel chambers were conceived, fabricated, and initially tested. The challenge for the parallel design is to guarantee a uniform flow rate in each of the parallel branches and to avoid the possibility of bubble generation inside the more elaborate channels. Once these problems are solved, the design can be applied to culturing significantly more RtOgs in one batch. Lastly, to further validate the functionality and metabolic changes of RtOgs in the long term, more experiments should be performed, especially augmenting with electrophysiology tests and gene analysis. The long-term characterization of RtOgs can be improved by deep learning trained with a large set of data accumulated from additional experiments on the morphologies, metabolic signatures and structures of RtOgs in different developmental stages.

Appendix

Information of qPCR primers

Gene name	Official full name	GeneGlobe ID
CHX10 (VSX2)	Visual system homeobox 2	QT00221081
NRL	Neural retina leucine zipper	QT01005165
RAX	Retina and anterior neural fold homeobox	QT00212667
RCVRN	Recoverin	QT00014098
ARR3	Arrestin 3	QT00000182
SAG	S-antigen visual arrestin	QT01007958
PRPH2	Peripherin 2	QT00094094
GNAT	G-protein subunit alpha transducin	QT00235606
GNAT2	G-protein subunit alpha transducin 2	QT00008764
RHO	Rhodopsin	QT01017058
OPN1SW	Opsin 1, short wave sensitive	QT00017304
OPN1MW	Opsin 1, medium wave sensitive	QT00040887
OPN1LW	Opsin 1, long wave sensitive	QT01007356
RPL7	Ribosomal protein L7	QT01670137

Information of Antibodies

Antibody	Species	Concentration	Manufacturer	Catalogue #	RRID
Rhodopsin (Rho4D2)	Mouse	1:100	Gift of Dr. Molday [241], University of British Columbia	N/A	AB_2315273 AB_2315274
Human NRL	Goat	1:100	R&D Systems	AF2945	AB_2155098
Recoverin	Rabbit	1:2000	Millipore	AB5585	AB_2253622
Calretinin	Goat	1:100	Novus	AF5065	AB_2068516
OTX2	Rabbit	1:1000	ThermoFisher	701948	AB_2608961
CHX10	Mouse	1:100	Santa Cruz	sc-365519	AB_10842442
RG-opsin	Rabbit	1:1000	Millipore	AB5405	AB_177456
Synaptophysin	Goat	1:100	Novus	AF5555	AB_2198864
PKC alpha	Rabbit	1:200	Oxford Biomedical	PK13	N/A
CRALBP	Rabbit	1:2000	Fitzgerald	70R-19906	N/A

Key Reagents and Resources

Reagents or Resource	Source	Identifier
mTeSR 1 media	STEMCELL Technologies	Cat# 85850
ReLeSR	STEMCELL Technologies	Cat# 100-0484
Vitronectin XF™	STEMCELL Technologies	Cat# 07180
Accutase	Nacalai USA, Inc	Cat# NU1267954
Growth factor reduced Matrigel	Corning	Cat# 354230
Dulbecco's modified eagle medium (DMEM)	Gibco	Cat# 12100-038
F12 Nutrient Mixture	Gibco	Cat# 21700-026
N2 supplement	Gibco	Cat# 17-502-048
Minimum essential media non-essential amino acids (NEAA)	Gibco	Cat# 11140-050
L-glutamine 200mM (100X)	Gibco	Cat# 25030-081
Heparin	Sigma-Aldrich	CAS 9041-08-1
B27 supplement (50X) (minus vitamin A)	Gibco	Cat# 1587-010
B27 Plus supplement (50X)	Gibco	Cat# A3582801
Taurine	Sigma-Aldrich	CAS# 107-35-7
Heat inactivated 10% fetal bovine serum (FBS)	Gibco	Cat# 10438-026
bFGF	Peprotech	Cat# 100-18B
Activin-A	Peprotech	Cat# 120-14E
Collagenase IV	Gibco	Cat# 17104019
Anti-cell adherence solution	STEMCELL Technologies	Cat# 07010
Dulbecco's phosphate-buffered saline (DPBS) without calcium and magnesium (10X)	STEMCELL Technologies	Cat# 37354
TRIzol reagent	Fisher	Cat# 15596026
DNase I	Invitrogen TURBO	Cat# AM2238
Phenol/Chloroform/Isoamyl Alcohol	Fisher	Cat# BP1752I-400
RT² cDNA synthesis kit	Qiagen	Cat# 330401

ROX qPCR master mix	Qiagen	Cat# 330530
Worthington papain dissociation system	Worthington	http://www.worthington-biochem.com/PDS/cat.html
10X Genomics Chromium Single Cell 3' Reagent Kit v3.1	10X Genomics	N/A
Kapa qPCR Library	Roche	Cat# 07960140001
Histo-VT One	Nacalai	Product# 06380-05
Vectashield Vibrance Antifade Mounting Medium	Vector Labs	Cat# H-1700
Standard clear resin	Formlabs	Cat# RS-F2-GPCL-04
Optimum cutting temperature (OCT) compound (PolarStat Plus, StatLab, McKinney, TX, USA)	Ted Pella Inc.	Product# 27301-1
Critical Commercial Assays		
0.6X SPRIselect	Beckman Coulter	Cat# B23318
Qubit DNA HS assay	Life Technologies	Cat Q32851
Agilent 2100 Bioanalyzer DNA HS	Agilent	Cat# 5067-1504
Experimental Models: Cell Lines		
hESC, CRX-GFP H9	Dr. Majlinda Lako, Newcastle University [76, 81, 173], UK	Derived from NIH registration #004
hESCs, CSC-14	AIVITA Biomedical Inc.	NIH registration #0284
Equipment and Culture Plates		
Formlabs Form 3B	Formlabs	N/A
Harrick	Harrick Plasma	N/A
#1.5, 64*50 mm, ClariTex	Ted Pella Inc.	Cat# 260378
Humidified 5% CO_2 incubator	Nuaire	N/A
EZSPHERE 12-well plate (D: 800μm, d: 400μm]	Nacalai USA, Inc	Cat# TCI-4815-903SP-10P
Ultra-low attachment Corning Costar 24-well plate	Corning	Cat# 07-200-602
CoolCLAVE Plus	Genlantis	N/A
50 mL Steriflip-GP sterile centrifuge tube with filter cap pore size 0.22 μm	Millipore Sigma	Cat# SCGP00525

MicroAmp™ optical adhesive film	Thermo Fisher Scientific	Cat# 4311971
ESCO Class II Type A2 biosafety cabinet	ESCO Micro Pte. Ltd.	N/A
Zeiss LSM 780	Carl Zeiss	N/A
Mai Tai multi-photon laser source	Spectra-Physics Mai Tai	N/A
photomultiplier tube	Hamamatsu Photonics	H7422p-40
FastFLIM FLIMbox	ISS	N/A
Nunc® Lab-Tek® II Chambered Coverglass	Thermo Fisher	Cat# 155411
Olympus IX71	Olympus	N/A
QICAM FAST1394 CCD camera	Teledyne QImaging	N/A
Bio-Rad C1000 Thermocycler	Bio-Rad Laboratories	N/A
Dynabeads MyOne SILANE	Life Technologies	N/A
Illumina NovaSeq 6000	Illumina	N/A
Zeiss LSM700	Carl Zeiss	N/A
JEOL 2100	JEOL USA, Inc.	N/A
FEI Magellan 400 XHR	FEI Company	N/A
Software and Algorithms		
COMSOL Multiphysics 5.6	COMSOL, Inc.	N/A
SolidWorks 2020	SolidWorks Corp.	N/A
Graphpad Prism	Graphpad Software LLC	N/A
FASTQC	Babraham Bioinformatics	https://github.com/s-andrews/FastQC1
cellRanger v.3.1.0.	10X Genomics	N/A
Zen 3.3 Software	Zeiss	N/A
Adobe Photoshop	Adobe	N/A
Etomo	University of Colorado, Boulder	N/A

References

1. Xue, Y., et al., *Retinal organoids on-a-chip: a micro-millifluidic bioreactor for long-term organoid maintenance.* Lab Chip, 2021. **21**(17): p. 3361-3377.
2. Xue, Y., et al., *Retinal Organoids Long-term Functional Characterization Using Two-Photon Fluorescence Lifetime and Hyperspectral Microscopy.* Frontiers in Cellular Neuroscience, 2021. **15**: p. 796903.
3. Kallman, A., et al., *Investigating cone photoreceptor development using patient-derived NRL null retinal organoids.* Communications biology, 2020. **3**(1): p. 82-82.
4. Chirco, K.R., et al., *Allele-specific gene editing to rescue dominant CRX-associated LCA7 phenotypes in a retinal organoid model.* Stem Cell Reports, 2021. **16**(11): p. 2690-2702.
5. Huang, K.C., et al., *Morphological and Molecular Defects in Human Three-Dimensional Retinal Organoid Model of X-Linked Juvenile Retinoschisis.* Stem Cell Reports, 2019. **13**(5): p. 906-923.
6. Gao, M.L., et al., *Patient-Specific Retinal Organoids Recapitulate Disease Features of Late-Onset Retinitis Pigmentosa.* Front Cell Dev Biol, 2020. **8**: p. 128.
7. Zhang, X., W. Wang, and Z.B. Jin, *Retinal organoids as models for development and diseases.* Cell Regen, 2021. **10**(1): p. 33.
8. Gamm, D.M., et al., *The Role of FGF9 in the Production of Neural Retina and RPE in a Pluripotent Stem Cell Model of Early Human Retinal Development.* American Journal of Ophthalmology, 2019. **206**: p. 113-131.
9. Dorgau, B., et al., *Laminin γ3 plays an important role in retinal lamination, photoreceptor organisation and ganglion cell differentiation.* Cell death & disease, 2018. **9**(6): p. 615-615.
10. Eldred, K.C., et al., *Thyroid hormone signaling specifies cone subtypes in human retinal organoids.* Science, 2018. **362**(6411).
11. Bharathan, S.P., et al., *Characterization and staging of outer plexiform layer development in human retina and retinal organoids.* Development, 2021. **148**: p. dev199551.
12. Aasen, D.M. and M.N. Vergara, *New Drug Discovery Paradigms for Retinal Diseases: A Focus on Retinal Organoids.* J Ocul Pharmacol Ther, 2020. **36**(1): p. 18-24.
13. Kruczek, K., et al., *Gene Therapy of Dominant CRX-Leber Congenital Amaurosis using Patient Stem Cell-Derived Retinal Organoids.* Stem Cell Reports, 2021. **16**(2): p. 252-263.
14. Zhang, X., et al., *Gene correction of the CLN3 c.175G>A variant in patient-derived induced pluripotent stem cells prevents pathological changes in retinal organoids.* Mol Genet Genomic Med, 2021. **9**(3): p. e1601.
15. Garita-Hernandez, M., et al., *Control of Microbial Opsin Expression in Stem Cell Derived Cones for Improved Outcomes in Cell Therapy.* Front Cell Neurosci, 2021. **15**: p. 648210.
16. Völkner, M., et al., *Optimized Adeno-Associated Virus Vectors for Efficient Transduction of Human Retinal Organoids.* Hum Gene Ther, 2021. **32**(13-14): p. 694-706.
17. Santos-Ferreira, T.F., O. Borsch, and M. Ader, *Rebuilding the Missing Part-A Review on Photoreceptor Transplantation.* Front Syst Neurosci, 2016. **10**: p. 105.

18. McLelland, B.T., et al., *Transplanted hESC-derived retina organoid sheets differentiate, integrate, and improve visual function in retinal degenerate rats.* Invest Ophthalmol Vis Sci, 2018. **59**(6): p. 2586-2603.

19. Gasparini, S.J., et al., *Transplantation of photoreceptors into the degenerative retina: Current state and future perspectives.* Prog Retin Eye Res, 2019. **69**: p. 1-37.

20. Akiba, R., et al., *Quantitative and Qualitative Evaluation of Photoreceptor Synapses in Developing, Degenerating and Regenerating Retinas.* Frontiers in Cellular Neuroscience, 2019. **13**: p. 16-16.

21. Lin, B., et al., *Retina Organoid Transplants Develop Photoreceptors and Improve Visual Function in RCS Rats With RPE Dysfunction.* Invest Ophthalmol Vis Sci, 2020. **61**(11): p. 34.

22. Singh, R.K., et al., *Pluripotent Stem Cell-Based Organoid Technologies for Developing Next-Generation Vision Restoration Therapies of Blindness.* J Ocul Pharmacol Ther, 2021. **37**(3): p. 147-156.

23. Matsuyama, T., et al., *Genetically engineered stem cell-derived retinal grafts for improved retinal reconstruction after transplantation.* iScience, 2021. **24**(8): p. 102866.

24. Gehlbach, P., T. Li, and E. Hatef, *Statins for age-related macular degeneration.* Cochrane Database Syst Rev, 2016. **2016**(8): p. Cd006927.

25. Lim, L.S., et al., *Age-related macular degeneration.* Lancet, 2012. **379**(9827): p. 1728-38.

26. Chichagova, V., et al., *Cellular regeneration strategies for macular degeneration: past, present and future.* Eye (London, England), 2018. **32**(5): p. 946-971.

27. Daiger, S.P., S.J. Bowne, and L.S. Sullivan, *Perspective on genes and mutations causing retinitis pigmentosa.* Arch Ophthalmol, 2007. **125**(2): p. 151-8.

28. Hartong, D.T., E.L. Berson, and T.P. Dryja, *Retinitis pigmentosa.* Lancet, 2006. **368**(9549): p. 1795-809.

29. Botto, C., et al., *Early and late stage gene therapy interventions for inherited retinal degenerations.* Progress in Retinal and Eye Research, 2021: p. 100975.

30. Wood, E.H., et al., *The retina revolution: signaling pathway therapies, genetic therapies, mitochondrial therapies, artificial intelligence.* Curr Opin Ophthalmol, 2020. **31**(3): p. 207-214.

31. De Silva, S.R., et al., *Long-term restoration of visual function in end-stage retinal degeneration using subretinal human melanopsin gene therapy.* Proceedings of the National Academy of Sciences of the United States of America, 2017. **114**(42): p. 11211-11216.

32. Campochiaro, P.A., et al., *Oral N-acetylcysteine improves cone function in retinitis pigmentosa patients in phase I trial.* The Journal of clinical investigation, 2020. **130**(3): p. 1527-1541.

33. Komeima, K., et al., *Antioxidants reduce cone cell death in a model of retinitis pigmentosa.* Proc Natl Acad Sci U S A, 2006. **103**(30): p. 11300-5.

34. Komeima, K., B.S. Rogers, and P.A. Campochiaro, *Antioxidants slow photoreceptor cell death in mouse models of retinitis pigmentosa.* J Cell Physiol, 2007. **213**(3): p. 809-15.

35. Farrar, G.J., et al., *Gene therapies for inherited retinal disorders.* Vis Neurosci, 2014. **31**(4-5): p. 289-307.

36. Yamasaki, S., et al., *Low Immunogenicity and Immunosuppressive Properties of Human ESC- and iPSC-Derived Retinas.* Stem cell reports, 2021. **16**(4): p. 851-867.

37. Kramer, J., K.R. Chirco, and D.A. Lamba, *Immunological Considerations for Retinal Stem Cell Therapy.* Adv Exp Med Biol, 2019. **1186**: p. 99-119.

38. West, E.L., et al., *Long - term survival of photoreceptors transplanted into the adult murine neural retina requires immune modulation.* Stem Cells, 2010. **28**(11): p. 1997-2007.

39. Zhu, J., et al., *Immunosuppression via Loss of IL2rγ Enhances Long-Term Functional Integration of hESC-Derived Photoreceptors in the Mouse Retina.* Cell Stem Cell, 2017. **20**(3): p. 374-384.e5.

40. Zhu, J., et al., *Generation of Transplantable Retinal Photoreceptors from a Current Good Manufacturing Practice-Manufactured Human Induced Pluripotent Stem Cell Line.* Stem Cells Transl Med, 2018. **7**(2): p. 210-219.

41. Thomas, B.B., et al., *A new immunodeficient retinal dystrophic rat model for transplantation studies using human-derived cells.* Graefes Arch Clin Exp Ophthalmol, 2018. **256**(11): p. 2113-2125.

42. Zerti, D., et al., *Transplanted pluripotent stem cell-derived photoreceptor precursors elicit conventional and unusual light responses in mice with advanced retinal degeneration.* Stem Cells 2021. **39**(7): p. 882-896.

43. Lakowski, J., et al., *Isolation of Human Photoreceptor Precursors via a Cell Surface Marker Panel from Stem Cell-Derived Retinal Organoids and Fetal Retinae.* Stem Cells, 2018. **36**(5): p. 709-722.

44. Liu, Y.V., et al., *Quantifiable In Vivo Imaging Biomarkers of Retinal Regeneration by Photoreceptor Cell Transplantation.* Transl Vis Sci Technol, 2020. **9**(7): p. 5.

45. Collin, J., et al., *CRX Expression in Pluripotent Stem Cell-Derived Photoreceptors Marks a Transplantable Subpopulation of Early Cones.* Stem Cells, 2019. **37**(5): p. 609-622.

46. Garita-Hernandez, M., et al., *Restoration of visual function by transplantation of optogenetically engineered photoreceptors.* Nature communications, 2019. **10**(1): p. 4524-4524.

47. Ribeiro, J., et al., *Restoration of visual function in advanced disease after transplantation of purified human pluripotent stem cell-derived cone photoreceptors.* Cell Rep, 2021. **35**(3): p. 109022.

48. Iraha, S., et al., *Establishment of immunodeficient retinal degeneration model mice and functional maturation of human ESC-derived retinal sheets after transplantation.* Stem cell reports, 2018. **10**(3): p. 1059-1074.

49. Mandai, M., et al., *iPSC-Derived Retina Transplants Improve Vision in rd1 End-Stage Retinal-Degeneration Mice.* Stem cell reports, 2017. **8**(1): p. 69-83.

50. Tu, H.-Y., et al., *Medium-to long-term survival and functional examination of human iPSC-derived retinas in rat and primate models of retinal degeneration.* EBioMedicine, 2019. **39**: p. 562-574.

51. Lin, B., et al., *Sheets of human retinal progenitor transplants improve vision in rats with severe retinal degeneration.* Exp Eye Res, 2018. **174**: p. 13-28.

52. Thomas, B.B., et al., *Co-grafts of Human Embryonic Stem Cell Derived Retina Organoids and Retinal Pigment Epithelium for Retinal Reconstruction in Immunodeficient Retinal Degenerate Royal College of Surgeons Rats.* Frontiers in Neuroscience, 2021. **15**: p. 752958.

53. Llonch, S., M. Carido, and M. Ader, *Organoid technology for retinal repair.* Dev Biol, 2018. **433**(2): p. 132-143.

54. Völkner, M., et al., *Mouse Retinal Organoid Growth and Maintenance in Longer-Term Culture.* Front Cell Dev Biol, 2021. **9**: p. 645704.

55. Bell, C.M., D.J. Zack, and C.A. Berlinicke, *Human Organoids for the Study of Retinal Development and Disease.* Annu Rev Vis Sci, 2020. **6**: p. 91-114.

56. Capowski, E.E., et al., *Reproducibility and staging of 3D human retinal organoids across multiple pluripotent stem cell lines.* Development (Cambridge, England), 2019. **146**(1): p. dev171686.

57. Zerti, D., et al., *Developing a simple method to enhance the generation of cone and rod photoreceptors in pluripotent stem cell-derived retinal organoids.* Stem Cells 2020. **38**(1): p. 45-51.

58. Ueda, K., et al., *Generation of three-dimensional retinal organoids expressing rhodopsin and S- and M-cone opsins from mouse stem cells.* Biochem Biophys Res Commun, 2018. **495**(4): p. 2595-2601.

59. Kaya, K.D., et al., *Transcriptome-based molecular staging of human stem cell-derived retinal organoids uncovers accelerated photoreceptor differentiation by 9-cis retinal.* Mol Vis, 2019. **25**: p. 663-678.

60. Kelley, R.A., et al., *Accelerated Development of Rod Photoreceptors in Retinal Organoids Derived from Human Pluripotent Stem Cells by Supplementation with 9-cis Retinal.* STAR Protoc, 2020. **1**(1).

61. Pan, D., et al., *COCO enhances the efficiency of photoreceptor precursor differentiation in early human embryonic stem cell-derived retinal organoids.* Stem Cell Res Ther, 2020. **11**(1): p. 366.

62. Mellough, C.B., et al., *Systematic Comparison of Retinal Organoid Differentiation from Human Pluripotent Stem Cells Reveals Stage Specific, Cell Line, and Methodological Differences.* Stem Cells Transl Med, 2019. **8**(7): p. 694-706.

63. Nakano, T., et al., *Self-formation of optic cups and storable stratified neural retina from human ESCs.* Cell Stem Cell, 2012. **10**(6): p. 771-785.

64. Wahlin, K.J., et al., *Photoreceptor Outer Segment-like Structures in Long-Term 3D Retinas from Human Pluripotent Stem Cells.* Sci Rep, 2017. **7**(1): p. 766.

65. Zhong, X., et al., *Generation of three-dimensional retinal tissue with functional photoreceptors from human iPSCs.* Nat Commun, 2014. **5**: p. 4047.

66. Meyer, J.S., et al., *Modeling early retinal development with human embryonic and induced pluripotent stem cells.* Proc Natl Acad Sci U S A, 2009. **106**(39): p. 16698-703.

67. Dorgau, B., et al., *Decellularised extracellular matrix-derived peptides from neural retina and retinal pigment epithelium enhance the expression of synaptic markers and light responsiveness of human pluripotent stem cell derived retinal organoids.* Biomaterials, 2019. **199**: p. 63-75.

68. Hunt, N.C., et al., *3D culture of human pluripotent stem cells in RGD-alginate hydrogel improves retinal tissue development.* Acta Biomaterialia, 2017. **49**: p. 329-343.

69. Kim, S., et al., *Generation, transcriptome profiling, and functional validation of cone-rich human retinal organoids.* Proc Natl Acad Sci U S A, 2019. **116**(22): p. 10824-10833.

70. Ovando-Roche, P., et al., *Use of bioreactors for culturing human retinal organoids improves photoreceptor yields.* Stem Cell Res Ther, 2018. **9**(1): p. 156.

71. DiStefano, T., et al., *Accelerated and Improved Differentiation of Retinal Organoids from Pluripotent Stem Cells in Rotating-Wall Vessel Bioreactors.* Stem Cell Reports, 2018. **10**(1): p. 300-313.

72. Yu, F., W. Hunziker, and D. Choudhury, *Engineering microfluidic organoid-on-a-chip platforms.* Micromachines, 2019. **10**(3): p. 165.

73. Achberger, K., et al., *Merging organoid and organ-on-a-chip technology to generate complex multi-layer tissue models in a human retina-on-a-chip platform.* Elife, 2019. **8**.

74. Langer, K.B., et al., *Retinal Ganglion Cell Diversity and Subtype Specification from Human Pluripotent Stem Cells.* Stem Cell Reports, 2018. **10**(4): p. 1282-1293.

75. Zerti, D., et al., *Understanding the complexity of retina and pluripotent stem cell derived retinal organoids with single cell RNA sequencing: current progress, remaining challenges and future prospective.* Current Eye Research, 2020. **45**(3): p. 385-396.

76. Collin, J., et al., *Deconstructing retinal organoids: single cell RNA‐Seq reveals the cellular components of human pluripotent stem cell‐derived retina.* Stem Cells, 2019. **37**(5): p. 593-598.

77. Phillips, M.J., et al., *A Novel Approach to Single Cell RNA-Sequence Analysis Facilitates In Silico Gene Reporting of Human Pluripotent Stem Cell-Derived Retinal Cell Types.* Stem Cells, 2018. **36**(3): p. 313-324.

78. Browne, A.W., et al., *Structural and Functional Characterization of Human Stem-Cell-Derived Retinal Organoids by Live Imaging.* Invest Ophthalmol Vis Sci, 2017. **58**(9): p. 3311-3318.

79. Scholler, J., et al., *Dynamic full-field optical coherence tomography: 3D live-imaging of retinal organoids.* Light: Science & Applications, 2020. **9**(1): p. 140.

80. Phillips, M.J., et al., *Generation of a rod-specific NRL reporter line in human pluripotent stem cells.* Scientific reports, 2018. **8**(1): p. 2370-2370.

81. Collin, J., et al., *Using zinc finger nuclease technology to generate CRX‐reporter human embryonic stem cells as a tool to identify and study the emergence of photoreceptors precursors during pluripotent stem cell differentiation.* Stem Cells, 2016. **34**(2): p. 311-321.

82. Vergara, M.N., et al., *Three-dimensional automated reporter quantification (3D-ARQ) technology enables quantitative screening in retinal organoids.* Development (Cambridge, England), 2017. **144**(20): p. 3698-3705.

83. Meyer, J.S., et al., *Optic vesicle-like structures derived from human pluripotent stem cells facilitate a customized approach to retinal disease treatment.* Stem Cells, 2011. **29**(8): p. 1206-18.

84. Mellough, C.B., et al., *IGF-1 Signaling Plays an Important Role in the Formation of Three-Dimensional Laminated Neural Retina and Other Ocular Structures From Human Embryonic Stem Cells.* Stem Cells, 2015. **33**(8): p. 2416-2430.

85. Reichman, S., et al., *Generation of Storable Retinal Organoids and Retinal Pigmented Epithelium from Adherent Human iPS Cells in Xeno-Free and Feeder-Free Conditions.* Stem Cells, 2017. **35**(5): p. 1176-1188.

86. Gagliardi, G., et al., *Characterization and Transplantation of CD73-Positive Photoreceptors Isolated from Human iPSC-Derived Retinal Organoids.* Stem Cell Reports, 2018. **11**(3): p. 665-680.

87. Garita-Hernandez, M., et al., *Optogenetic Light Sensors in Human Retinal Organoids.* Front Neurosci, 2018. **12**: p. 789.

88. Hallam, D., et al., *Human-Induced Pluripotent Stem Cells Generate Light Responsive Retinal Organoids with Variable and Nutrient-Dependent Efficiency.* Stem Cells, 2018. **36**(10): p. 1535-1551.

89. Afanasyeva, T.A.V., et al., *A look into retinal organoids: methods, analytical techniques, and applications.* Cell Mol Life Sci, 2021. **78**(19-20): p. 6505-6532.

90. Li, L., et al., *Electrophysiological characterization of photoreceptor-like cells in human inducible pluripotent stem cell-derived retinal organoids during in vitro maturation.* Stem Cells, 2021. **39**(7): p. 959-974.

91. Cowan, C.S., et al., *Cell Types of the Human Retina and Its Organoids at Single-Cell Resolution.* Cell, 2020. **182**(6): p. 1623-1640 e34.

92. Aboualizadeh, E., et al., *Imaging Transplanted Photoreceptors in Living Nonhuman Primates with Single-Cell Resolution.* Stem cell reports, 2020. **15**(2): p. 482-497.

93. Klassen, H.J., et al., *Multipotent retinal progenitors express developmental markers, differentiate into retinal neurons, and preserve light-mediated behavior.* Invest Ophthalmol Vis Sci, 2004. **45**(11): p. 4167-73.

94. MacLaren, R.E., et al., *Retinal repair by transplantation of photoreceptor precursors.* Nature, 2006. **444**(7116): p. 203-7.

95. Lakowski, J., et al., *Transplantation of Photoreceptor Precursors Isolated via a Cell Surface Biomarker Panel From Embryonic Stem Cell-Derived Self-Forming Retina.* Stem Cells, 2015. **33**(8): p. 2469-82.

96. Lakowski, J., et al., *Effective transplantation of photoreceptor precursor cells selected via cell surface antigen expression.* Stem Cells, 2011. **29**(9): p. 1391-404.

97. Lakowski, J., et al., *Cone and rod photoreceptor transplantation in models of the childhood retinopathy Leber congenital amaurosis using flow-sorted Crx-positive donor cells.* Hum Mol Genet, 2010. **19**(23): p. 4545-59.

98. Zou, T., et al., *Organoid-derived C-Kit(+)/SSEA4(-) human retinal progenitor cells promote a protective retinal microenvironment during transplantation in rodents.* Nat Commun, 2019. **10**(1): p. 1205.

99. Gust, J. and T.A. Reh, *Adult donor rod photoreceptors integrate into the mature mouse retina.* Invest Ophthalmol Vis Sci, 2011. **52**(8): p. 5266-72.

100. Pearson, R.A., et al., *Restoration of vision after transplantation of photoreceptors.* Nature, 2012. **485**(7396): p. 99-103.

101. Chao, J.R., et al., *Transplantation of Human Embryonic Stem Cell-Derived Retinal Cells into the Subretinal Space of a Non-Human Primate.* Translational vision science & technology, 2017. **6**(3): p. 4-4.

102. Santos-Ferreira, T., et al., *Retinal transplantation of photoreceptors results in donor–host cytoplasmic exchange.* Nature Communications, 2016. **7**(1).

103. Ortin-Martinez, A., et al., *A Reinterpretation of Cell Transplantation: GFP Transfer From Donor to Host Photoreceptors.* Stem Cells, 2017. **35**(4): p. 932-939.

104. Waldron, P.V., et al., *Transplanted Donor- or Stem Cell-Derived Cone Photoreceptors Can Both Integrate and Undergo Material Transfer in an Environment-Dependent Manner.* Stem Cell Reports, 2018. **10**(2): p. 406-421.

105. Simó, R., et al., *The retinal pigment epithelium: something more than a constituent of the blood-retinal barrier--implications for the pathogenesis of diabetic retinopathy.* J Biomed Biotechnol, 2010. **2010**: p. 190724.

106. Steinberg, R.H., *Interactions between the retinal pigment epithelium and the neural retina.* Doc Ophthalmol, 1985. **60**(4): p. 327-46.

107. Nishida, M., et al., *Human iPS cell derived RPE strips for secure delivery of graft cells at a target place with minimal surgical invasion.* Sci Rep, 2021. **11**(1): p. 21421.

108. Takagi, S., et al., *Evaluation of Transplanted Autologous Induced Pluripotent Stem Cell-Derived Retinal Pigment Epithelium in Exudative Age-Related Macular Degeneration.* Ophthalmology Retina, 2019. **3**(10): p. 850-859.

109. Sugita, S., et al., *Successful Transplantation of Retinal Pigment Epithelial Cells from MHC Homozygote iPSCs in MHC-Matched Models.* Stem Cell Reports, 2016. **7**(4): p. 635-648.

110. Kamao, H., et al., *Evaluation of the Surgical Device and Procedure for Extracellular Matrix-Scaffold-Supported Human iPSC-Derived Retinal Pigment Epithelium Cell Sheet Transplantation.* Invest Ophthalmol Vis Sci, 2017. **58**(1): p. 211-220.

111. Mandai, M., et al., *Autologous Induced Stem-Cell-Derived Retinal Cells for Macular Degeneration.* N Engl J Med, 2017. **376**(11): p. 1038-1046.

112. Kashani, A.H., et al., *A bioengineered retinal pigment epithelial monolayer for advanced, dry age-related macular degeneration.* Sci Transl Med, 2018. **10**(435).

113. da Cruz, L., et al., *Phase 1 clinical study of an embryonic stem cell-derived retinal pigment epithelium patch in age-related macular degeneration.* Nat Biotechnol, 2018. **36**(4): p. 328-337.

114. Kashani, A.H., et al., *One-Year Follow-Up in a Phase 1/2a Clinical Trial of an Allogeneic RPE Cell Bioengineered Implant for Advanced Dry Age-Related Macular Degeneration.* Transl Vis Sci Technol, 2021. **10**(10): p. 13.

115. Vitillo, L., V.E. Tovell, and P. Coffey, *Treatment of Age-Related Macular Degeneration with Pluripotent Stem Cell-Derived Retinal Pigment Epithelium.* Curr Eye Res, 2020. **45**(3): p. 361-371.

116. Uyama, H., M. Mandai, and M. Takahashi, *Stem-cell-based therapies for retinal degenerative diseases: Current challenges in the establishment of new treatment strategies.* Dev Growth Differ, 2021. **63**(1): p. 59-71.

117. German, O.L., et al., *Retinal pigment epithelial cells promote spatial reorganization and differentiation of retina photoreceptors.* Journal of neuroscience research, 2008. **86**(16): p. 3503-3514.

118. Kaempf, S., et al., *Novel organotypic culture model of adult mammalian neurosensory retina in co-culture with retinal pigment epithelium.* Journal of neuroscience methods, 2008. **173**(1): p. 47-58.

119. Aramant, R.B., M.J. Seiler, and S.L. Ball, *Successful cotransplantation of intact sheets of fetal retina with retinal pigment epithelium.* Invest Ophthalmol Vis Sci, 1999. **40**(7): p. 1557-64.

120. Radtke, N.D., et al., *Vision improvement in retinal degeneration patients by implantation of retina together with retinal pigment epithelium.* Am J Ophthalmol, 2008. **146**(2): p. 172-182.

121. Ghareeb, A.E., M. Lako, and D.H. Steel, *Coculture techniques for modeling retinal development and disease, and enabling regenerative medicine.* Stem cells translational medicine, 2020. **9**(12): p. 1531-1548.

122. Hunt, N.C., et al., *The Application of Biomaterials to Tissue Engineering Neural Retina and Retinal Pigment Epithelium.* Advanced Healthcare Materials, 2018. **7**(23): p. 1800226.

123. Lee, I.-K., et al., *Ultrathin micromolded 3D scaffolds for high-density photoreceptor layer reconstruction.* Science advances, 2021. **7**(17): p. eabf0344.

124. Jung, Y.H., et al., *3D Microstructured Scaffolds to Support Photoreceptor Polarization and Maturation.* Advanced Materials, 2018. **30**(39): p. 1803550.

125. Wu, Y.-R., et al., *Transplanted Mouse Embryonic Stem Cell-Derived Retinal Ganglion Cells Integrate and Form Synapses in a Retinal Ganglion Cell-Depleted Mouse Model.* Invest Ophthalmol Vis Sci, 2021. **62**(13): p. 26-26.

126. Prusky, G.T., et al., *Rapid quantification of adult and developing mouse spatial vision using a virtual optomotor system.* Invest Ophthalmol Vis Sci, 2004. **45**(12): p. 4611-6.

127. Seiler, M.J., et al., *Vision recovery and connectivity by fetal retinal sheet transplantation in an immunodeficient retinal degenerate rat model.* Invest Ophthalmol Vis Sci, 2017. **58**(1): p. 614-630.

128. Fujii, M., et al., *Evaluation of micro Electroretinograms Recorded with Multiple Electrode Array to Assess Focal Retinal Function.* Scientific reports, 2016. **6**: p. 30719-30719.

129. Ito, S. and D.A. Feldheim, *The Mouse Superior Colliculus: An Emerging Model for Studying Circuit Formation and Function.* Front Neural Circuits, 2018. **12**: p. 10.

130. Yamasaki, S., et al., *A Genetic modification that reduces ON-bipolar cells in hESC-derived retinas enhances functional integration after transplantation.* iScience, 2022. **25**(1): p. 103657.

131. He, X.Y., et al., *Synaptic repair and vision restoration in advanced degenerating eyes by transplantation of retinal progenitor cells.* Stem Cell Reports, 2021. **16**(7): p. 1805-1817.

132. Pearson, R.A., et al., *Donor and host photoreceptors engage in material transfer following transplantation of post-mitotic photoreceptor precursors.* Nat Commun, 2016. **7**: p. 13029.

133. Singh, M.S., et al., *Transplanted photoreceptor precursors transfer proteins to host photoreceptors by a mechanism of cytoplasmic fusion.* Nat Commun, 2016. **7**: p. 13537.

134. Nickerson, P.E.B., A. Ortin-Martinez, and V.A. Wallace, *Material Exchange in Photoreceptor Transplantation: Updating Our Understanding of Donor/Host Communication and the Future of Cell Engraftment Science.* Front Neural Circuits, 2018. **12**: p. 17.

135. Boudreau-Pinsonneault, C. and M. Cayouette, *Cell lineage tracing in the retina: Could material transfer distort conclusions?* Dev Dyn, 2018. **247**(1): p. 10-17.

136. Jiang, D., et al., *Bioenergetic Crosstalk between Mesenchymal Stem Cells and various Ocular Cells through the intercellular trafficking of Mitochondria.* Theranostics, 2020. **10**(16): p. 7260-7272.

137. Santos-Ferreira, T., et al., *Stem Cell-Derived Photoreceptor Transplants Differentially Integrate Into Mouse Models of Cone-Rod Dystrophy.* Invest Ophthalmol Vis Sci, 2016. **57**(7): p. 3509-20.

138. Heisterkamp, P., et al., *Evidence for endogenous exchange of cytoplasmic material between a subset of cone and rod photoreceptors within the adult mammalian retina via direct cell-cell connections.* Exp Eye Res, 2022: p. 109033.

139. Trapani, I., A. Puppo, and A. Auricchio, *Vector platforms for gene therapy of inherited retinopathies.* Progress in retinal and eye research, 2014. **43**: p. 108-128.

140. Dias, M.F., et al., *Molecular genetics and emerging therapies for retinitis pigmentosa: Basic research and clinical perspectives.* Progress in retinal and eye research, 2018. **63**: p. 107-131.

141. Seiler, M.J., R.B. Aramant, and S.L. Ball, *Photoreceptor function of retinal transplants implicated by light-dark shift of S-antigen and rod transducin.* Vision Res, 1999. **39**: p. 2589-2596.

142. Woch, G., et al., *Retinal transplants restore visually evoked responses in rats with photoreceptor degeneration.* Invest Ophthalmol Vis Sci, 2001. **42**(7): p. 1669-76.

143. Sagdullaev, B.T., et al., *Retinal transplantation-induced recovery of retinotectal visual function in a rodent model of retinitis pigmentosa.* Invest Ophthalmol Vis Sci, 2003. **44**(4): p. 1686-95.

144. Thomas, B.B., et al., *Superior colliculus responses to light - preserved by transplantation in a slow degeneration rat model.* Exp Eye Res, 2004. **79**(1): p. 29-39.

145. Yang, P.B., et al., *Trophic Factors GDNF and BDNF Improve Function of Retinal Sheet Transplants.* Exp Eye Res, 2010. **91**: p. 727-738.

146. Thomas, B.B., et al., *Retinal transplantation - A treatment strategy for retinal degenerative diseases*, in *Retinal Degenerative Diseases*, J.G. Hollyfield, R.E. Anderson, and M.M. LaVail, Editors. 2006, Springer: New York, NY. p. 367-376.

147. Aramant, R.B. and M.J. Seiler, *Progress in retinal sheet transplantation.* Prog Retin Eye Res, 2004. **23**(5): p. 475-94.

148. Seiler, M.J., R.B. Aramant, and H.S. Keirstead, *Retinal Transplants: Hope to Preserve and Restore Vision?* Optics and Photonics News, 2008. **19**(4): p. 37-47.

149. Seiler, M.J. and R.B. Aramant, *Cell replacement and visual restoration by retinal sheet transplants.* Prog Retin Eye Res, 2012. **31**(6): p. 661-87.

150. Tucker, B.A., et al., *Transplantation of adult mouse iPS cell-derived photoreceptor precursors restores retinal structure and function in degenerative mice.* PLoS ONE, 2011. **6**(4): p. e18992.

151. Pearson, R.A., et al., *Restoration of vision after transplantation of photoreceptors.* Nature, 2012. **485**(3): p. 99-103.

152. Singh, M.S., et al., *Reversal of end-stage retinal degeneration and restoration of visual function by photoreceptor transplantation.* Proc Natl Acad Sci U S A, 2013. **110**(3): p. 1101-6.

153. Lamba, D.A., J. Gust, and T.A. Reh, *Transplantation of human embryonic stem cell-derived photoreceptors restores some visual function in Crx-deficient mice.* Cell Stem Cell, 2009. **4**(1): p. 73-9.

154. Mansergh, F.C., et al., *Loss of photoreceptor potential from retinal progenitor cell cultures, despite improvements in survival.* Exp Eye Res, 2010. **91**: p. 500-512.

155. Thomson, J.A., et al., *Embryonic stem cell lines derived from human blastocysts.* science, 1998. **282**(5391): p. 1145-1147.

156. Takahashi, K., et al., *Induction of pluripotent stem cells from adult human fibroblasts by defined factors.* Cell, 2007. **131**(5): p. 861-72.

157. Fligor, C.M., et al., *Three-dimensional retinal organoids facilitate the investigation of retinal ganglion cell development, organization and neurite outgrowth from human pluripotent stem cells.* Scientific reports, 2018. **8**(1): p. 14520.

158. Wahlin, K., et al., *Photoreceptor outer segment-like structures in long-term 3D retinas from human pluripotent stem cells. Sci Rep 7: 766*. 2017.

159. McLelland, B.T., et al., *Transplanted hESC-derived retina organoid sheets differentiate, integrate, and improve visual function in retinal degenerate rats.* Investigative ophthalmology & visual science, 2018. **59**(6): p. 2586-2603.

160. Assawachananont, J., et al., *Transplantation of embryonic and induced pluripotent stem cell-derived 3D retinal sheets into retinal degenerative mice.* Stem Cell Reports, 2014. **2**(5): p. 662-74.

161. Shirai, H., et al., *Transplantation of human embryonic stem cell-derived retinal tissue in two primate models of retinal degeneration.* Proceedings of the National Academy of Sciences, 2016. **113**(1): p. E81-E90.

162. Ao, Z., et al., *One-Stop Microfluidic Assembly of Human Brain Organoids To Model Prenatal Cannabis Exposure.* Anal Chem, 2020. **92**(6): p. 4630-4638.

163. Berger, E., et al., *Millifluidic culture improves human midbrain organoid vitality and differentiation.* Lab Chip, 2018. **18**(20): p. 3172-3183.

164. Boutin, M.E., et al., *3D Engineering of Ocular Tissues for Disease Modeling and Drug Testing.* Adv Exp Med Biol, 2019. **1186**: p. 171-193.

165. Goto-Silva, L., et al., *Computational fluid dynamic analysis of physical forces playing a role in brain organoid cultures in two different multiplex platforms.* BMC Dev Biol, 2019. **19**(1): p. 3.

166. Phelan, M.A., P.I. Lelkes, and A. Swaroop, *Mini and customized low-cost bioreactors for optimized high-throughput generation of tissue organoids.* Stem Cell Investig, 2018. **5**: p. 33.

167. Artero Castro, A., et al., *Deciphering retinal diseases through the generation of three dimensional stem cell-derived organoids: Concise Review.* Stem Cells, 2019. **37**(12): p. 1496-1504.

168. Smith, D., et al. , *<Smith et al. - 2014 - A Researcher's Guide to Microbial Research.pdf>.* 2014.

169. Berger, E., et al., *Millifluidic culture improves human midbrain organoid vitality and differentiation.* Lab on a Chip, 2018. **18**(20): p. 3172-3183.

170. Sidar, B., et al., *Long-term flow through human intestinal organoids with the gut organoid flow chip (GOFlowChip).* Lab Chip, 2019. **19**(20): p. 3552-3562.

171. Beauchamp, M.J., G.P. Nordin, and A.T. Woolley, *Moving from millifluidic to truly microfluidic sub-100-mum cross-section 3D printed devices.* Anal Bioanal Chem, 2017. **409**(18): p. 4311-4319.

172. Qin, D., Y. Xia, and G.M. Whitesides, *Soft lithography for micro-and nanoscale patterning.* Nature protocols, 2010. **5**(3): p. 491-502.

173. Collin, J., et al., *CRX expression in pluripotent stem cell ‐ derived photoreceptors marks a transplantable subpopulation of early cones.* Stem Cells, 2019. **37**(5): p. 609-622.

174. Zhong, X., et al., *Generation of three-dimensional retinal tissue with functional photoreceptors from human iPSCs.* Nature communications, 2014. **5**: p. 4047.

175. Digman, M.A., et al., *The phasor approach to fluorescence lifetime imaging analysis.* Biophys J, 2008. **94**(2): p. L14-6.

176. Ranjit‡, S., et al., *Determination of the metabolic index using the fluorescence lifetime of free and bound NADH in the phasor approach.*

177. Stringari, C., et al., *Phasor fluorescence lifetime microscopy of free and protein-bound NADH reveals neural stem cell differentiation potential.* PLoS one, 2012. **7**(11): p. e48014.

178. Datta, R., et al., *Fluorescence lifetime imaging of endogenous biomarker of oxidative stress.* Sci Rep, 2015. **5**: p. 9848.

179. Hong, C.-C., J.-W. Choi, and C.H. Ahn, *A novel in-plane passive microfluidic mixer with modified Tesla structures.* Lab on a Chip, 2004. **4**(2): p. 109-113.

180. Sridhar, A., et al., *Single-cell transcriptomic comparison of human fetal retina, hPSC-derived retinal organoids, and long-term retinal cultures.* Cell reports, 2020. **30**(5): p. 1644-1659. e4.

181. Shekhar, K., et al., *Comprehensive classification of retinal bipolar neurons by single-cell transcriptomics.* Cell, 2016. **166**(5): p. 1308-1323. e30.

182. Niven, J.E. and S.B. Laughlin, *Energy limitation as a selective pressure on the evolution of sensory systems.* J Exp Biol, 2008. **211**(Pt 11): p. 1792-804.

183. Wolfe, R.P. and T. Ahsan, *Shear stress during early embryonic stem cell differentiation promotes hematopoietic and endothelial phenotypes.* Biotechnol Bioeng, 2013. **110**(4): p. 1231-42.

184. Regmi, S., A. Fu, and K.Q. Luo, *High Shear Stresses under Exercise Condition Destroy Circulating Tumor Cells in a Microfluidic System.* Scientific Reports, 2017. **7**(1): p. 39975.

185. Frangos, J.A., L.V. McIntire, and S.G. Eskin, *Shear stress induced stimulation of mammalian cell metabolism.* Biotechnol Bioeng, 1988. **32**(8): p. 1053-60.

186. Ovando-Roche, P., et al., *Use of bioreactors for culturing human retinal organoids improves photoreceptor yields.* Stem Cell Research & Therapy, 2018. **9**(1): p. 156.

187. Schwartz, A., *Chronic open-angle glaucoma secondary to rhegmatogenous retinal detachment.* Transactions of the American Ophthalmological Society, 1972. **70**: p. 178.

188. Smith, Y.C., Grande, K. K., Rasmussen, S. B., & O'Brien, A. D., *Novel Three-Dimensional Organoid Model for Evaluation of the Interaction of Uropathogenic Escherichia coli with Terminally Differentiated Human Urothelial Cells.* 2006.

189. Carterson, A.J., Höner zu Bentrup, K., Ott, C. M., Clarke, M. S., Pierson, D. L., Vanderburg, C. R., Buchanan, K. L., Nickerson, C. A., Schurr, M. J., *A549 Lung Epithelial Cells Grown as Three-Dimensional Aggregates: Alternative Tissue Culture Model for Pseudomonas aeruginosa Pathogenesis.* Infection and Immunity, 2005. **73**(2): p. 1129-1140.

190. Salerno-Goncalves, R., A. Fasano, and M.B. Sztein, *Development of a Multicellular Three-dimensional Organotypic Model of the Human Intestinal Mucosa Grown Under Microgravity.* J Vis Exp, 2016(113).

191. Hjelm, B.E., et al., *Development and characterization of a three-dimensional organotypic human vaginal epithelial cell model.* Biol Reprod, 2010. **82**(3): p. 617-27.

192. Homan, K.A., et al., *Flow-enhanced vascularization and maturation of kidney organoids in vitro.* Nat Methods, 2019. **16**(3): p. 255-262.

193. Ramachandran, S.D., et al., *In Vitro Generation of Functional Liver Organoid-Like Structures Using Adult Human Cells.* PLoS One, 2015. **10**(10): p. e0139345.

194. Kasendra, M., et al., *Development of a primary human Small Intestine-on-a-Chip using biopsy-derived organoids.* Sci Rep, 2018. **8**(1): p. 2871.

195. Zhang, Y.S., et al., *Multisensor-integrated organs-on-chips platform for automated and continual in situ monitoring of organoid behaviors.* Proc Natl Acad Sci U S A, 2017. **114**(12): p. E2293-E2302.

196. Mattei, G., Giusti, Serena, Ahluwalia, Arti, *Design Criteria for Generating Physiologically Relevant In Vitro Models in Bioreactors.* 2014. **2**(3): p. 548-569.

197. Macdonald, N.P., et al., *Comparing Microfluidic Performance of Three-Dimensional (3D) Printing Platforms.* Analytical Chemistry, 2017. **89**(7): p. 3858-3866.

198. Archberger, K.P., C.; Haderspeck, J.; Bolz, S.; Rogal, J.; Chuchuy, J.; Nikolova, M.; Cora, V.; Antowiak, L.; Haq, W.; Shen, N.; Schenke-Layland, K.; Ueffing, M.; Liebau, S.; Loskill, P. , *Merging organoid and organ-on-a-chip technology to generate complex multi-layer tissue models in a human retina-on-a-chip platform.* eLife 2019.

199. Stringari, C., et al., *Metabolic trajectory of cellular differentiation in small intestine by Phasor Fluorescence Lifetime Microscopy of NADH.* Scientific reports, 2012. **2**(1): p. 1-9.

200. Wright, B.K., et al., *NADH distribution in live progenitor stem cells by phasor-fluorescence lifetime image microscopy.* Biophysical journal, 2012. **103**(1): p. L7-L9.

201. Datta, R., et al., *Label-free imaging of metabolism and oxidative stress in human induced pluripotent stem cell-derived cardiomyocytes.* Biomedical optics express, 2016. **7**(5): p. 1690-1701.

202. Thapa, R., et al., *Prevalence, Pattern and Risk Factors of Retinal Diseases Among an Elderly Population in Nepal: The Bhaktapur Retina Study.* Clin Ophthalmol, 2020. **14**: p. 2109-2118.

203. Singh, R.K. and I.O. Nasonkin, *Limitations and Promise of Retinal Tissue From Human Pluripotent Stem Cells for Developing Therapies of Blindness.* Front Cell Neurosci, 2020. **14**: p. 179.

204. Fligor, C.M., et al., *Three-dimensional retinal organoids facilitate the investigation of retinal ganglion cell development, organization and neurite outgrowth from human pluripotent stem cells.* Sci Rep, 2018. **8**(1): p. 14520.

205. Maity, B., D. Sheff, and R.A. Fisher, *Immunostaining: detection of signaling protein location in tissues, cells and subcellular compartments.* Methods Cell Biol, 2013. **113**: p. 81-105.

206. Shannon, S.R., et al., *Chapter Fifteen - Identifying vitamin A signaling by visualizing gene and protein activity, and by quantification of vitamin A metabolites*, in *Methods in Enzymology*, E. Pohl, Editor. 2020, Academic Press. p. 367-418.

207. Sanderson, M.J., et al., *Fluorescence microscopy.* Cold Spring Harb Protoc, 2014. **2014**(10): p. pdb.top071795.

208. Palczewska, G., et al., *Noninvasive multiphoton fluorescence microscopy resolves retinol and retinal condensation products in mouse eyes.* Nat Med, 2010. **16**(12): p. 1444-9.

209. Bush, P.G., D.L. Wokosin, and A.C. Hall, *Two-versus one photon excitation laser scanning microscopy: critical importance of excitation wavelength.* Front Biosci, 2007. **12**: p. 2646-57.

210. Rubart, M., *Two-Photon Microscopy of Cells and Tissue.* Circulation Research, 2004. **95**(12): p. 1154-1166.

211. Bastiaens, P.I.H. and A. Squire, *Fluorescence lifetime imaging microscopy: spatial resolution of biochemical processes in the cell.* Trends in Cell Biology, 1999. **9**(2): p. 48-52.

212. Belluscio, L., *Two-Photon Imaging in Live Rodents.* Current Protocols in Neuroscience, 2005. **32**(1): p. Unit 2.9.

213. Wei, A., et al., *Two-Photon Microperimetry: A Media Opacity-Independent Retinal Function Assay.* Transl Vis Sci Technol, 2021. **10**(2): p. 11.

214. Datta, R., et al., *Fluorescence lifetime imaging microscopy: fundamentals and advances in instrumentation, analysis, and applications.* J Biomed Opt, 2020. **25**(7): p. 1-43.

215. Ranawat, H., S. Pal, and N. Mazumder, *Recent trends in two-photon auto-fluorescence lifetime imaging (2P-FLIM) and its biomedical applications.* Biomed Eng Lett, 2019. **9**(3): p. 293-310.

216. Becker, W., *Fluorescence lifetime imaging – techniques and applications.* Journal of Microscopy, 2012. **247**(2): p. 119-136.

217. Cao, R., H. Wallrabe, and A. Periasamy, *Multiphoton FLIM imaging of NAD(P)H and FAD with one excitation wavelength.* J Biomed Opt, 2020. **25**(1): p. 1-16.

218. Lakowicz, J.R., et al., *Fluorescence lifetime imaging of free and protein-bound NADH.* Proc Natl Acad Sci U S A, 1992. **89**(4): p. 1271-5.

219. Nakabayashi, T., K. Awasthi, and N. Ohta, *Application of Fluorescence Lifetime Imaging (FLIM) to Measure Intracellular Environments in a Single Cell.* Adv Exp Med Biol, 2017. **1035**: p. 121-133.

220. Dysli, C., et al., *Fluorescence lifetime imaging ophthalmoscopy.* Prog Retin Eye Res, 2017. **60**: p. 120-143.

221. Sauer, L., et al., *Review of clinical approaches in fluorescence lifetime imaging ophthalmoscopy.* J Biomed Opt, 2018. **23**(9): p. 1-20.

222. Ranjit, S., et al., *Determination of the metabolic index using the fluorescence lifetime of free and bound nicotinamide adenine dinucleotide using the phasor approach.* J Biophotonics, 2019. **12**(11): p. e201900156.

223. Govender, M., K. Chetty, and H. Bulcock, *A review of hyperspectral remote sensing and its application in vegetation and water resource studies.* Water SA, 2007. **33**(2): p. 145-151.

224. Gao, L. and R.T. Smith, *Optical hyperspectral imaging in microscopy and spectroscopy – a review of data acquisition.* Journal of Biophotonics, 2015. **8**(6): p. 441-456.

225. Hedde, P.N., et al., *Phasor-based hyperspectral snapshot microscopy allows fast imaging of live, three-dimensional tissues for biomedical applications.* Communications Biology, 2021. **4**(1): p. 721.

226. Ben Ami, T., et al., *Spatial and Spectral Characterization of Human Retinal Pigment Epithelium Fluorophore Families by Ex Vivo Hyperspectral Autofluorescence Imaging.* Transl Vis Sci Technol, 2016. **5**(3): p. 5-5.

227. Dwight, J.G., et al., *Hyperspectral Image Mapping Spectrometry for Retinal Oximetry Measurements in Four Diseased Eyes.* Int Ophthalmol Clin, 2016. **56**(4): p. 25-38.

228. Hadoux, X., et al., *Non-invasive in vivo hyperspectral imaging of the retina for potential biomarker use in Alzheimer's disease.* Nat Commun, 2019. **10**(1): p. 4227.

229. Choi, E.H., et al., *Retinoids in the visual cycle: role of the retinal G protein-coupled receptor.* Journal of Lipid Research, 2021. **62**: p. 100040.

230. Cutrale, F., A. Salih, and E. Gratton, *Spectral Phasor approach for fingerprinting of photo-activatable fluorescent proteins Dronpa, Kaede and KikGR.* Methods Appl Fluoresc, 2013. **1**(3): p. 35001.

231. Cutrale, F., et al., *Hyperspectral phasor analysis enables multiplexed 5D in vivo imaging.* Nature Methods, 2017. **14**(2): p. 149-152.

232. Stringari, C., et al., *Metabolic trajectory of cellular differentiation in small intestine by Phasor Fluorescence Lifetime Microscopy of NADH.* Sci Rep, 2012. **2**(1): p. 1-9.

233. Palczewska, G., et al., *Noninvasive two-photon microscopy imaging of mouse retina and retinal pigment epithelium through the pupil of the eye.* Nat Med, 2014. **20**(7): p. 785-9.

234. Palczewska, G., et al., *Endogenous fluorophores enable two-photon imaging of the primate eye.* Invest Ophthalmol Vis Sci, 2014. **55**(7): p. 4438-47.

235. Alexander, N.S., et al., *Image registration and averaging of low laser power two-photon fluorescence images of mouse retina.* Biomed Opt Express, 2016. **7**(7): p. 2671-91.

236. Palczewska, G., et al., *Noninvasive two-photon optical biopsy of retinal fluorophores.* Proc Natl Acad Sci U S A, 2020. **117**(36): p. 22532-22543.

237. Dutta, A., et al., *A proof of concept 'phase zero' study of neurodevelopment using brain organoid models with Vis/near-infrared spectroscopy and electrophysiology.* Scientific Reports, 2020. **10**(1): p. 20987.

238. Schwarz, C., et al., *Tacrolimus, Mycophenolate Mofetil, and Low-Dose Steroids With or Without Interleukin-2 Receptor Antibody Induction Therapy: A Retrospective Cohort Analysis.* Transplantation Proceedings, 2015. **47**(8): p. 2446-2449.

239. Thomson, A.W., C.A. Bonham, and A. Zeevi, *Mode of Action of Tacrolimus (FK506): Molecular and Cellular Mechanisms.* Therapeutic Drug Monitoring, 1995. **17**(6): p. 584-591.

240. Allison, A.C., *Mechanisms of action of mycophenolate mofetil.* Lupus, 2005. **14 Suppl 1**: p. s2-8.

241. Molday, R.S. and D. MacKenzie, *Monoclonal antibodies to rhodopsin: characterization, cross-reactivity, and application as structural probes.* Biochemistry, 1983. **22**(3): p. 653-60.